

Silesian University of Technology
Faculty of Mechanical Engineering
Institute of Fundamentals of Machinery Design

DOCTORAL DISSERTATION

*Non-destructive evaluation of composite aircraft elements
based on ultrasonic testing and image analysis*

Angelika Wronkowicz

Dissertation advisor:

Assoc. Prof. Anna Timofiejczuk, Ph.D., D.Sc. Eng.
Silesian University of Technology, Gliwice

Auxiliary advisor:

Lt. Col. Krzysztof Dragan, Ph.D., D.Sc. Eng.
Air Force Institute of Technology, Warsaw

Gliwice, 2018

Contents

Acknowledgements	v
List of important abbreviations	vi
1 Introduction	1
2 Research background	5
2.1 Composite materials and their application in the aircraft industry	5
2.1.1 Fibre Reinforced Polymer (FRP) composites	5
2.1.2 Manufacturing of aircraft structural elements	6
2.1.3 Polymer composites in the aircraft industry	8
2.2 Types of flaws and damage in FRP composites	9
2.2.1 Manufacturing flaws and fracture	10
2.2.2 In-service fracture and damage	14
2.2.3 Mechanisms of damage propagation	18
2.3 Maintenance of aircraft elements according to design methodologies	19
2.3.1 Safe-life design	19
2.3.2 Fail-safe design	20
2.3.3 Damage tolerance methodology	21
2.3.4 Condition-based maintenance	22
2.3.5 Structural health monitoring	22
2.3.6 Repairs of composite aircraft elements	23
2.4 NDT&E methods of aircraft composite elements	24
2.4.1 Visual and penetrant inspection	25
2.4.2 Tap-testing	25
2.4.3 Eddy current inspection	26
2.4.4 Shearography	26
2.4.5 Thermography	27
2.4.6 Acoustic emission testing	27
2.4.7 Radiographic and tomographic inspection	28
2.4.8 Ultrasonic inspection	29

2.5	Application of image analysis methods in ultrasonic inspections	33
3	Research problem	37
3.1	Identification of the research problem	37
3.2	Research objectives	38
3.3	Research hypothesis	38
3.4	Research scope and plan	38
4	Related works	40
4.1	Measurement uncertainty factors in damage detection and evaluation . . .	40
4.1.1	Material parameters	40
4.1.2	Operating parameters	43
4.1.3	Calibration	47
4.1.4	Post-processing of ultrasonic scans	49
4.1.5	Summary	50
4.2	Damage detection using image analysis methods	52
4.2.1	A review of related work	52
4.2.2	A review of image segmentation methods	54
4.2.3	Summary	61
4.3	3D damage reconstruction and visualisation using image processing	62
4.3.1	A review of related work	62
4.3.2	Summary	63
5	Analysis of measurement uncertainty in damage detection and evaluation	64
5.1	Structures and experiments	64
5.1.1	Specimens preparation	64
5.1.2	UT measurements by the Pulse-Echo method	66
5.1.3	UT measurements by the Phased Array method	67
5.2	Image analysis algorithm	68
5.3	Results and discussion	69
5.3.1	Results from the Pulse-Echo UT	69
5.3.2	Results from the Phased Array UT	74
5.4	Conclusions	76

6	Analysis of damage detection accuracy using image segmentation methods	78
6.1	Structures and experiments	78
6.2	Comparative analysis of image segmentation algorithms	79
6.2.1	Analysis of bi-modal threshold-based segmentation methods	80
6.2.2	Analysis of edge-based segmentation methods	82
6.2.3	Analysis of clustering-based segmentation methods	82
6.2.4	Analysis of region-based segmentation methods	87
6.2.5	Analysis of other histogram-based segmentation approaches	88
6.3	Conclusions	92
7	Analysis of 3D damage reconstruction and visualisation	93
7.1	Structures and experiments	93
7.1.1	Specimen preparation	93
7.1.2	Ultrasonic testing	94
7.1.3	X-ray CT testing	95
7.2	3D damage reconstruction based on ultrasonic C-Scan	96
7.3	3D damage reconstruction based on ultrasonic B-Scans	97
7.4	Verification of 3D damage reconstruction based on CT method	100
7.5	Conclusions	101
8	Examples of the application of the developed image analysis algorithms	103
8.1	Impact damage detection and evaluation in CFRP specimens	103
8.1.1	Structures and experiments	103
8.1.2	Image analysis algorithm	105
8.1.3	Results and discussion	107
8.1.4	Conclusions	108
8.2	Delamination size monitoring in CFRP aircraft elements	109
8.2.1	Structures and experiments	109
8.2.2	Image analysis algorithm	109
8.2.3	Results and discussion	112
8.2.4	Conclusions	113
8.3	3D damage reconstruction and visualisation in CFRP aircraft elements	114
8.3.1	Structures and experiments	114
8.3.2	Image analysis algorithm	114
8.3.3	Results and discussion	116
8.3.4	Conclusions	116

9 Summary conclusions	118
9.1 Conclusions	118
9.2 Further work	121
Bibliography	122
List of figures	137
Summary	141
Streszczenie	142

Acknowledgements

I would like to express my sincere gratitude and appreciation to my advisors for their guidance, motivation and help during the realisation of the doctoral dissertation. I address special thanks to Prof. Anna Timofiejczuk for inviting and encouraging me to start a scientific career and to Prof. Krzysztof Dragan for giving the opportunity to deal with such fascinating problems and for sharing his practical experience and immense expert knowledge.

I sincerely thank Prof. Wojciech Cholewa for his valuable comments, continuous motivation and encouragement.

I am very grateful to experts from the Air Force Institute of Technology in Warsaw for their contribution in the realisation of the experiments and providing the access to laboratories and research facilities. In particular, I thank Adam Latoszek, Marcin Ciepliński and Dr. Michał Dziendzikowski for their kind assistance and substantial support during the realisation of ultrasonic testing, and Marek Chalimoniuk for performing X-ray computed tomography testing.

My sincere thanks also go to other researchers for the discussions and support in preparation of composite specimens used in the research, especially: Dr. Claudio Sbaruffatti from the Politecnico di Milano (Italy) for providing experimental data of an impacted specimen; Prof. Andrzej Katunin from the Silesian University of Technology for the assistance in introducing impact damage to other set of specimens; and Dr. Krzysztof Lis from the Silesian University of Technology for introducing artificial damage in specimens by milling and measuring them with the use of a coordinate measuring machine. I also address special thanks to Dr. Georgi Mihaylov from the Royal Mail Group in London (UK) for our common discussions that resulted in new ideas connected with the research on image analysis steps.

Special thanks go to my family and friends for their patience and support in striving towards my goal.

Angelika Wronkowicz
Gliwice, April 2018

List of important abbreviations

AFIT	Air Force Institute of Technology
BVID	Barely Visible Impact Damage
CBM	Condition-Based Maintenance
CFRP	Carbon Fibre Reinforced Polymer
CM	Condition Monitoring
CT	Computed Tomography
DAC	Distance Amplitude Correction
DGS	Distance Gain Size
EM	Expectation Maximization
FBH	Flat-Bottom Hole
FML	Fibre Metal Laminate
FRP	Fibre Reinforced Polymer
GFRP	Glass Fibre Reinforced Polymer
GMM	Gaussian Mixture Model
LoG	Laplacian of Gaussian
MBP	Minima-Between-Peaks
NDE	Non-Destructive Evaluation
NDI	Non-Destructive Inspection
NDT	Non-Destructive Testing
NDT&E	Non-Destructive Testing and Evaluation
pfRF	Peak Filtered Radio Frequency
PMC	Polymer Matrix Composite
RF	Radio Frequency
ROI	Region of Interest
SHM	Structural Health Monitoring
SNR	Signal to Noise Ratio
SRM	Statistical Region Merging
tfRF	Threshold Filtered Radio Frequency
ToF	Time-of-Flight
UT	Ultrasonic Testing

1. Introduction

Polymeric composite materials, owing to their numerous advantages, are nowadays widely applied for manufacturing of structural components of aircrafts. However, due to their complex nature and anisotropy, they are vulnerable to the formation of various types of defects during their production and damage during operation. One of the most significant problems is the type of damage caused by an impact, especially that of a low velocity, since it may cause extensive internal cracks and delaminations with simultaneous little, if any, visible evidence of the damage at the surface. Damage occurring in composite materials is a complex phenomenon and, under load, may propagate and interact with manufacturing defects up to failure. Because of that, composites are inspected with the use of non-destructive testing and evaluation (NDT&E) methods to detect the damage appearance and monitor its progression. The maintenance procedures of aircraft elements are accomplished according to one of developed to-date design methodologies. Historically, the development of these methodologies was motivated by several tragic accidents in the aircraft industry and the necessity of increasing safety and prolongation of airworthiness. One of the currently used approaches is based on so-called damage tolerance methodology, in which the existence of small cracks and defects in the aircraft structure is permissible if they can resist failure before the scheduled inspection. Therefore, one of the most important tasks in this methodology is to perform periodic non-destructive inspections (NDIs) of the critical aircraft elements.

Among many NDT&E methods, ultrasonic testing (UT) is one of the most commonly applied owing to its capabilities of detecting various types of flaws and damage inside composite elements and evaluating their location and geometrical properties. Principally, the obtained output during such an inspection is in a form of ultrasonic data presenting levels of attenuation of the ultrasonic waves by particular areas of a tested structure. A change in that levels may indicate the presence of a flaw or damage, but also noise or, for instance, an embedded element inside the structure, such as a stiffening rib or a rivet. There is a number of factors influencing on the damage detectability and the occurrence of measurement errors during performing ultrasonic inspections. To these factors one can include test material parameters and selection of operating parameters, such as the scanning method and applied transducer's characteristics. For that reason, qualifications

of the UT operators should meet many requirements, i.e. they should pass appropriate training and own certificates allowing for performing such inspections as well as much experience and knowledge on the internal architecture of the examined element.

Another factor affecting the measurement uncertainty includes post-processing methods applied to the obtained ultrasonic data. After the inspection, the obtained ultrasonic data is thoroughly analysed and a report with the description on the detected damage sites with annotations about their sizes and locations is prepared. In practice, this is performed with the use of software dedicated to UT that usually provides only very simple tools for manual processing of the data. In the case of inspecting the structural aircraft elements such as vertical stabilizers that are very large the evaluation based on ultrasonic data is time-consuming and, due to the need for manual parameter settings, human error is more likely to occur. There are several standardised methods employed for damage evaluation, i.e. quantification by the post-processing of the ultrasonic data, however, there is a need of the application of the second method for verification. Certain approaches can be found in the literature that are aimed at the development of image analysis algorithms for aiding the analysis of ultrasonic scans, including the steps of damage detection, evaluation as well as enhanced three-dimensional (3D) visualisation. However, these approaches were developed for specific problems and are not universal. No studies could be found that would cover a comprehensive analysis of accuracy of damage detection using various image processing methods as well as the assessment of the measurement uncertainty.

Ultrasonic and many other types of inspections of aircraft elements have been performed in the Air Force Institute of Technology (AFIT) in Warsaw for years and the presented problems resulted from the actual needs observable in practice. This thesis is the result of close cooperation with the AFIT, where all the experimental parts of the research connected with the ultrasonic inspections were accomplished. The main motivation towards undertaking the presented research was to investigate how to increase the efficiency of ultrasonic inspections of composite aircraft elements, i.e. shorten duration of the ultrasonic data analysis and ensure repeatability of the damage evaluation results. The assumptions were established for the algorithms to be developed to be highly accurate, fast, and universal for any type and internal construction of a tested element as well as any damage type and shape. The research was divided into four main stages: analysis of the factors affecting the damage detectability and the measurement error; analysis of damage detection accuracy using various image segmentation methods; analysis of 3D damage reconstruction and visualisation methods; and the application of the developed image analysis algorithms to several case studies. All the experiments were performed with the use of elements made of carbon fibre reinforced polymer (CFRP) composites. All the

image processing and analysis algorithms were implemented in Matlab[®] by MathWorks (Natick, MA).

The structure of the thesis is as follows. Chapter 2 introduces the background of the research problem and the undertaken study. This starts with a brief description of composite materials, particularly the composites made of a polymeric matrix reinforced with fibres, their manufacturing and the application in the aircraft industry. Afterwards, the manufacturing flaws and in-service damage types that may appear in such structures are listed and shortly described. The problem of damage propagation in composite structures with explanation of its mechanisms and thus the necessity of increasing the operational safety are introduced. Subsequently, several design methodologies are presented in the order they were historically developed, which are directly related to the way the aircraft elements are maintained. Moreover, basic methods of repairing composite elements, which takes place after the detection of damage of an unacceptable size, are shortly introduced. As most of the currently implemented maintenance methodologies in the aircraft industry require performing NDIs of the critical elements, the most relevant NDT&E methods employed for this purpose are briefly described. For ultrasonic inspections, a more detailed overview is introduced and exemplary inspection results in the aircraft industry are presented based on the example of research carried out by the AFIT. Finally, the introduction to standardised methods of processing of ultrasonic data, aimed at damage detection and quantification, and the application of other image analysis methods for this purpose are presented. The needs in this area are presented, which resulted in the motivation towards performing the research presented in this thesis.

Chapter 3 presents the identified research problem based on the performed review and learned findings as well as the needs discussed in chapter 2 and the defined research objectives, hypothesis and scope of the thesis.

Chapter 4 presents the theory and work related to the aspects raised in the next chapters, divided into three main sections. The first section introduces a review on the measurement uncertainty factors in damage detection and evaluation with reference to appropriate standards including material parameters, operating parameters during UT, calibration methods and post-processing of the ultrasonic data. The second section presents a review on methods of damage detection using image analysis that have already been developed and an overview of image segmentation methods that possibly could be applied for this purpose. The third section introduces related work connected with the application of image processing methods for the aim of 3D damage reconstruction and visualisation. The chapter's sections end with summaries and comments on their relation to own work.

Chapter 5 includes the description of the experimental studies aimed at the inves-

tigation on the measurement uncertainty during testing CFRP structures with variable UT techniques and their parameters. The results on the damage detectability and the obtained measurement error are discussed and the most suitable testing parameters for the used in the research structures are selected.

Chapter 6 covers a comprehensive analysis on the damage detection accuracy when processed the ultrasonic scans with algorithms based on various image segmentation methods, including the proposed approaches. Among the image segmentation groups of methods the threshold-, edge-, region-, and clustering-based ones were tested. The results of the comparative analysis carried out on the basis of ultrasonic images of a low and high degree of complexity are discussed and the most accurate and universal image analysis methods are selected.

Chapter 7 presents the results of the development of algorithms aimed at 3D damage reconstruction and visualisation by processing of ultrasonic scans. These cover the reconstruction of impact damage in a CFRP specimen based on two types of ultrasonic data, namely B-Scans and C-Scans, and the verification of this reconstruction based on reference data obtained with the use of X-ray computed tomography.

Chapter 8 introduces the exemplary results of the application of the developed algorithms based on three case studies. The first case includes the analysis of impact damage detection and evaluation in CFRP structures. In this study, the specimens with a wide range of impact damage cases were tested, which were obtained with combinations of variable impact energy and shapes of impactors. The second case is devoted to the analysis of delamination size monitoring in CFRP aircraft elements. This includes the steps of damage detection and quantification based on ultrasonic scans obtained during two separate inspections of aircraft elements and the assessment of damage propagation. The third case is dedicated to the application of the proposed 3D damage reconstruction and visualisation approach to ultrasonic scans of aircraft elements.

Chapter 9 covers the summary conclusions on the research, including the comments to the obtained results and the description of further work that has already started to be realised within frames of a research project financed by the National Science Centre (Poland).

2. Research background

2.1 Composite materials and their application in the aircraft industry

The first airplanes were constructed mainly from wood and later from metal alloys (Federal Aviation Administration, 2012b; Konieczny, 2013). In the mid-20th century, significant advancement in aircraft construction technology occurred with the application of composite materials. Composites have become competitive alternatives to traditional metallic (aluminium, steel and titanium) materials due to their numerous advantages. A combination of two or more different materials, based on the definition of composites, enables the creation of a superior and unique material. The most commonly adapted composites in the aircraft industry, among the Polymer Matrix Composites (PMCs), are based on Fibre Reinforced Polymers (FRPs). They have found a wide application in military, general aviation as well as in commercial aircraft. They have also been used in the production of helicopter rotor blades, sailplanes and gliders. This is due to the significant weight savings, greater strength and stiffness, aerodynamic smoothness, and resistance to corrosion and fatigue that FRPs ensure over traditional metallic structures. Moreover, a possibility of the shape forming is much more advanced than in the metal processing technologies. Lightness is of key importance in the aircraft industry since reducing structural weight of an aircraft results in reduced fuel consumption and increased payload capacity (Taylor, 2008).

2.1.1 Fibre Reinforced Polymer (FRP) composites

An FRP is a composite made of a polymeric matrix reinforced with fibres. Plies of the matrix are layered together to form a composite laminate. Generally, fibres are responsible for transferring loads, whereas a binder material is responsible for holding the fibres in a desired location and orientation, and for filling voids between them (Taylor, 2008). Structural properties of a composite laminate, such as stiffness and strength, depend on the stacking sequence of the plies, i.e. the distribution of ply orientations through the composite thickness. Proper selection of ply orientation is necessary to provide a structurally efficient design. Orientations of the plies at 0° , $\pm 45^\circ$, and 90° ensure reaction to axial,

shear, and side loads, respectively. Because a composite material is strong and stiff only in the direction of the fibres, successive plies of the matrix are layered together at various angles to achieve the required strength characteristics. This enables the transfer of loads in different directions and the use of such a composite as a structural material. There are two basic arrangements of fibre reinforcement: unidirectional and bidirectional, where the former provides the strength and stiffness only in one direction and the latter ensures strength in two directions (not necessarily of the same strength) typically oriented at 90° to each other (Federal Aviation Administration, 2012a). An example of unidirectional ply orientation is a pre-impregnated (prepreg) tape (Fig. 2.1 on the left side), which is an FRP reinforcement that is pre-impregnated with a thermoplastic resin. An example of bidirectional ply orientation is a plain weave fabric (Fig. 2.1 on the right side), which offers more flexibility for a lay-up of complex shapes when compared to straight unidirectional tapes. Prepregs are the standard in the aerospace industry (Federal Aviation Administration, 2012a). It should be noted that there are also other architectures of fibre reinforcement which can be multidirectional or even three-dimensional (Mallick, 2007).

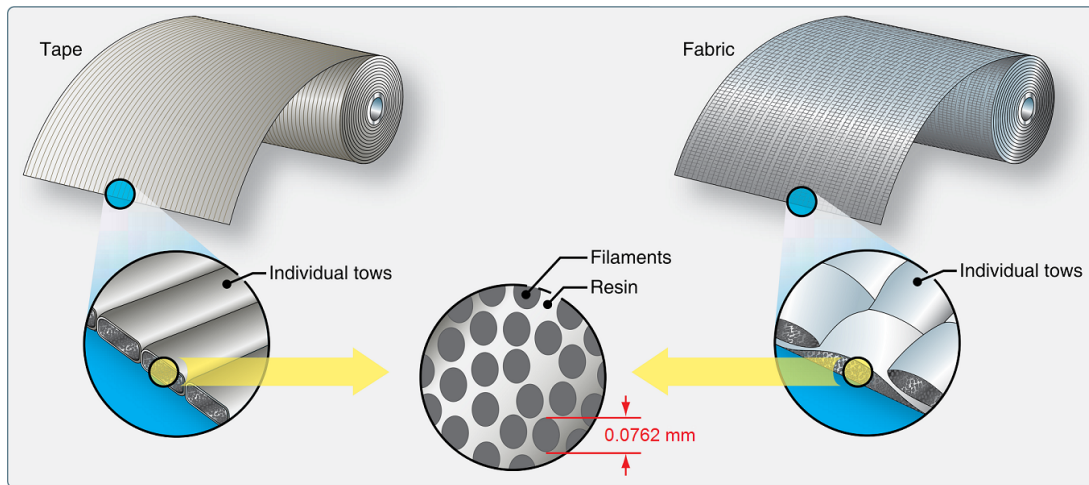


Fig. 2.1: A scheme of basic prepreg products (Federal Aviation Administration, 2012a)

Many aerospace composite structures are made of quasi-isotropic materials, which simulate the properties of an isotropic material, ensuring the same properties in all directions. The plies of the quasi-isotropic lay-up are stacked in the following sequence: 0° , 90° , $+45^\circ$, and -45° (Fig. 2.2), or 0° , -60° , and $+60^\circ$ (Federal Aviation Administration, 2012a).

2.1.2 Manufacturing of aircraft structural elements

There are numerous methods of manufacturing of composite structures such as hand laminating (or wet lay-up), autoclave processing, filament winding, pultrusion, resin transfer

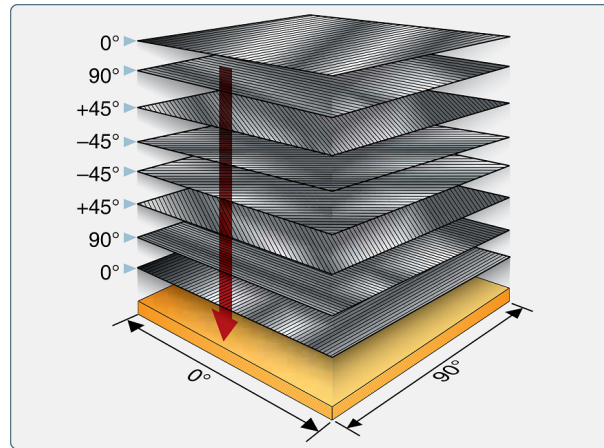


Fig. 2.2: An example of quasi-isotropic material lay-up $(0/90/\pm 45)_s$ (Federal Aviation Administration, 2012a)

moulding, etc. (Mallick, 2007; Hoa, 2009; Masuelli, 2013; Divya *et al.*, 2016). In the case of manufacturing of high quality polymer composite aerospace/aircraft structural components, autoclaves (heated pressure vessels) have become irreplaceable tools. Autoclaves are now being used to produce very large aircraft components such as wings and fuselages. Autoclaves can process a wide variety of materials with varying contours and complex shapes (Upadhyaya *et al.*, 2011). Manufacturing with use of autoclaves is a very common process in the aerospace industry because it affords precise control over the moulding process due to a long and slow curing cycle. This precise control creates the exact laminate geometric forms needed to ensure strength and safety in the aerospace industry (Masuelli, 2013). The typical vacuum bagging scheme adopted in the autoclave moulding technique for a composite component is shown in Fig. 2.3.

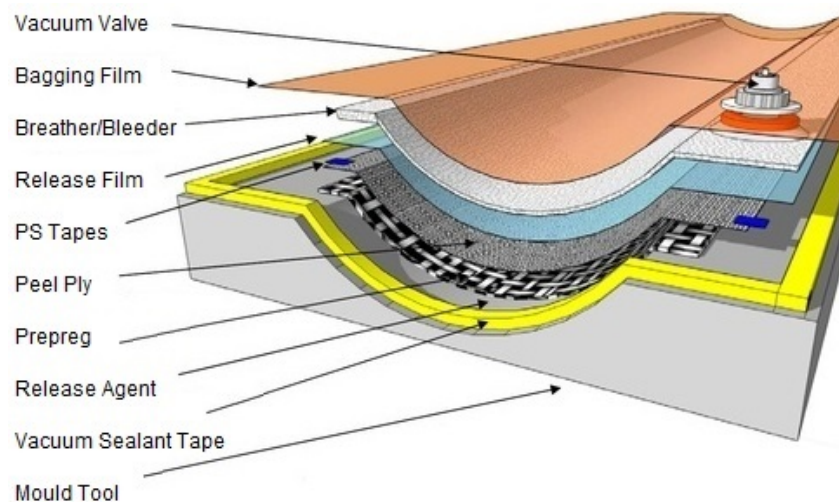


Fig. 2.3: Typical autoclave moulding bagging scheme (Aero Consultants AG, n.a.)

The consecutive steps of the manufacturing process are as follow. Individual sheets of a prepreg material (previously stored in a fridge) are laid-up and placed in an open mould. It has to be mentioned that detailed QA/QC (quality assurance and quality control) of the date of validity of the material for the use has to be verified. Moreover, those materials have to be certified in accordance with relevant standards used in the aerospace industry. Before this ply, a release agent can be inserted as an option, which enables more resin to remain on the laminate surface. Then, the laminate is covered with a peel ply, a release film, a breather/bleeder material and a vacuum bagging film (Masuelli, 2013). The peel ply provides an easy release barrier between the laminate surface and the breather and bleeder. The breather and bleeder traps and holds the excess resin from the laminate. The release films and the breather/bleeder can be held in place by use of pressure sensitive tapes (Aero Consultants AG, n.a.). The bagging film is an air-tight seal placed over the sealant tape and it applies vacuum pressure over the entire laminate. A vacuum is pulled on the component and the entire mould is placed into an autoclave. A vacuum valve connects the bagging film to a vacuum tubing. The component is cured with an elevated temperature and a continuous vacuum to extract entrapped gasses from the laminate (Masuelli, 2013) and to create chemically irreversible bonds between the resin and the fibre plies (Kjelgaard, 2012).

2.1.3 Polymer composites in the aircraft industry

In aviation, a composite aircraft usually contains one or a combination of the following components (Taylor, 2008):

- carbon fibre/epoxy resin (CFRP) – used as a primary structural and skin material,
- aramid (Kevlar[®]) fibre/epoxy resin – mostly used in military applications, in primary structures and armour plating,
- glass fibre – used as a structural and skin material (on general aviation aircraft),
- glass fibre/phenolic resin (GFRP – Glass Fibre Reinforced Polymer) – used in interior fittings, furnishings and structures,
- boron fibre/epoxy resin – used in composite repair patches, or on older composite structures,
- honeycomb (e.g. DuPont[™] Nomex[®]) core/face sheets made of aluminium, carbon fibre, glass fibre, or Kevlar[®] – used in floor boards, interior walls, storage bins, wing spoilers, fairings, ailerons, flaps, engine nacelles, and rudders (Federal Aviation Administration, 2012a; DuPont, n.a.).

Initially, composites were used for a variety of secondary aviation components, such as rudders and wing trailing edge panels, which require directional reinforcement. Later, composite materials were introduced into the manufacturing of main load-carrying structures, such as in the Airbus A380, of which they cover 25% by weight. The central wing box of the aircraft is entirely made of CFRP (Meola and Carlomagno, 2013). Use of composites in the construction of aircraft is still increasing; an example is the Boeing 787 Dreamliner which contains approximately 50% composites by weight (Hale, 2006; Meola and Carlomagno, 2013) including major structural elements such as the fuselages, wings, spars and stringers (Fig. 2.4). As depicted, CFRPs are the one of the most widely used composites for structural aircraft applications, such as floor beams, horizontal and vertical stabilizers, flight control surfaces, primary fuselages and wing structures, as well as engine nacelles and fan casings, and interior components (Kjelgaard, 2012; Konieczny, 2013). In the case of the carbon sandwich composites, their skin materials are usually made of CFRP laminates whereas the core materials of honeycomb panels. Composites are also finding applications in other aviation components, such as turbofan engine blades and cowlings, fairings, landing gear doors, leading and trailing edge panels on the wing and stabilizer, floor boards, and propellers (Taylor, 2008; Federal Aviation Administration, 2012a).

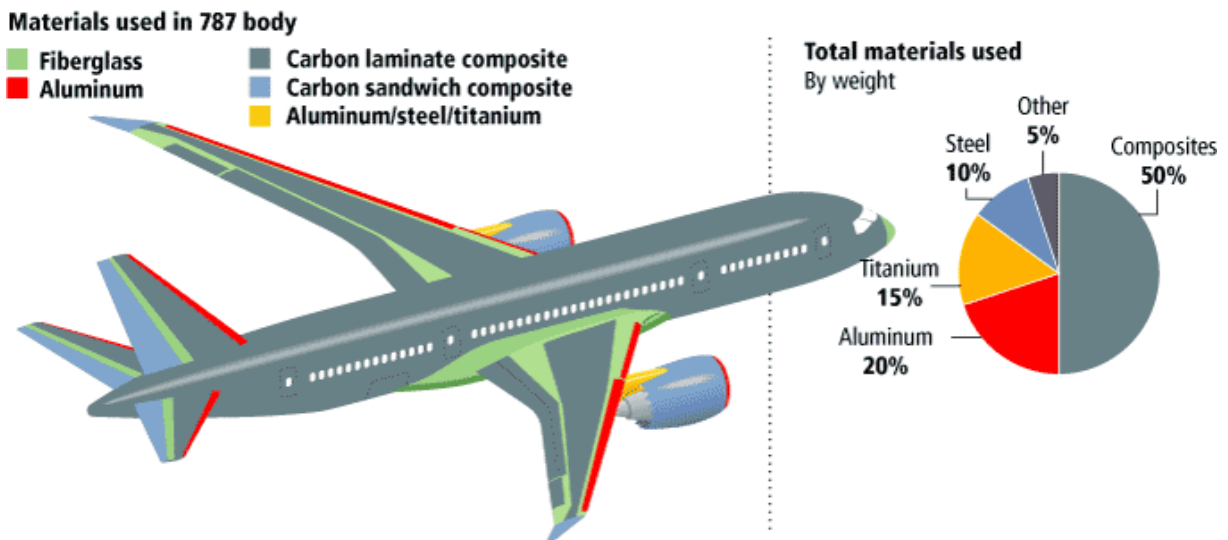


Fig. 2.4: Materials used in the Boeing 787 Dreamliner body (*Boeing 787 Specs*, n.a.)

2.2 Types of flaws and damage in FRP composites

As mentioned, composite structures have numerous advantages which make them the best solution for structural aircraft components. However, due to their complex nature,

the presence of interfaces, inherent anisotropy and non-homogeneity, they have drawbacks which include poorer performance at high temperatures, poor through-the-thickness properties and poor resistance to transverse impact loadings (Donadon *et al.*, 2008). They are subject to many factors that may cause flaws or damage, both during the manufacturing process and throughout the service life of a composite component.

Several definitions should be introduced here in order to differentiate notions that will be further used. A **flaw** is an imperfection, defect, or blemish. Examples of flaws in composites are porosity and foreign body inclusion. A **fracture** can be understood as breakage of a material, or breakage of atomic bonds. Examples of fractures in composites are fibre breakage, cracks in the matrix, fibre/matrix debonds, and delamination. **Damage** refers to a collection of distributed, irreversible changes brought to a material from a set of energy dissipating physical or chemical processes, resulting in thermomechanical loadings. Examples of damage are multiple matrix cracking, multiple intralaminar cracking in a laminate, or local delamination distributed in an interlaminar plane. **Fatigue** is the progressive structural damage or weakening of a material caused by repeatedly applied loads. **Failure** is the inability of a given element, made of a composite material, to perform its design function. Fracture is one example of a possible failure; however, a material could fracture locally and still perform its design function. Similarly, a composite material, upon damage (e.g. in a form of multiple cracking), may still continue to carry loads and therefore, its load-bearing requirement is met, but it could fail in respect to other design requirements (e.g. vibration characteristics or deflection limits). In practice, a failure event in a composite structure is preceded by the progressive occurrence and interaction of various damage mechanisms (Talreja and Singh, 2012).

2.2.1 Manufacturing flaws and fracture

Flaws and fracture that occur during manufacturing of composites appear due to the difficulty of the production processes of FRP composites compared to traditional metallic structures, and the fact that most composite structures are laid up by hand. Automated production using autoclaves is still a relatively new method and as a result, quality problems occur (Taylor, 2008). Among common flaw or fracture types of FRP composites formed during production, one can distinguish (Federal Aviation Administration, 2012a; Smith, 2009; Karbhari, 2013):

- air entrapment: porosity, blisters and voids;
- foreign object inclusion;
- water moisture;

- interface fracture: delamination, debonding;
- incorrect fibre volume distribution: resin starved areas, resin rich areas;
- reinforcement flaws and fracture: fibre misalignment, fibre waviness (wrinkling), ply misalignment, fibre breakage;
- matrix flaws and fracture: matrix cracking, micro-cracking, incompletely cured matrix.

Moreover, most composite elements require further processing such as drilling and cutting. During these operations other types of flaws, fractures, or damage may occur which can be caused by improper drilling, improper machining, improper sanding, mishandling, or tool drops, e.g.: flawed fastener holes, inadvertent edge cuts, surface scratches and other imperfections, impact damage (Federal Aviation Administration, 2012a).

Porosity. The most common flaw that occurs during the manufacturing process is porosity (Fig. 2.5(a)) – the presence of a large number of distributed micro-voids (air bubbles) in a resin matrix of FRP composites (Smith, 2009; Hsu, 2013; Rajic, 2013). Such a microscopic single void is too small to be of structural significance or to be detected individually by common inspection techniques, but they collectively may reduce mechanical properties of a component to an unacceptable degree (Birt and Smith, 2004). Porosity can be caused by inadequate evacuation of the volatile gas released during the cure cycle, which is usually the result of incorrect, or non-optimal, curing parameters such as duration, temperature, pressure, or vacuum bleeding of a resin (Hsu, 2013; Smith, 2009). This leads to the entrapment of microscopic or even macroscopic air bubbles.

Porosity in composite laminates has been a persistent quality issue in aircraft/aerospace components. For instance, one of ten test fuselage barrels produced by Boeing as a part of the Federal Aviation Administration (FAA) certification process for the 787 Dreamliner was deemed unacceptable due to excessive porosity between plies of carbon fibre. Defects between plies cause poor bonding between them, which can lead to delamination or stringer disbonding (Mulcair and Villiers, 2006).

Blisters and voids. As previously mentioned, macroscopic voids (Fig. 2.5(a)) may occur in FRP composites due to improper curing processing. Other existing flaws inside a composite, such as foreign object inclusion, may also lead to void formation (Fig. 2.5(b)). Moreover, stitching of fibre tows (bunches of fibres) to hold them in place and prevent misalignment during the cure process can itself introduce numerous regularly-spaced sites for void or blister formation (Smith, 2009).

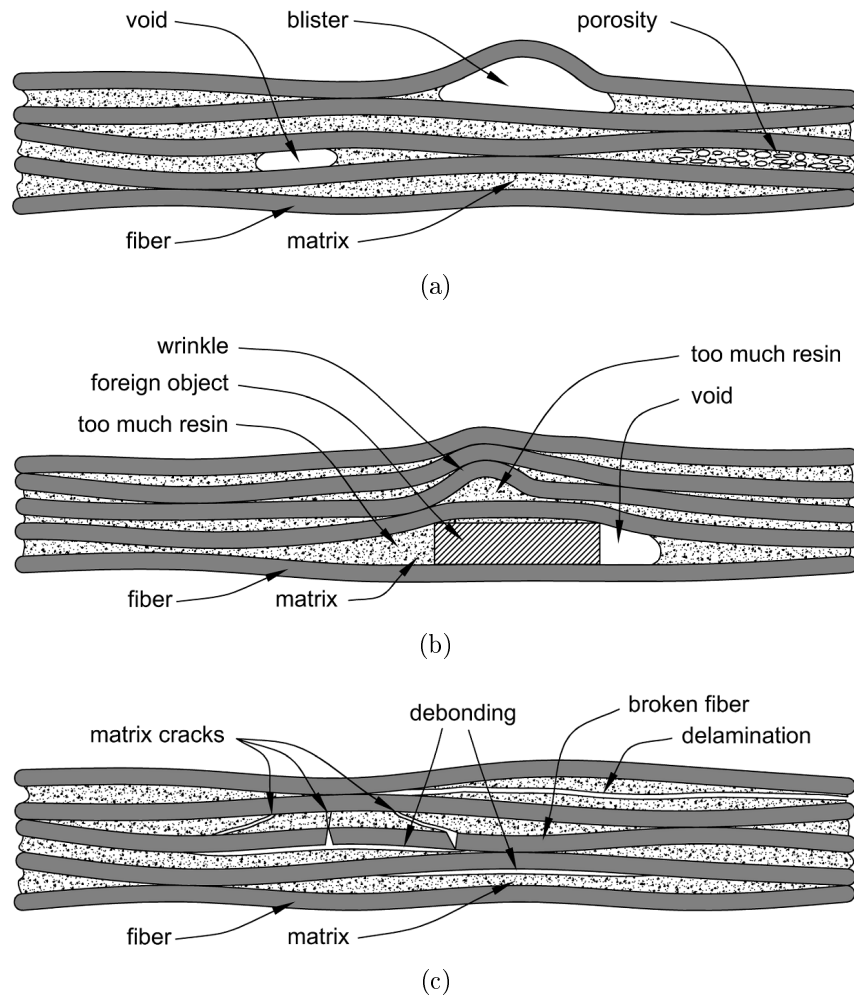


Fig. 2.5: Typical manufacturing flaws and fractures in FRP composites (Unnpórrsson, 2008)

Foreign object inclusion. Another example of a manufacturing flaw includes a contaminated surface (e.g. with greasy marks from fingers) or the inclusion of foreign bodies (Fig. 2.5(b)), such as prepreg backing paper or separation film, accidentally left between plies during lay-up (Federal Aviation Administration, 2012a; Smith, 2009).

Water moisture. Composite materials are susceptible to ingress of moisture, which is another dangerous factor since it may contribute to failure. Water can penetrate into a composite material through subsequent plies of a laminate. Temperature outside an aircraft during flight is very low (it can reach even -90°C) which causes freezing of water during flight and its thawing after landing. This freezing/thawing cycle may result in subsurface damage and lead to delamination (Mulcair and Villiers, 2006; Taylor, 2008).

Delamination. Delamination is a planar defect that usually occurs on the interface between plies in a composite laminate (Fig. 2.5(c)). Delamination formation during the manufacturing process may be caused by insufficient wetting of fibres, contaminated fibres, machining and mechanical loading (such as low-energy impact loading), lack of reinforcement in the thickness direction, and matrix cracks that grow into the interlaminar layer (Ghasemnejad *et al.*, 2012; Smith, 2009; Federal Aviation Administration, 2012a).

Debonding. Debonding occurs when two materials stop adhering to each other (Fig. 2.5(c)) and can initiate delamination in adjacent laminate layers (Federal Aviation Administration, 2012a). Debonding may be the result of factors such as incorrect cure conditions for the adhesive or contamination of the bonded surfaces (Smith, 2009).

Incorrect fibre volume distribution. Fibre volume distribution can be incorrect due to excess or insufficient resin. A component is considered **resin-rich** if too much resin is used (Fig. 2.5(b)), or **resin-starved** if not enough resin is applied during the wet layup process or if too much resin is bled off during the curing process. The weight ratio of fibre to resin of 60:40 is considered to be optimal (Federal Aviation Administration, 2012a; Smith, 2009). Too little resin results in inadequate bonding between plies and the formation of voids. In turn, too much resin lowers the volume fraction of fibres and increases the risk of cracks (Gaylord, 1974).

Fibre misalignment and waviness. Fibre misalignment can occur when fibres are laid up, mostly in low-cost manufacturing techniques which usually involve the infusion of resin into pre-formed dry fibres in moulds. Fibre misalignment, or waviness – i.e. wrinkling (Fig. 2.5(b)), can occur both in-plane of the material and out-of-plane. Such defects reduce mechanical properties like stiffness and strength and are potentially disastrous, but are rarely encountered due to high standards of quality control (Smith, 2009). Wrinkles can cause air entrapment and resin accumulation.

Ply misalignment. Ply misalignment can be caused by mistakes made in the lay-up of laminate plies. This results in modification of the overall stiffness and strength of the composite and may cause bending during the curing process (Smith, 2009).

Fibre Breakage. Fibre breakage (Fig. 2.5(c)) occurs less commonly during manufacturing of FRP composites, however, it can be critical since such structures are designed to be fibre dominant, i.e. most of the loads are carried by fibres (Federal Aviation Administration, 2012a).

Matrix cracking and micro-cracking. Matrix imperfections usually appear on the interface between the matrix and fibres or in the matrix parallel to the fibres. Accumulation of matrix cracks (Fig. 2.5(c)) or micro-cracks can cause degradation of matrix-dominated properties. In the case of fibre dominant laminates, only slight reduction of material properties occurs if matrix degradation is not widespread. However, matrix imperfections may develop into delaminations (Federal Aviation Administration, 2012a).

Incompletely cured matrix. The matrix can also be incompletely cured, which may be caused by an incorrect curing cycle or faulty material (Smith, 2009).

2.2.2 In-service fracture and damage

In general, in-service fracture or damage of composite structures may result from impacts, static overloads, fatigue, overheating, hydrothermal effects, lightning strikes or creep (Smith, 2009). Common in-service damage types of components made of FRP composites include (Smith, 2009; Federal Aviation Administration, 2012a; Giurgiutiu, 2016):

- matrix damage: matrix cracking, micro-cracking;
- interface damage: debonding, delamination/interlaminar cracking, fibre bridging and fibre pull-out;
- reinforcement damage: fibre breakage;
- environmental degradation and ingress of moisture;
- impact damage (mixed damage).

External damage that occurs on the matrix surface during operation should also be mentioned. These include: surface cracks, scratches, abrasions, external voids or notches. They can be easily detected and usually their appearance is insignificant (Katunin, 2015a).

Matrix cracking and micro-cracking. Since FRP composites offer high strength and stiffness properties in the longitudinal direction, matrix cracking usually occurs parallel to the fibres due to tension, compression and shearing (Talreja and Singh, 2012; Safri *et al.*, 2014). Such matrix cracks (including micro-cracks, intralaminar (ply) cracks, and transverse cracks) are found to be caused by tensile loading, fatigue loading, impacts or by thermal cycling. They can originate from fibre/matrix debonds or manufacturing defects such as voids and inclusions (see Fig. 2.6). The formation of debonds, in turn, can be initiated by micro-cracks which grow under compressive loading (Gamstedt and Sjögren, 1999). As the debonds at the interface between the fibres and matrix coalesce and grow, a transverse crack forms (Harrison and Bader, 1983) (see Fig. 2.7). Although matrix

cracking does not cause structural failure by itself, it can result in a significant decrease in material stiffness and can also induce other forms of damage, such as delamination and fibre breakage, and give pathways for entry of fluids (Talreja and Singh, 2012).

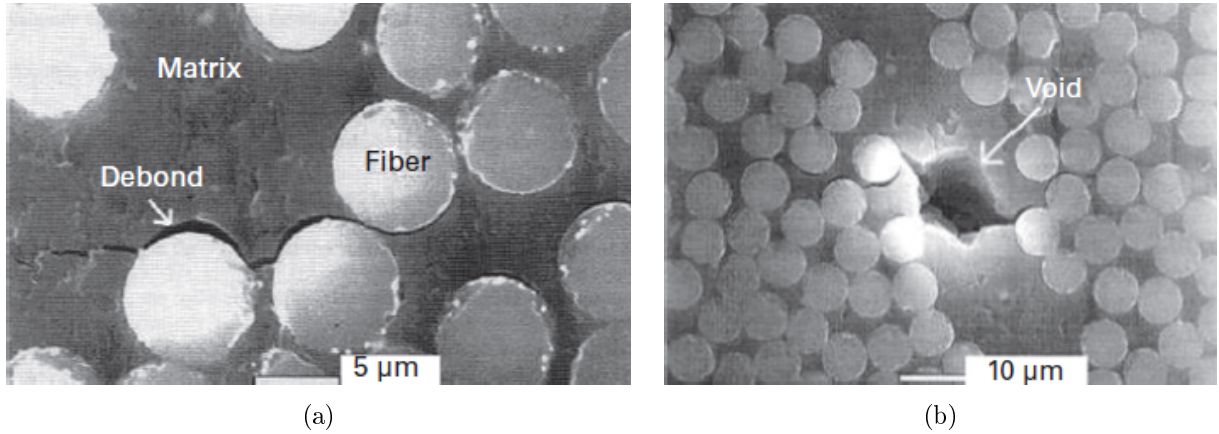


Fig. 2.6: Matrix crack initiated from: fibre debonds (a), void (b) (Wood and Bradley, 1997)

Debonding. The fibre/matrix interface plays a significant role in stress transfer between the fibre and the matrix. Too weak or too strong fibre/matrix bonding may lead to matrix cracking or fibre cracking. As mentioned earlier, the debonding can be induced by a matrix crack, or it can result from a growth of interfacial defects (Talreja and Singh, 2012). Debonding may also occur due to unexpected out-of-plane stresses (Giurgiutiu, 2016). The constraint between the fibre and the matrix also affects other damage mechanisms such as fibre bridging, and fibre pull-out (Talreja and Singh, 2012; Katunin, 2015a).

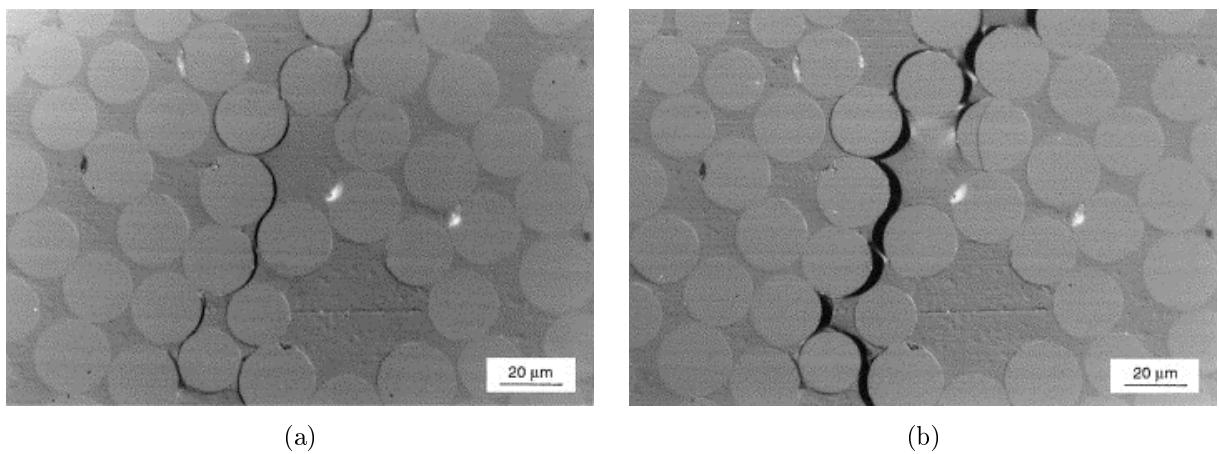


Fig. 2.7: Fibre/matrix debonds (a) and coalescence into transverse cracks (b) (Gamstedt and Sjögren, 1999)

Delamination/interlaminar cracking. Because of low interlaminar strength of fibre composites, they are susceptible to delamination during their lifetime (Meola and Carlomagno, 2013). Delamination (or interlaminar cracking), i.e. cracking in the interfacial plane between two adjoining plies in a layered composite, causes separation of the plies. The three basic fracture modes for delamination are: opening mode, sliding mode, and tearing mode. In composite laminates, delamination often occurs at cut (free) edges, such as at holes, or at an exposed surface through the thickness (Talreja and Singh, 2012). Major sources of delamination are tension loads, shear loads applied between plies in the laminate, low-velocity impacts, or local interlaminar cracking induced by ply cracks (Talreja and Singh, 2012; Safri *et al.*, 2014; Taylor, 2008). Delamination can significantly reduce the compression strength of laminated structures. Under certain conditions, delamination or debonds can propagate upon repeated loading and cause catastrophic failure when the composite is loaded in compression (Federal Aviation Administration, 2012a; Taylor, 2008; Talreja and Singh, 2012).

Fibre bridging and fibre pull-out. Fibre bridging occurs when the stress distribution around a matrix crack is enough for propagation of the crack but is not enough for fibre breakage. When the matrix crack advances, the bridging fibres are pulled-out of the matrix (Fig. 2.8) (Katunin, 2015a).

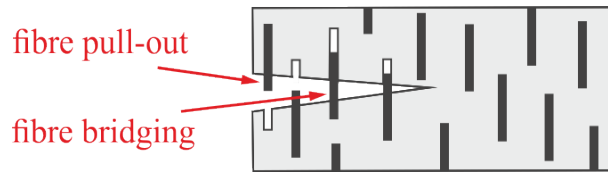


Fig. 2.8: A scheme of fibre bridging and fibre pull-out

Fibre breakage. The failure (separation) of FRP composites ultimately comes from breakage of fibres (Talreja and Singh, 2012). Fibre breakage causes overall structure failure since, as mentioned before, the reinforcement carries most of the loads (Katunin, 2015a).

Environmental degradation and ingress of moisture. Damage initiated during in-service can be caused by several environmental and operational factors. The mechanical properties of epoxy matrices degrade when exposed to long-term ultraviolet radiation, thermal cycling, high temperatures and moisture. Due to the different coefficients of thermal expansion between the fibres and the matrix, thermal changes cause the two materials to expand differently and create stresses at the fibre/matrix interface. These thermal stresses can lead to matrix cracking and debonding. The ingress of moisture degrades

matrix-dominated properties such as stiffness, shear strength, compressive strength, or impact tolerance (Unnþórsson, 2008; Smith, 2009). Moreover, lightning burns appear in an area of a composite subjected to high temperature during a lightning discharge, which results in degradation and decomposition of the polymeric matrix (Giurgiutiu, 2016).

Impact damage. FRP composites have the major drawback of being fragile and particularly sensitive to loads in the thickness direction, such as impacts, both during manufacturing and in-service. In the case of the aircraft elements, impact damage may be caused by hail, bird strikes in flight, runway debris impacts (during take-off and landing), or dropped tools during maintenance (Unnþórsson, 2008; Taylor, 2008; Hsu, 2013; Giurgiutiu, 2016). Impact damage is often classified as being of low-, medium-, or high-energy (or -velocity), depending on the impact parameters, or as BVID (Barely Visible Impact Damage), minor VID (minor Visible Impact Damage), and large VID, depending on the damage visibility during visual inspections (Bouvet and Rivallant, 2016). The resulting damage mechanisms due to impact loading can be divided into four distinct damage categories: delamination, matrix cracking, fibre breakage and total perforation (Donadon *et al.*, 2008). The structural response of composites differs between variable velocity impacts. Under low-energy impact a structure may experience only an elastic phase without perforation, since composites are able to absorb impact energy owing to the polymeric matrix that distributes energy through the structure (Meola and Carlomagno, 2013). For high velocity, e.g. in the case of ballistic impacts, the impact event is so short that the structure does not respond in flexural or shear modes, and a complete penetration occurs. The primary need for NDT of aircraft structures is the detection of damage produced by low-velocity impacts, which have the potential to create BVID that may cause significant internal structural damage with little, if any, visible evidence of damage at the surface (Rajic, 2013). The delaminations and interlaminar matrix cracks caused by a low-velocity impact tend to be distributed through the composite in a pattern that resembles the branches of a pine tree (Fig. 2.9). Adjacent to the impact site the damage is limited to a relatively small region, but it extends in size with increasing depth and typically reaches its maximum size near the back-wall of the composite (Rajic, 2013).

Such BVID may grow during in-service and, if undetected, lead to catastrophic failure (Meola and Carlomagno, 2013). In a report (Taylor, 2008) it is noted that in order to ensure BVID does not cause delamination resulting in structural failure, composite aircraft components are often designed with a safety factor of 3, or more. Safety factors such as these have been employed in the design of major composite structures in the Boeing 787 Dreamliner, such as the fuselage.

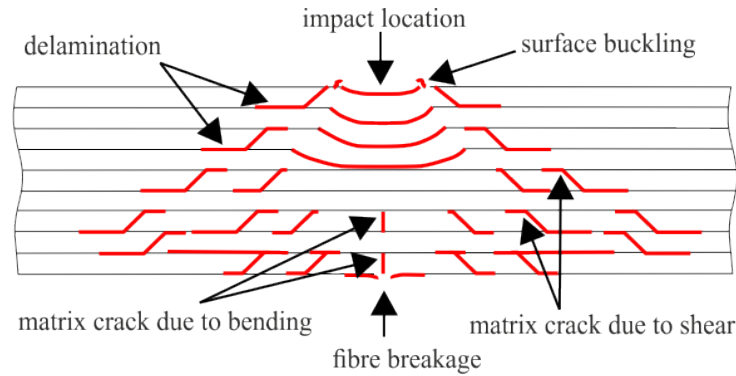


Fig. 2.9: A typical impact damage mode in an FRP composite structure (adapted from (Shyr and Pan, 2003))

2.2.3 Mechanisms of damage propagation

It should be pointed out that damage occurring in layered composites is a complex phenomenon and propagates progressively up to the failure. The failure of a PMC is generally preceded by an accumulation of different internal micro- and macro-structural damage types. Normally, the damage is well distributed throughout the composite and progresses with an increasingly applied load. It coalesces to form a macroscopic fracture shortly before the catastrophic failure. The sequence and interaction of the failure mechanisms depend on a type of the loading and properties of the constituents (Gdoutos, 2005). The three fundamental modes in which a composite may fail are tension, compression, and shear (Giurgiutiu, 2016).

Based on the studies (Talreja and Singh, 2012; Giurgiutiu, 2016), aimed at investigation of damage progression in a cross-ply laminated composite under fatigue loading, the stages under cyclic tension may look as follow. In the early stage of damage propagation, multiple matrix micro-cracking develops mainly in the layers with fibres aligned not parallel to the loading direction. As the cyclic loading continues, transverse matrix cracks develop from locations of defects such as voids, or areas of high fibre volume fraction or resin rich areas. Upon increasing loading, more and more cracks are formed. They grow and start interacting as they become closer, so that they become the macroscopic cracks. Stress concentrations cause initiation of so-called secondary cracks in locations of plies adjacent to the ones with the primary cracks, and as a result – initiation of interfacial debonding and thus local interlaminar cracks. Merging of the interlaminar cracks into strip-like zones leads to large scale delaminations. This causes the loss of the integrity of the composite in the delaminated regions and further damage development resulting in an extensive fibre breakage. Finally, the fracture failure of the overall composite laminate occurs through the locally failed regions. In (Talreja and Singh, 2012) it was reported that

similar damage progression scenario occurs under quasi-static loading. As mentioned, different orientation of plies in a laminate, varying thickness, or internal defects may modify the damage evolution (Taylor, 2008; Huang, 2013).

In view of this progressive damage behaviour, composite structures should be periodically inspected non-destructively to monitor the damage progression, which will be discussed in the next sections. Several notions related to the NDIs that will be further used should be introduced here. The term non-destructive testing (NDT) applies to an inspection of a structure without affecting it, whereas the term non-destructive evaluation (NDE) refers to such testing extended by a quantitative analysis of the detected damage, e.g. measurement of its size, shape, and orientation. They both are sometimes called together the NDT&E.

2.3 Maintenance of aircraft elements according to design methodologies

Striving to fulfilling requirements for aircraft structures, such as shortening the duration of inspections and ground handling, prolongation of airworthiness, increasing safety, leads to a necessity of taking operation of an aircraft into account at the stage of its design (Nowosielska and Kowalczyk, 2008). Therefore, the maintenance procedures in the aircraft industry are dependent upon the design methodology. Historically, the development of the design methodologies was often initiated by tragic accidents (Schijve, 2009; Wanhill, 2003). Several case histories are often cited as milestones in the aircraft industry's approaches to structural integrity, which will be recalled below.

2.3.1 Safe-life design

The most primary design methodology is a safe-life approach, which relies on predicting the durability of aircraft elements. It is based on the assumption that a component should not fail within a pre-determined number of cycles, i.e. during its operational "safe life" (Reddick, 1983). Inspection is not necessary because the components are simply replaced prior to their design life end. The basic criteria for determining the life cycles rely on fatigue tests of the components or the entire aircraft structures. Due to high costs and time-consuming of such tests, they are performed on single aircrafts' copies. This results in applying significant safety factors to ensure that no catastrophic failures will occur during operation with the safe-life regime (Kurnyta *et al.*, 2016). This methodology results in decommission of the component at the end of the safe life regardless of its actual condition.

In 1954, two aircrafts of de Havilland Comet fleet were crashed due to fuselage disintegration. These Comet accidents, and other experiences, showed that cracks sometimes occur much earlier than predicted, and the pure safe-life concept is insufficient (Wanhill, 2003).

2.3.2 Fail-safe design

The above-mentioned problem was addressed by the introduction of a fail-safe design in 1956. In the fail-safe, similarly to the safe-life approach, a structure is designed to achieve a satisfactory life time with no considerable damage. However, the difference between these two methodologies is that the fail-safe design assumes that the component will fail, and therefore it is designed to fail in a safe manner. The fail-safe design requires that if one component fails, the entire system does not fail. In other words, the components are arranged so that cracks will not lead to failure of the structure before they are detected and repaired. Damage has to be detected by inspection procedures before its development reduces the residual strength of the structure below an acceptable limit (Reddick, 1983; Wanhill, 2003). Verification of the fail-safe design concepts requires much fatigue and residual strength testing. When the fail-safe principles were first implemented, it was not required to do full-scale testing, however, subsequent experience and knowledge has led to mandatory full-scale testing (Wanhill, 2003).

It should be noted that not all structural components are amenable to the fail-safe design. The main exceptions are landing gears, usually made from high-strength steels and still designed to the safe-life principles (Wanhill, 2003).

In 1969, F-111 aircraft lost the left wing during a low-level training flight. The aircraft had accumulated only 107 airframe flight hours. This catastrophe was caused by a manufacturing flaw in the lower plate of the wing pivot fitting, which remained undetected. The loss of F-111 was one of the main reasons for the United States Air Force (USAF) to reconsider and abandon its previous policy, which was essentially the safe-life approach verified by full-scale fatigue testing. After much research, the USAF provided new guidelines to the Aircraft Structural Integrity Program (ASIP), incorporated in Military Specification MIL-A-83444 in 1974, known as the "Damage Tolerance philosophy" (Wanhill, 2003), and broadly described in a first handbook (Wood and Engle, 1979) to support the damage tolerance requirements.

Moreover, in 1977, the fail-safe concept failed when Dan Air Boeing 707-321C aircraft lost the entire horizontal stabilizer. The investigation revealed fatigue failure in the upper chord of the rear spar of the horizontal stabilizer. This crash prompted airwor-

thiness authorities to reconsider the fatigue problems of older aircrafts. It became clear that existing inspection methods and schedules were inadequate, and that supplementary inspection programs were needed to prevent older aircraft from becoming fatigue-critical (Wanhill, 2003).

2.3.3 Damage tolerance methodology

Damage tolerant design is similar to the fail-safe approach with the main difference that the latter assumes that cracks or damage might initiate during the aircraft operation, whereas the damage tolerant approach assumes the presence of a small flaw in the structure. A structure is designed to resist failure due to the assumed existence of flaws, cracks, or other damage for a time period sufficient to enable their detection. The damage-tolerant requirements address three key aspects: the residual strength, the damage propagation, and the damage detection involving NDIs of the structure under consideration (Reddick, 1983). It is very important to implement appropriate maintenance program based on regular NDIs that allow detecting damage before it propagates to the level causing reducing the strength of the structure below an acceptable limit. The inspection intervals are therefore computed such that no crack can grow to the critical size before the next inspection (Cot *et al.*, 2013).

The introduction of the damage tolerance principle has significantly reduced the risk of air crashes due to fatigue damage. Compared to the safe-life approach, the operation of aircraft according to the assumptions of damage tolerance also corresponded to the need for a more complete use of the construction elements and avoiding withdrawal of still valuable structures. Nevertheless, despite significant advances in the field of fracture mechanics and the development of numerical modelling methods for complex physical processes, it is impossible to predict all factors that could increase the risk of an accident. The risk of human error associated with NDIs is also difficult to be eliminated (Kurnyta *et al.*, 2016).

Another milestone in the aircraft industry's requirements to the structural integrity was the accident during Aloha Airlines flight 243. In 1988, Boeing 737-200 experienced an explosive decompression during climbing out at cruise altitude. The aircraft lost a part of the fuselage skin structure due to multiple fatigue cracks in spar splices. The Aloha Airlines Boeing 737 accident prompted again worldwide activities to ensure the safety and structural integrity of ageing aircrafts. Manufacturers, operators, and airworthiness authorities have collaborated to develop new regulations and advisory circulars, or extend the existing ones (Wanhill, 2003).

2.3.4 Condition-based maintenance

The scheduled-based maintenance methodologies, such as the damage tolerance approach, have evolved towards more cost-effective condition-based maintenance (CBM) (Cot *et al.*, 2013). The CBM can be described as a set of maintenance procedures derived mainly from the real-time assessment of a monitored object's condition, obtained with the use of embedded sensors and/or external measurements and tests using portable equipment. The main goal of the CBM is to perform maintenance only upon evidence of need. The CBM is closely associated to Condition Monitoring (CM), the base approach in which the results of measurements (e.g. of vibrations, acoustic emission or thermal radiation) are used to trigger the maintenance activities. A major challenge in the CBM methodology lies in the analysis of the obtained data to retrieve the diagnostic information from it. Usually, data-driven methods are developed for that purpose, e.g. based on trending, comparing with a baseline measurement, or sometimes based on physical models (Tinga and Loendersloot, 2014).

2.3.5 Structural health monitoring

Due to the increased reliability requirements, research has focused on developing continuous monitoring techniques by introducing permanently used sensors, which evolved into a structural health monitoring (SHM) discipline (Tinga and Loendersloot, 2014). The SHM involves integrating sensors and actuators (Dragan *et al.*, 2015), possibly smart materials, data transmission and computational power within the structure. Whereas NDT&E approaches focus on off-line monitoring, the SHM systems utilise NDT&E methods as tools and provide real-time monitoring of a structure during its operation using combinations of active and passive systems (Stępiński *et al.*, 2013; Karbhari, 2013). These systems have proved to be capable of detecting small (centimetre square) delaminations, millimetre-sized holes and impact damage of a few Joules (Fowler *et al.*, 2001). The SHM approaches can be classified into local systems, which monitor a small region of the structure surrounding the sensor, and global systems, which induce global motion of the structure. The examples of most commonly phenomena employed for the local SHM are the ultrasonic waves, eddy currents, thermal field, and acoustic emission. The most common methods used for the design of the SHM systems are guided waves, those based on fibre Bragg gratings (FBG) sensors (strain, temperature measurements and ultrasound sensing), vibrothermography and electromechanical impedance. The global SHM includes vibration-based methods, usually employing a sensor network (Stępiński *et al.*, 2013). These methods can be classified into signal-based and model-based approaches. The signal-

based methods use relations between the measured responses of the structure after ambient excitation and possible damage. The model-based methods monitor the structure by detecting shifts of its natural frequencies, increases in damping, or changes of vibration modes' shapes (Stępiński *et al.*, 2013; Boller and Staszewski, 2004; Kessler *et al.*, 2002).

The five levels of the SHM can be presented as particular steps that allow answering the following questions (Farrar and Worden, 2007):

1. **damage detection** (*Is there damage in the system?*),
2. **damage localisation** (*Where is the damage in the system?*),
3. **damage characterisation** (*What kind of damage is present?*),
4. **damage quantification** (*How severe is the damage?*),
5. **prognostics** (*How much useful life remains?*).

Currently, the first three levels can be achieved by many methods, whereas the last two are still quite challenging (Tinga and Loendersloot, 2014).

However, the SHM systems must be implemented during manufacturing of composites, thus can be applied only in newly-produced aircraft elements and they constitute a separate research area. Since the dissertation addresses the problems in the area of data analysis for passive NDT&E inspections, mostly being a part of the damage tolerance and the CBM methodologies, the SHM systems will not be discussed in more detail. The NDT&E inspection methods widely applied in the aircraft industry are described in section 2.4. It should be mentioned that NDT&E methods enable realisation of from the 1st up to the 4th SHM level, which simultaneously correspond to the stages of technical diagnostics of machines (Cempel *et al.*, 1992; Cholewa and Moczulski, 1995; Żółtowski, 1996), processes (Korbicz *et al.*, 2002), and systems (Natke and Cempel, 1997).

2.3.6 Repairs of composite aircraft elements

After detection of damage of an unacceptable size in a composite aircraft element, the decision must be made whether the structural element should be repaired or replaced. The extent of repair needed to restore the composite component to its former strength and stiffness is then considered. Because the strength design requirements are a function of the applied load direction, it is critical during the repair to replace each damaged ply with a ply of the same orientation and sequence (Federal Aviation Administration, 2012a). In-service repairs can be either permanent, which requires no further steps, or temporary, which will be monitored on a regular basis until the permanent repair is required. The types of repairs to composite structures can be classified as follow (Taylor, 2008):

- **non-patch repairs** – suitable for minor damage where NDT indicated no serious delamination or disbonding. For minor sub-surface flaws and delaminations, such repairs involve filling the affected area by a thermosetting resin. For minor surface damage, filler/potting repairs can be applied by filling the affected area with a fibre flock, smoothing back, and then curing;
- **bonded external patch repairs** – the most common repair type, suitable for repairing laminates and composite skin of a thickness below 2 mm. Bonded external patches usually consist of a tapered single lap-joint bonded over the affected area;
- **bonded scarf repairs** – suitable where a repair to thick sections of a composite is required. The bonded scarf repairs are advantageous for repairing large damaged areas as the damage is cut away and replaced with the scarf patch.

2.4 NDT&E methods of aircraft composite elements

An aircraft inspection can range from preflight and postflight inspections, which are a casual "walk-around" with a visual check for general condition and delivered mainly by the flight crew, to detailed inspections involving complete disassembly and the use of complex inspection aids and delivered by the qualified engineering staff. The time intervals for the inspection periods vary with the models of aircraft involved and the types of operations being conducted. In some instances, aircrafts are inspected when a specified number of flight hours is accumulated. During each inspection, appropriate check-lists must be used to ensure that no items are forgotten or overlooked. Moreover, so-called special inspections can be performed out of schedule in the case of occurrence of something out of the ordinary care and use of the aircraft, such as hard or overweight landing, severe turbulence, over "g" overload, lightning strike, fire damage, or flood damage (Federal Aviation Administration, 2008).

A variety of NDT&E methods have been developed that allow for a qualitative and some of them also quantitative analysis of the integrity of composite structures. The principal difference between qualitative and quantitative methods is that the first group is suitable only for damage detection, whereas the latter enables flaws to be also quantified in their location and/or size. The most common methods used for the inspections of the PMC aircraft components are shortly introduced in the following subsections. Since ultrasonic inspections have been by far the most popular in the NDT&E of composites (Hsu, 2013; Meola and Carlomagno, 2013), and is the subject of the research covered by this dissertation, this method is presented in more detail.

2.4.1 Visual and penetrant inspection

Visual inspection is the oldest and most common inspection form used for aircrafts, relying on the bare eye. However, it has to be mentioned that in accordance with the EN 4179/NAS 410 NDI personnel certification scheme this method is not regarded as the NDI but rather as maintenance inspection delivered by a qualified maintenance crew. It is usually one of the first methods used for locating potential defect areas. Once located, the areas of interest are more thoroughly examined (Mix, 2005). Approximately 80% of all NDI procedures are accomplished by the direct visual methods (Finch *et al.*, n.a.). Various tools can be used to aid this inspection procedure, such as flash-lights, inspection mirrors, magnifying instruments, borescopes, or video scanners (Finch *et al.*, n.a.; Ehrhart *et al.*, 2013). Moreover, a dye-penetrant can be applied to detect material discontinuities that may not be evident to the ordinary visual inspection. The basic purpose of the penetrant inspection is to increase the visible contrast between the defect and the underlying material. A high penetrating dye is sprayed on the composite element and it enters the surface opening of the discontinuity. Excess penetrant is removed, and a developer material (usually a dry white powder) is then applied that draws the liquid from the suspected flaw to reveal the discontinuity. The visual evidence of the suspected defect can then be seen either by the colour contrast in normal visible white light or by fluorescence under black ultraviolet light. The major limitation of the penetrant inspection is that it can detect only those discontinuities that are open to the surface (Finch *et al.*, n.a.). The typical applications of visual inspections include the detection of scratches, resin starvation, resin richness, wrinkles, ply bridging, cracks, impact damage, foreign inclusions, blisters, etc. (Federal Aviation Administration, 2012a; Ehrhart *et al.*, 2013). The visual inspection is economical and easily performed, however, it is limited by the inspector's sight (Ehrhart *et al.*, 2013), and the internal flaws such as delaminations and disbonds cannot be detected (Federal Aviation Administration, 2012a).

2.4.2 Tap-testing

Tap test is a widely used resonance test for a quick evaluation of aircraft surfaces to detect the presence of delamination or debonding, as well as voids (Finch *et al.*, n.a.; Ehrhart *et al.*, 2013). The inspected surface is tapped with a tool producing a constant frequency and the acoustic response of the structure is analysed. Several inexpensive tools have been designed for tap tests, from coins to hammers, as well as Woodpeckers – automated hammers that offer selectable tapping intensity and frequencies (Ehrhart *et al.*, 2013). The acoustic response is compared with that of a known good area. Tap

testing is limited to finding relatively shallow defects in skins less than ca. 2 mm in thickness. This method is generally qualitative (Ehrhart *et al.*, 2013) and its accuracy depends on the inspector's subjective interpretation of the test response (Finch *et al.*, n.a.; Federal Aviation Administration, 2012a).

2.4.3 Eddy current inspection

Eddy current techniques belong to a kind of electromagnetic testing and are based on analysing conductivity and permeability variations of the material under inspection. A primary magnetic field is generated when alternating current is applied to an induction coil. Eddy currents are induced in a test element when the coil is placed near that element. The alternating current in the coil induces an alternating magnetic field in the element which causes the flow of eddy currents. Thickness changes or flaws in the test element influence the flow of eddy currents and change the impedance of the coil (Finch *et al.*, n.a.; Heuer *et al.*, 2013). Eddy current testing is particularly well-suited for detection of service-induced cracks (Finch *et al.*, n.a.), but also corrosion, surface breakings (Bowkett and Thanapalan, 2017; Finch *et al.*, n.a.), missing carbon fibre bundles (Heuer *et al.*, 2013), porosity, voids, foreign inclusions (Mix, 2005). The limitations of this qualitative method include the limited penetration depth and undetectability of the damage parallel to the scan direction. Moreover, only electrically conductive materials can be inspected (Bowkett and Thanapalan, 2017).

2.4.4 Shearography

Speckle shearing interferometry, or shearography, is an interferometric optical measurement technique that uses the laser speckle and the so-called shear effect. The laser speckle effect occurs when light is scattered from an optically rough surface whose topographical features are greater than the wavelength of the light. When this occurs, a complex granular pattern is produced as the result of the interference of light scattered from different points on the surface. Shearography is derived from a similar technique – Electronic Speckle Pattern Interferometry (ESPI), which is related to holography. The basic principle of shearography involves the comparison of the speckle patterns recorded before and after applying a load to the component under test. Correlation of the speckle patterns offset by the so-called shear vector produces a fringe pattern with the fringes representing contour maps of the measurands. For the composite material testing, a static loading (vacuum, pressure or thermal), or dynamic loading – by inducing a resonant vibration (e.g. with the use of a piezoelectric shaker or an acoustic wave) are often used. Shearogra-

phy is particularly well suited to industrial testing compared with holography and ESPI because of its resilience to environmental disturbances owing to short coherence length requirements, and its direct sensitivity to surface strain (Francis, 2013). This technique is particularly effective in locating debonds and delaminations (Finch *et al.*, n.a.), as well as cracks (Hung *et al.*, 2013). It enables identifying the size and shape of subsurface defects. Shearography is a rapid technique allowing on-aircraft inspections of structures without their removal, as well as inspections of large areas (fuselages and wings) in seconds (Finch *et al.*, n.a.; Ehrhart *et al.*, 2013).

2.4.5 Thermography

Infrared thermography is an NDI technique that uses radiant electromagnetic thermal energy. Thermographic cameras are used to detect infrared radiation of a tested object and produce an image of that radiation. The presence of a defect is indicated by an abnormal temperature distribution when the tested component is subject to normal heating or cooling conditions typical to the in-service life (passive thermography), and/or when artificially heated or cooled (active thermography) (Finch *et al.*, n.a.). Active thermography involves heating the object's surface using an external heat source and observing how the surface temperature decays with time as the heat penetrates or diffuses into the material. Internal flaws in the material show up by variations in both the surface temperature distribution and decay rate. Active thermography can utilise an optical/external excitation, e.g. using a lamp, laser, fluid jets (Lock-in thermography, Pulsed thermography, Step thermography), or mechanical/internal excitation (Vibrothermography) (Ley and Godinez, 2013). Thermography can be used for detecting impact damage, inclusions (Fowler *et al.*, 2001), delamination, debonds, cracks, and water ingress (Ehrhart *et al.*, 2013; Federal Aviation Administration, 2012a). Thermographic methods are suitable for fast inspecting of large areas and can be quantitative, but their accuracy is dependent on thermal conductivity of the tested component (Ehrhart *et al.*, 2013) and are most effective for thin laminates or for near-surface defects (Federal Aviation Administration, 2012a).

2.4.6 Acoustic emission testing

Acoustic emission (AE) methods are based on the principle that a defective structure should generate an acoustic answer, i.e. a transient elastic wave, by sudden redistribution of stress (Ehrhart *et al.*, 2013). The AE sources are the fracture mechanisms or deformation phenomena, such as crack initiation and growth, micro-structural separation, and dislocations between material phases. The AE inspection involves the placing

of acoustical-emission sensors at various locations on the aircraft structure and then applying an external load or stress (Federal Aviation Administration, 2008). In the case of the aircraft fuselage the pressure-induced stress can be applied (Finch *et al.*, n.a.). There are several disadvantages of this method. First of all, it is a qualitative method. Secondly, flaws that do not move or grow cannot be detected (Mix, 2005). Moreover, the noise, attenuation and anisotropic properties of PMCs may pose challenges for the AE data analysis (Huang, 2013). Slight movement of riveted or bolted joints can also generate acoustic signals. These unwanted AE sources significantly complicate the AE tests of complex structures (Finch *et al.*, n.a.). AE monitoring using in PMCs can be used for detection of matrix cracking, delamination, debonding, or fibre breakage. AE measurements can be also used for real-time and continuous monitoring of the structure condition (Huang, 2013; Bowkett and Thanapalan, 2017).

2.4.7 Radiographic and tomographic inspection

Radiography is based on the principle of absorption of the penetrating radiation (X-ray or gamma-ray (Civil Aviation Authority, 2010)) by a tested component. Variances in absorption of the radiation occur due to differences in density, thickness, sizes, shapes, absorption characteristics, or, due to the presence of defects in the material. During a radiographic inspection, the unabsorbed radiation that passes through the tested element is recorded on a radiographic film, fluorescent screens, or other radiation monitors (Finch *et al.*, n.a.; Bowkett and Thanapalan, 2017). Radiography successfully reveals the inner defects of composite elements, such as delamination, cracks, foreign inclusions, voids, or water moisture. However, since the method records changes in a total density through the thickness, it is not a suitable method for detecting defects that are not parallel to the beams (Federal Aviation Administration, 2012a). Other drawbacks of this method are the high costs and strict health regulations.

Computed Tomography (CT) is another radiological technique with enhanced flaw detection and location capabilities. Unlike film radiography, CT involves the generation of cross-sectional views instead of a planar projection (Finch *et al.*, n.a.). CT enables displaying the three-dimensional views of the inspected component and better detection of small defects, such as pores, voids, cracks, etc. (Ehrhart *et al.*, 2013). The spatial resolution of the current CT technology is lower than $1\text{ }\mu\text{m}$ (Kastner *et al.*, 2013), which allows for detection and precise characterisation of even single fibre breakage in an FRP composite structure. Analysis of tomograms (CT scans) is difficult due to existence of numerous artefacts, which usually appear in a form of streaking, shading, rings, or distortion of the

image (Barrett and Keat, 2004) due to the very high sensitivity of this method. CT has the serious limitation regarding the possible dimensions of tested elements, i.e. they must fit in a tomograph chamber. Therefore, CT is suitable only for laboratory tests and cannot be used neither in field conditions nor as a regular NDT method for aircraft composite elements.

2.4.8 Ultrasonic inspection

UT is one of the most universal NDT methods used for composite structures (Davis, 1989) and is the primary inspection method for the aircraft/aerospace industry (Hsu, 2013). The reason for such applicability of UT is its high sensitivity to various damage types commonly found in composites, such as delaminations, debonds, foreign object inclusions, cracks, voids, or porosity (Finch *et al.*, n.a.; Smith, 2009). Using this method, it is possible to precisely determine a geometry of internal defect or damage, its surface area and the depth location.

Phenomenology and fundamentals of UT

Ultrasonic inspections are based on the fact that elastic waves propagate in solid materials and are reflected at the interfaces and by internal flaws or damage (material separations, inclusions, etc.). This method consists in the transmission of ultrasonic waves into a test material and observation of the reflected waves (Pulse-Echo technique), or the transmitted waves (Through-Transmission technique). Pulse-Echo systems require only one-sided access to the element being tested, thus are practically used for the in-service inspections, whereas Through-Transmission technique is widely used in manufacturing. The most common UT methods apply longitudinal and transverse (shear) waves, however, other forms of the elastic waves propagation are also used, including Rayleigh and Lamb waves. Most ultrasonic transducers operate on the piezoelectric principle of transconductance, i.e. they transmit an ultrasonic pulse when excited by an extremely short electrical discharge, and generate an electrical signal when they receive the returned ultrasonic signal (Berke, 1996). This mutual conversion is accomplished by a plate of polarized ceramic or crystalline material with electrodes on the opposite surfaces. Transducers are designed for contact testing or immersion testing. Most contact transducers require applying a coupling agent (e.g. water, thin film or oil, contact paste, or glycerin) between the probe and the test element surface because air attenuates most of the ultrasonic energy. In the immersion testing, the elastic waves are transmitted into the material through a water path or a liquid column. Flaw detection is possible because of the difference in

acoustic impedance of various materials, which is a measure of resistance to propagation of ultrasonic wave in a material. Ultrasonic waves are reflected at the interface of two different materials or other discontinuities, when the mismatch in acoustic impedance occurs (Mix, 2005). The general principles of ultrasonic examination are wider presented in the PN-EN ISO 16810:2014 standard (Standard, 2014a).

It should be mentioned that there is also an air-coupled UT technique. It eliminates the necessity for a liquid couplant and can be applied to such structures as honeycomb sandwich with perforated face sheets. The greatest challenge in air-coupled UT is the enormous loss of ultrasonic energy at the air-solid interface; therefore, special transducer types are used. For a piezoceramic type of an air-coupled transducer, the special material layers are used to bridge the high acoustic impedance of the transducer element and the low impedance of air (Hsu, 2013).

UT results visualisation and evaluation

Two fundamental parameters of the received ultrasonic energy are observed: the relative amount (amplitude), and its occurrence in time domain with respect to a zero point (Time-of-Flight – ToF). Three basic types of UT inspection result visualisation are so-called A-Scan, B-Scan, and C-Scan presentation modes (see example in Fig. 2.10(b)).

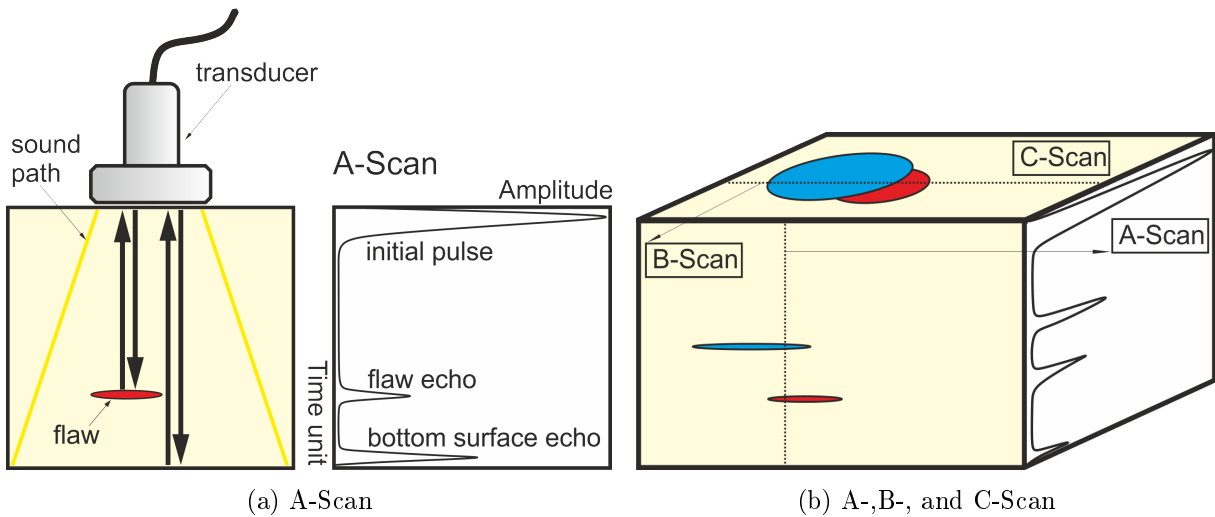


Fig. 2.10: Schemes of basic modes of UT results visualisation

The A-Scan displays a one-dimensional signal, which is the amount of the received ultrasonic energy as a function of time (Fig. 2.10(a)). The time measurement starts with the electrical transmission pulse (i.e. the initial pulse or front surface indication). The pulse travels through the test material and is reflected by a discontinuity and/or the back wall and returns back to the probe. The received oscillations are converted into an electrical

pulse which stops the time measurement (Berke, 1996; Mix, 2005). It should be noted that when the ultrasonic wave comes across the discontinuity, the echo from the bottom surface will have lower amplitude than in the case when there is no discontinuity. Moreover, if the discontinuity is large enough, the echo from the bottom surface may disappear. There are different A-Scan display modes, which will be discussed in section 4.1.2.

The B-Scan presents a two-dimensional map, reflecting the cross section of the inspected structure (Fig. 2.10(b)), which is obtained by merging the A-Scans acquired along a path followed by the UT transducer.

The C-Scan is a two-dimensional map, presenting damage in the plan view of the test element (Fig. 2.10(b)), obtained by extracting some limited information from all the B-Scans. For a given point on the map, the amplitude C-Scan carries the information about the maximum value of the signal amplitude acquired at this point and the ToF C-Scan represents the ToF of the signal component with the highest amplitude, which usually corresponds to the damage located the closest to the surface of the inspected structure.

Having known the material's sound velocity c (km/s) and the calculated sound pulse's ToF t (μ s) from the probe to the flaw and back it is possible to determine the depth of the flaw s (mm) by the following simple formula (Berke, 1996):

$$s = \frac{ct}{2}. \quad (2.1)$$

Appropriate processing and analysis of ultrasonic scans allow for the damage detection, localisation, characterisation, as well as quantification. By the separation of damage from a "background" (i.e. the underlying healthy regions of the test structure) visible in the C-Scan, i.e. extraction of its contour, it is possible to calculate the damage extent. However, a measurement uncertainty should be taken into account when interpreting the UT results, which follows from many various factors. These factors include, for instance, the test material parameters and selection of the operating parameters, which will be discussed in detail further, in section 4.1.

Other ultrasonic techniques for bond testing

Apart from the traditional UT methods described above, the integrity of bonds in the multi-layered adhesively bonded structures can be tested using so-called bond testers. Modern bond testers operate in three testing modes – a Resonance, a Pitch-Catch and a Mechanical Impedance Analysis (MIA) mode. Bond testing can be regarded as an electronic form of tap-testing (see section 2.4.2), but with continuous excitation rather than impulse (Fowler *et al.*, 2001; Crompton, 2014; Federal Aviation Administration, 2008).

Compared to the conventional UT techniques, bond testers operate at lower frequencies, typically between 4 kHz–400 kHz (Crompton, 2014). The Resonance, Pitch-Catch, and MIA testing modes all have several similarities and the measurement metric is a variation in the amplitude and/or phase of the elastic wave transmitted into the material. The second common principle is that the result is a relative measurement between a good and a flawed area of the structure. These modes vary, among others, in terms of a way of coupling, a frequency range (a swept or fixed frequency; a low, medium or high frequency), and sensitivity to various damage types and sizes. The bond testers enable detection of delamination, disbonds, impact damage, foreign objects, voids, porosity (Crompton, 2014; Ehrhart *et al.*, 2013), as well as water ingress in honeycomb sandwich structures (Ehrhart *et al.*, 2013). The main disadvantage of bond testing is that it is qualitative and suitable only for near-surface damage detection (Fowler *et al.*, 2001).

Ultrasonic inspections in the aircraft industry

In the aircraft industry, there are many inspection programmes of service life extension of aircraft elements implemented in accordance with the CBM or damage tolerance maintenance methodologies. One of the major tasks of maintaining airplanes following these maintenance approaches is to perform NDT inspections of their critical elements. For instance, according to the review of aeronautical fatigue investigations in Poland (2013–2014) presented in (Niepokólczycki *et al.*, 2016), such programmes in the military aviation were established for main rotor blades of helicopters (such as Russian-made Mi-2, Mi-8, Mi-17, Mi-14, and Mi-24), vertical stabilizers of MiG-29 (a basic fighter jet used in the Polish Air Force), elements of Sukhoi SU-22 (a close air support aircraft), and PZL-130 ORLIK (a light aircraft used for pilot training).

The ultrasonic instruments used for NDI of the aerospace composites range from small portable manual ultrasonic flaw detectors to large fully automated scanning systems (Hsu, 2013). In the case study (Dragan and Synaszko, 2009) concerning NDT&E of composite skins of MiG-29 vertical stabilizers performed in the AFIT, the authors paid attention to the enormity of the examined areas. It was noted that the total surface area for the ultrasonic inspection was approximately 11 m² per one aircraft. The aircraft population selected to these tests were more than 30, so the total area for the inspection was more than 360 m². To meet the need for systems that are portable for on-aircraft application and can provide quantitative scan data of such large areas, automated ultrasonic systems are used. The exemplary from the performed in the AFIT inspections of MiG-29 using a mobile automated scanner MAUS[®] of Boeing[®] is presented in Fig. 2.11(a).

Such a vertical stabilizer consists of the aluminium substructure and the composite

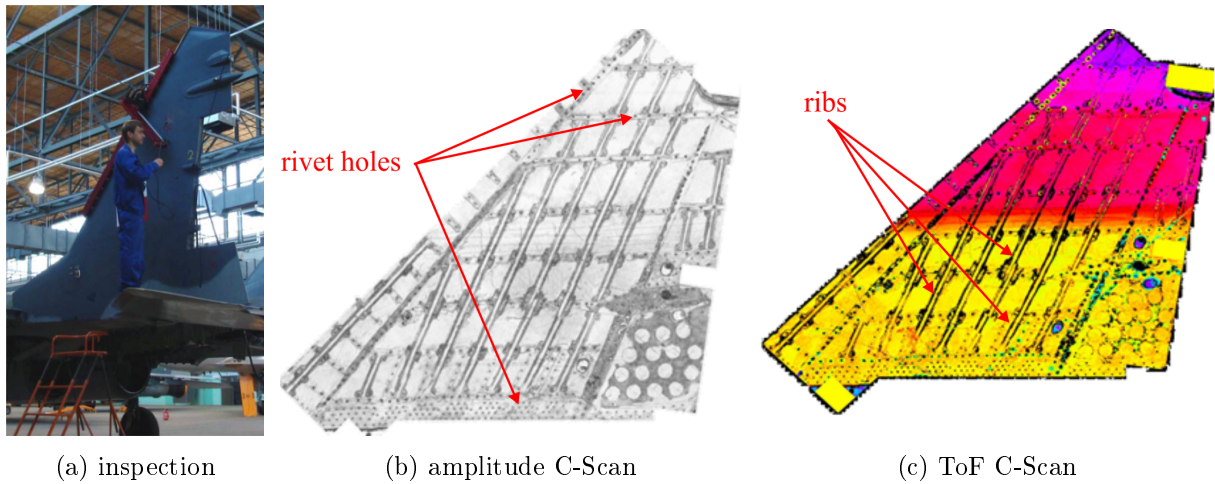


Fig. 2.11: Ultrasonic inspection of a vertical stabilizer of MiG-29 carried out by the AFIT and the exemplary results (adapted from (Dragan and Synaszko, 2009))

skin made of CFRP. The skin is monolithic with a thickness in the range of 1.8–3.2 mm and is joined to the substructure with the use of rivets and adhesive (Dragan and Synaszko, 2009). The variable thickness of the tested composite skins and the presence of openings for riveted connections and stiffening ribs (see Fig. 2.11(b,c)) complicate interpretation of UT results. The variable thickness of the composite skin results in respectively variable ToF of the ultrasonic wave during testing, which is visible in Fig. 2.11(c) as a monotonic change in a colour in a vertical direction of the scan, while the black regions represent the ribs and rivet holes.

The exemplary C-Scans of the aircraft vertical stabilizers with localised defects and damage of various types are presented in Fig. 2.12. In Fig. 2.12(a,b), the presence of porosity was identified by the observation of the area where the signal was attenuated by the presence of air (visible as the cluster of black pixels in the ToF C-Scan). In Fig. 2.12(c,d), one can observe delamination areas around inspection hatches and rivet holes, probably caused by over-tightening during assembly, as well as disbonds formed between the skin and the ribs. These delaminated regions are observable in a form of areas with sudden changes in a colour.

2.5 Application of image analysis methods in ultrasonic inspections

As a preliminary remark, a difference between two terms, namely: image processing and image analysis, should be pointed out. Image processing relies on performing some trans-

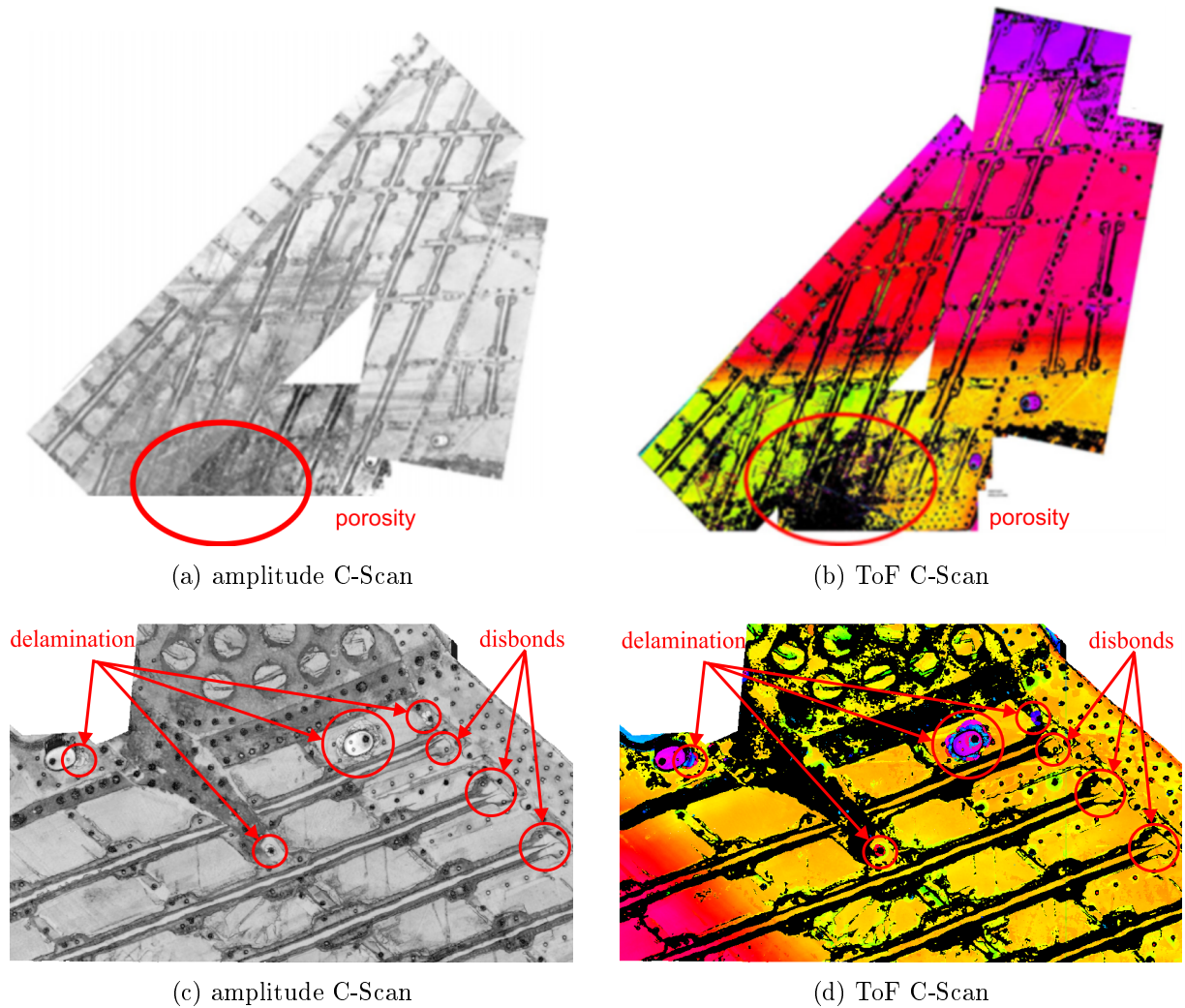


Fig. 2.12: Exemplary defects and damage types located in vertical stabilizers of MiG-29 (adapted from (Niepokólczycki *et al.*, 2016))

formations on an image in order to obtain a modified (enhanced) image. Image analysis, in turn, is also based on transformations, however, it returns additional information representing a description. In the case of the application of image analysis to ultrasonic C-Scans the result can be, for instance, the damage contour and its surface area.

For the purpose of damage quantification based on the obtained during inspection C-Scans, an UT operator performs a thorough analysis of the C-Scans and calculates the damage extent using a software dedicated to UT. There are several standardised methods of the defect sizing by the appropriate post-processing of C-Scans. Commonly applied are the measures based on Signal-to-Noise Ratio (SNR), such as so-called 6 dB drop method provided in the PN-EN ISO 16827:2014 standard (Standard, 2014c). This method is applied to the amplitude C-Scans and has certain shortcomings, which will

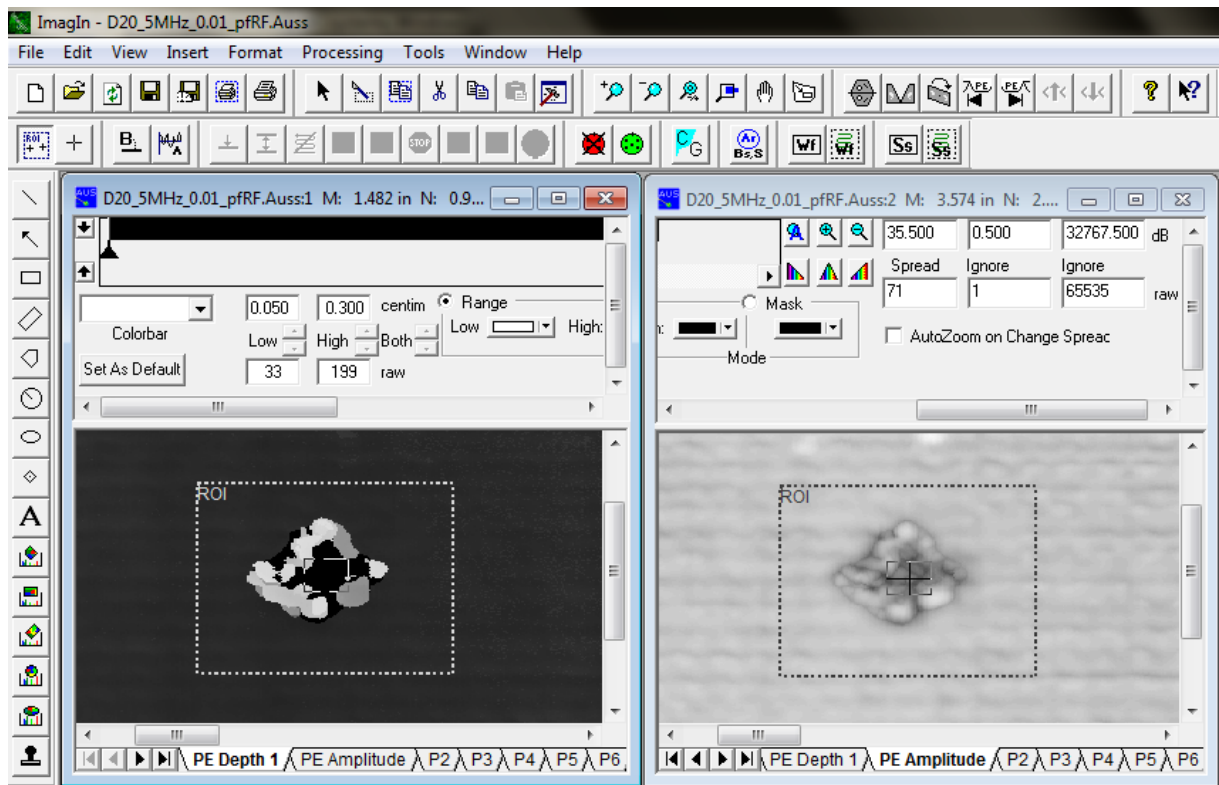
be discussed in section 4.1.4. However, there is a need of the application of a second – reference method for the damage quantification, which typically exploits the ToF C-Scan maps. The ToF C-Scans are more convenient for this purpose since they are obtained after filtration of the ultrasonic signal unlike the amplitude C-Scans that contain all noise. This makes the border between the damage and the underlying material more distinct and thus they are easier to be separated.

In practice, the damage is usually quantified based on manually selected areas on the obtained C-Scans. One of the examples is presented in the paper (Meola *et al.*, 2015), where the overall delamination extension of CFRP composites was estimated by calculating the average diameter after the manual selection of the region of interest (ROI) in a rectangle. In the paper (Hasiotis *et al.*, 2011), defects detected in a composite structure were analysed by means of ULTRAWIN[®] software. In this case, the defects were sized after their isolation by selection of a group of data with the amplitude greater than 70% of a full screen height. Other example of the defect sizing in composite structures can be found in (Mašonkina and Kalniņš, 2013), where Oculus[®] software was used that enables changing the palette of colours to enhance the analysis of the signal amplitudes distribution.

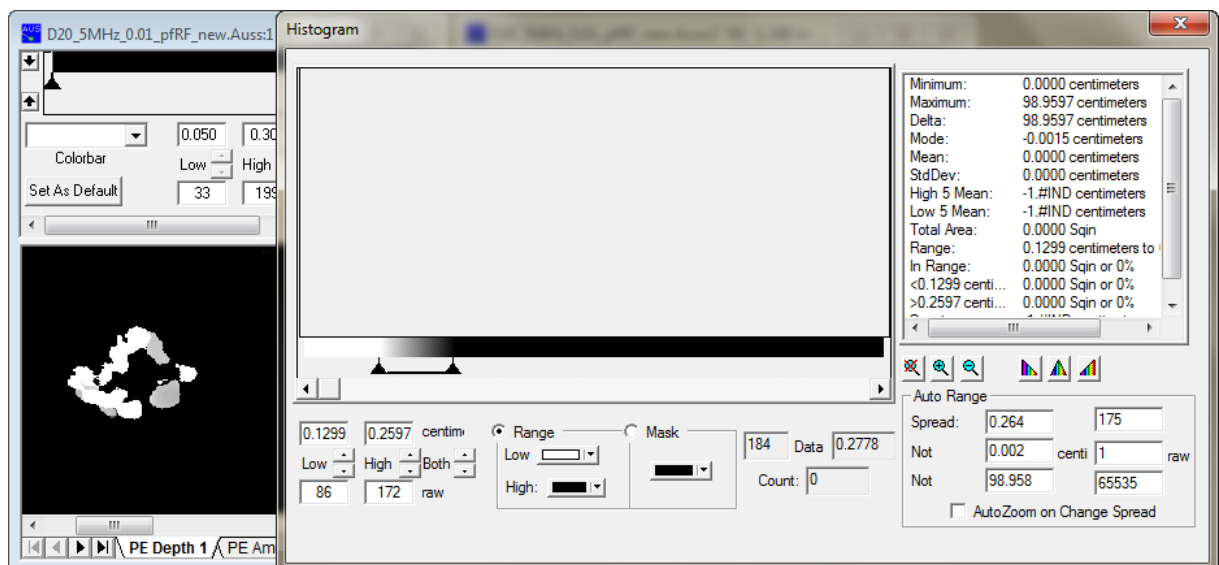
In the case of NDIs performed by the experts from the AFIT, ImagIn[®] software is used for the analysis of ultrasonic scans, which is the inherent element of the MAUS[®] system. This software provides simple tools, such as geometrical shapes and a text editor for making annotations on the scan, a tool for ROI selection (Fig. 2.13(a)), or sliders for manual changing the range of the image histogram, i.e. the displayed pixels' values (Fig. 2.13(b)).

Such analyses may bring unrepeatable results since some manual settings can be selected differently when analysed the data in a different period of time or by another UT operator. Another reason is the human factor which may be introduced due to excessive numbers of data to be analysed. As mentioned earlier, the risk of human error is difficult to be eliminated. A particular problem are the large sizes of the scans and the high time-consumption of the analysis. Due to the necessity of increasing the efficiency of ultrasonic inspections, i.e. shortening the duration of UT data analysis, the application of image processing and analysis methods is one of the presently undertaken goals. In the literature, one can find research studies that address the application of image processing methods to aid the damage detection and evaluation procedures, which will be discussed in section 4.2.1. There are also some works dedicated to 3D visualisation of damage, which will be introduced in section 4.3. Such a visualisation may provide an additional support for the operator who analyses the ultrasonic scans and facilitate their interpretation. However, most of the studies were developed for a specific problem or structure

tested and they are not universal. No studies were found in the literature that aimed at a comprehensive analysis and/or comparison of various methods of image processing and analysis in the light of accuracy of damage detection and evaluation.



(a)



(b)

Fig. 2.13: Exemplary tools for a C-Scan analysis available in ImagIn[®] software (the presented C-Scans concern a CFRP specimen with BVID)

3. Research problem

Having regard to the current state of knowledge in terms of the application of image analysis methods for the purpose of aiding the ultrasonic evaluation of composite aircraft elements, the research problem can be identified and the objectives, hypothesis, and scope of the thesis formulated.

3.1 Identification of the research problem

The problems described in section 2.5 regarding the necessity of increasing the efficiency of ultrasonic inspections by aiding the analysis of ultrasonic scans have been the motivation towards the undertaken research. Namely, this need arose from several difficulties in analysing the ultrasonic scans obtained during NDI of composite aircraft components. These inconveniences cover the high time-consumption of such analyses resulting from the large sizes of the scans and the manual handling, i.e. the processing and annotating, of them. This, in turn, may lead to the unavoidable occurrence of the human error and unrepeatable results.

For the best of the author's knowledge, there are no tools available dedicated to ultrasonic scans for aiding the process of damage detection, evaluation, and enhanced visualisation that are reliable and universal for any type and internal architecture of a composite structural element as well as any damage type and shape. There is a lack of knowledge whether the application of various image processing and analysis methods could be helpful in solving this problem so that they were effective and highly accurate, which is critically important in the case of NDE of the aircraft structures.

The formulated research problem is therefore to investigate how to facilitate the procedure of the damage detection, evaluation, and enhanced visualisation based on ultrasonic data obtained during NDIs of composite aircraft structures so that it was universal, quick and the obtained results were highly accurate and reliable.

3.2 Research objectives

The main goal of the dissertation is to increase efficiency and reliability of damage detection and evaluation including its localisation, characterisation, quantification, as well as enhanced (3D) visualisation. The objective is associated with improving and facilitating the currently implemented procedures of diagnostics of composite aircraft elements based on ultrasonic testing.

This is planned to be achieved by the additional development of algorithms based on image analysis methods. The developed methods and algorithms could be included as elements of an expert system. It should be pointed out that the analysis of the ultrasonic scans cannot be performed without the supervision of a certified expert since the full automation of the algorithms may result in errors, which is unacceptable in the case of NDE in the aircraft/aerospace industry. The expert should have the possibility of deciding which scan regions represent the damage and which, for instance, the embedded elements inside the diagnosed element. Moreover, the algorithms should be computationally effective, thus allow for performing fast analyses.

3.3 Research hypothesis

Bearing in mind the defined research problem and the research objectives, the dissertation hypothesis was formulated as follows.

It is possible to increase efficiency and reliability of diagnostics of composite aircraft elements based on ultrasonic testing by the development of a methodology with the use of image processing and analysis methods.

3.4 Research scope and plan

For the research, the most commonly applied type of composite structures for the aircraft elements was considered, namely the CFRP composite. This includes both artificially damaged specimens as well as aircraft components with damage induced during in-service. To achieve the objectives determined in the thesis and verify the set hypothesis it was planned to perform the research stages as follow.

1. ***Analysis of the measurement uncertainty factors in the damage detection and evaluation.*** This stage includes performing a thorough review on the factors, such as the test material parameters and applied operating parameters for

UT, that influence on the damage detection sensitivity and the measurement error (see section 4.1). Various combinations of basic UT methods and variable operating parameters were tested on CFRP specimens with flat-bottom holes (FBHs) of known dimensions in order to determine the damage detectability, calculate the measurement error and select the most appropriate testing parameters for the used in the research structures (see chapter 5).

2. ***Analysis of damage detection accuracy using image segmentation methods.*** This stage covers performing a review on the studies connected with the application of image analysis methods to aid the damage detection from ultrasonic scans and a broad review of image segmentation methods that potentially could be applied for this purpose (see section 4.2). After that, a comparative analysis of the application of various image segmentation methods to the ultrasonic scans, including the proposed approaches, was performed in the light of the damage detection accuracy. The most suitable methods were selected having regard to the objectives of the algorithm to be accurate, efficient and universal (see chapter 6).
3. ***Analysis of 3D damage reconstruction and visualisation.*** This stage includes performing a review in the area of the application of image processing methods aimed at the 3D damage visualisation (see section 4.3). Afterwards, the algorithms of the 3D damage reconstruction and visualisation based on a C-Scan and a series of B-Scans of a specimen with BVID were proposed. The accuracy of the reconstructed BVID geometry inside the specimen was verified on the basis of the reference data acquired with the X-ray CT method (see chapter 7).
4. ***Application of the developed image analysis algorithms to selected problems.*** The developed image analysis algorithms within the framework of the stages 1–3 were tested by the application to selected case studies. These cover impact damage detection and evaluation in CFRP specimens (section 8.1); delamination size monitoring in CFRP aircraft elements (section 8.2); and 3D damage reconstruction and visualisation in CFRP aircraft elements (section 8.3).

4. Related works

This chapter includes reviews on research works related to the aspects raised in the next chapters. It is divided into three sections covering the reviews on:

1. measurement uncertainty factors in damage detection and evaluation,
2. damage detection using image analysis methods, and
3. 3D damage reconstruction and visualisation using image processing.

The performed experiments and own developed methods connected with these three sections are presented correspondingly in chapters: 5, 6, 7.

4.1 Measurement uncertainty factors in damage detection and evaluation

Ultrasonic inspection, when properly performed, enables determining the geometry of internal damage, its surface area and depth location. However, measurement uncertainty should be taken into consideration when interpreting UT results, which follows from numerous factors that influence on the flaw detectability and its size evaluation. The main factors include the test material parameters (for instance acoustic impedance, attenuation, and flaw characteristics), and the selection of the operating parameters, such as the scanning technique and transducer characteristics (e.g. the type, frequency, diameter of an active element). Moreover, the uncertainty in the flaw size assessment is caused by signal or image processing methods applied to the obtained ultrasonic scans, which may return incorrect results. This section presents an overview of the factors affecting the UT measurement uncertainty with reference to appropriate standards. The review presented in this section was included in (Wronkiewicz *et al.*, 2018a).

4.1.1 Material parameters

Wave interactions

It is well-known that elastic waves may interact with materials in various ways depending on the material parameters (e.g. the geometry, material properties) and other factors such

as, for instance, an angle of incidence. In homogeneous medium, elastic waves propagate uniformly and are transmitted through the object without interacting (Fig. 4.1(a)). Reflection (Fig. 4.1(b–d)) and refraction (Fig. 4.1(e)) occur at the boundary between two media with different characteristic acoustic impedances or different speeds of sound. It should be noted that the angle of reflection is always equal to the angle of incidence (Mix, 2005), whereas the angle of refraction is dependent on the angle of incidence and can be calculated using the Snell's Law. Diffraction, dispersion, and attenuation are hard to quantify because of undefined transducer, flaw, and material variations. Diffraction involves a change in direction of waves when they pass through a small gap (Fig. 4.1(f)) or around a barrier in their path. The dispersion has a definition similar to diffraction and occurs due to rough and irregular surfaces. These surfaces reflect the ultrasonic energy in directions that cannot be detected by the transducer. Scattering occurs when the wave bounces off an object in many different directions (Fig. 4.1(g)). The main mechanisms contributing to ultrasound attenuation (Fig. 4.1(h)) is absorption, diffraction, scattering, as well as possible coupling losses.

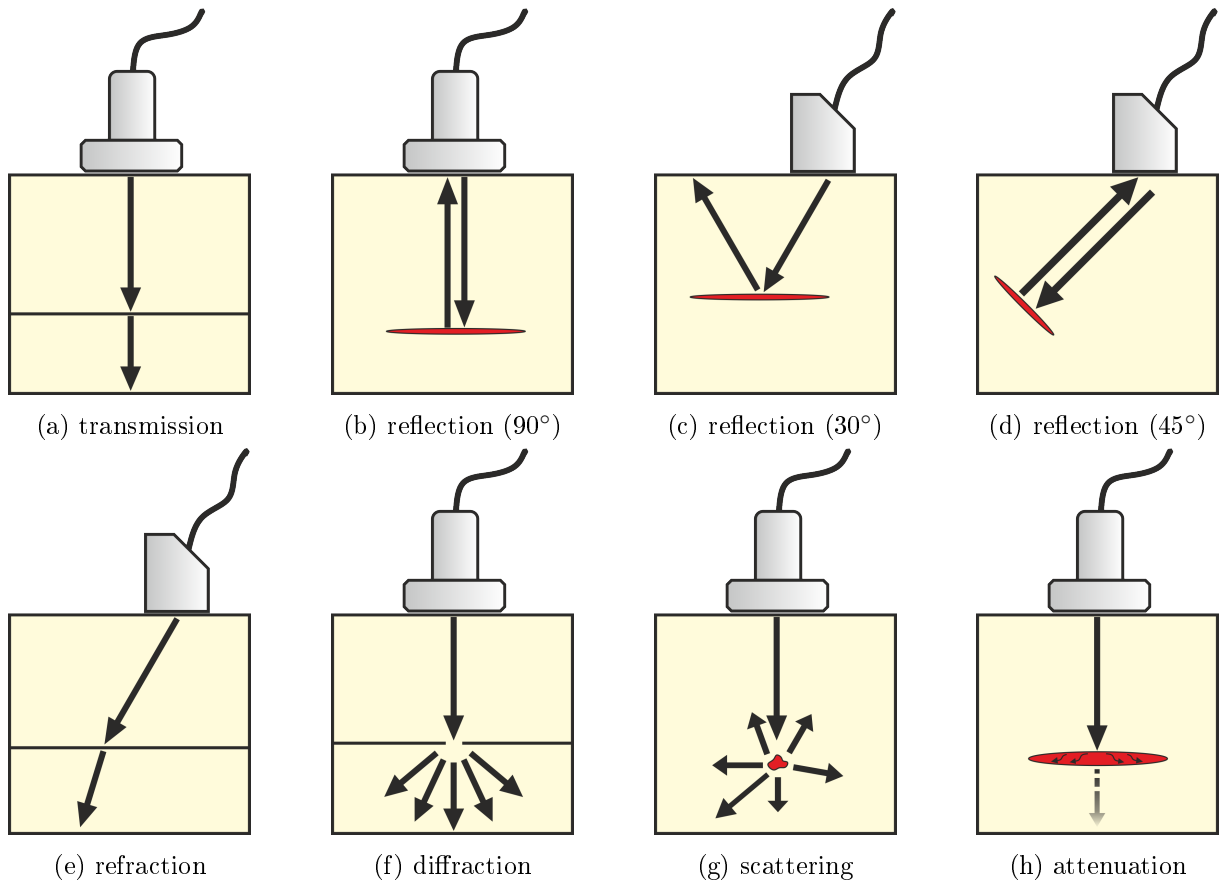


Fig. 4.1: Examples of basic wave interaction scenarios

Some material properties affecting attenuation are heat conduction, grain size, viscous friction, mechanical hysteresis, and modulus of elasticity (Mix, 2005). Absorption occurs when the incoming wave hits an object and causes its atoms to vibrate, converting the energy into heat which is radiated. Some of these interactions may cause the ultrasound wave not to return to the probe or return with a significantly lower amplitude.

Flaw characteristics

The echo amplitude is strongly dependent on the discontinuity characteristics, i.e. its geometry, orientation to the ultrasound beam and the surface quality (Berke, 1996). Moreover, a discontinuity size and depth location also influence on the received echo, which is directly connected with the UT operating parameters and described in section 4.1.2.

The direction of the ultrasound wave has a big influence on its portion returned to the probe after being reflected by the discontinuity. A plane (two-dimensional) flaw (e.g. crack, delamination) reflects the ultrasonic waves mostly in a certain direction (see example in Fig. 4.2(a)). The possibilities of the flaw detection increase when the plane discontinuity is hit horizontally by the ultrasound beam (as in Fig. 4.1(b,d)) (Berke, 1996).

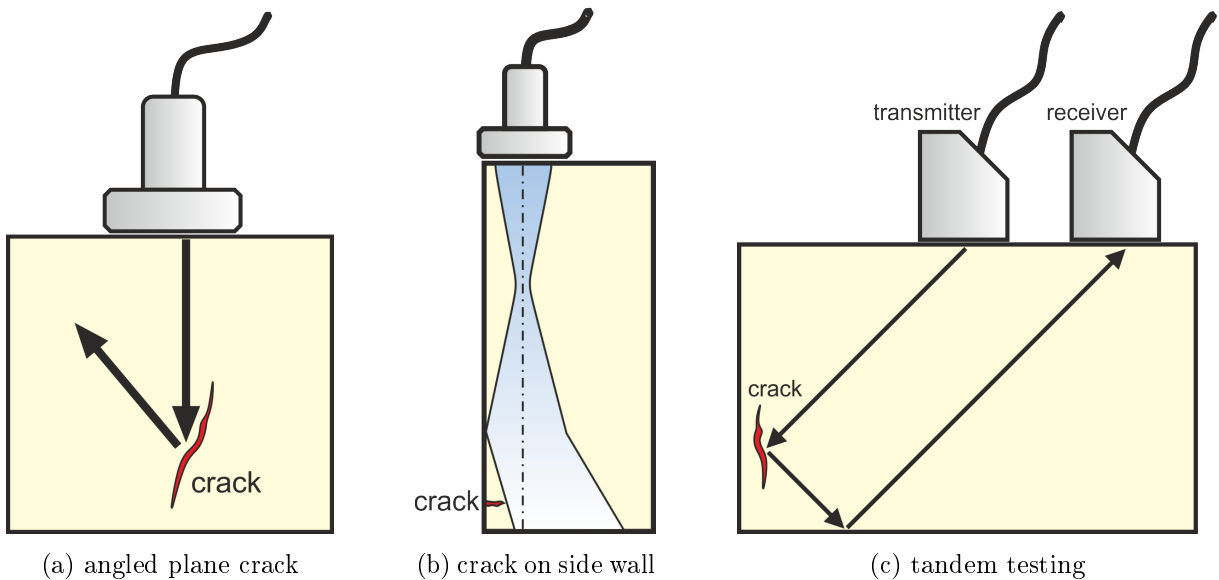


Fig. 4.2: Other factors affecting crack detectability

A volumetric flaw (foreign material, a void) reflects the waves in different directions, which reduces probability of receiving the reflected portion of the ultrasound wave.

Moreover, discontinuities which are open to the surface of the test object, e.g. a crack running vertically from the surface into the test object, might be undetected because of

wave interferences appeared due to ultrasound wave reflection on the object's side wall (Fig. 4.2(b)) (Berke, 1996).

Vertical discontinuities in thick-walled objects are also unlikely to be detected, since the reflected elastic waves do not return to the probe. In such cases, a second probe can be used for receiving the reflected portions of the waves (Fig. 4.2(c)) (Berke, 1996).

4.1.2 Operating parameters

There are numerous variables of operating parameters during UT that have a significant influence on the obtained results. These factors include, among others, the selected scanning technique and equipment type, transducer characteristics, coupling method, and problems with noise (caused by external radio frequency (RF) interference, internal signal-to-noise characteristics of the equipment, dirt, air bubbles, etc. (Mix, 2005)). A short description of the most important factors is presented below.

Transducer type

The transducer is one of the most critical components of any ultrasonic system. A great deal of attention should be paid to selecting the proper transducer. In general, conventional ultrasonic transducers consist of either a single active element that both generates and receives ultrasonic waves, or two paired elements – one for transmitting and one for receiving (Tandem Technique). There are also Phased Array probes, which consist of a transducer assembly with multiple (from 16 to 256) small individual elements that are pulsed separately.

Straight-beam probes. Probes whose beams are normal to the test surface are called straight-beam probes (see e.g. Fig. 4.1(b)). Most standard straight-beam probes transmit and receive longitudinal waves (Berke, 1996). Straight-beam testing is very effective in detecting parallel, laminar, or planar flaws in plates (e.g. delamination). With straight-beam testing, non-parallel surfaces (e.g. transverse cracks as in Fig. 4.2(a)) may cause partial or total loss of the back reflection (Mix, 2005).

Angle-beam probes. Probes transmitting and receiving the elastic waves at an angle to the surface of the test object are called angle-beam probes. Most standard angle-beam probes transmit and receive transverse waves or shear waves. During scanning with the use of angle-beam probes, the refraction law should be taken into consideration. Although with angle scanning in thin test objects there is a risk that plane discontinuities cannot be

vertically hit (e.g. Fig. 4.1(c)), the detection sensitivity is much better, especially by suitable selection of the scanning angle (e.g. Fig. 4.1(d)) and the test frequency (Berke, 1996). The incident angle necessary to produce the desired refracted wave can be calculated from the Snell's Law.

Tandem Technique. A more complicated angle scanning method is the Tandem Technique, where one probe is used as a transmitter, and the other probe is used as the receiver. Both probes are moved over the surface of the test object and are spaced apart at fixed distance. This method is useful for detecting vertically positioned discontinuities (see e.g. Fig. 4.2(c)) (Berke, 1996).

Delay line transducers. For testing thin materials, such as composites, delay line elements are attached to the contact-type transducers in order to separate the initial pulse from the reflected waves. The delay line allows the crystal element to stop vibrating before returning of the reflected signal, so that near-surface resolution is improved.

Transducer frequency

Selection of the test frequency depends on the required sensitivity (i.e. the ability to locate small flaws), ultrasound penetration depth (depending on the thickness of the test object), or required resolution (i.e. the ability to locate near-surface flaws). The relation between the wavelength λ (mm), material sound velocity c (km/s), and frequency f (MHz) is as follows:

$$\lambda = \frac{c}{f}. \quad (4.1)$$

As the frequency increases, the wavelength decreases, which allows for small flaw detection and thickness location precision; while as the frequency decreases, the wavelength increases, which allows for greater penetration into thick and/or attenuating materials (Berke, 1996; Mix, 2005; Olympus Corporation, 2006). It should be noted that the flaw detectability also depends on the transducer bandwidth, which refers to the range of frequencies associated with the transducer. Namely, narrow bandwidth often improves sensitivity, whereas broad bandwidth improves near-surface resolution. The frequency noted on a transducer is the central frequency. The selection of the test frequency is therefore the trade off between the desired sensitivity and the possibility of the material to be inspected due to the attenuation.

A general rule is that a discontinuity must be larger than one-half the wavelength to have a reasonable chance of being detected (Rose, 1999). Other factors such as near-field

length, and beam diameter also affect the damage detectability and thus the frequency selection, which are discussed further. General recommendations considering the selection of the transducer parameters (frequency, probe dimensions) are presented in the PN-EN ISO 16810:2014 standard (Standard, 2014a).

A useful frequency range of ultrasonic waves in NDT applications is between about 0.5 MHz and 25 MHz (Berke, 1996), whereas composite materials are usually tested within the frequency range of 1–10 MHz.

Distance-amplitude effect and beam diameter

A distance of a flaw from an ultrasonic probe significantly influences on the amplitude of the received signal. Differences in signals received from identical flaws at different depths of a test element may be caused by the material attenuation, beam divergence, or near-field effects (Mix, 2005).

Near field and far field. Ultrasonic transducers produce ultrasound beam patterns composed of two zones (Fig. 4.3(a)): a convergent (focusing) area – the near field (or the Fresnel zone) and a divergent (spreading) part – the far field (or the Fraunhofer zone) (Berke, 1996; Mix, 2005). The shape of the ultrasound beam, including the near-field length N and the divergence angle γ , plays an important role in the probe selection. In the near field, fluctuations in ultrasound pressure (the interference fields) occur, which makes the evaluation of flaws positioned within this area using the amplitude-based techniques very difficult. The near-field distance N is a function of the transducer frequency f , crystal diameter D , and the sound velocity c of the test material (Olympus Corporation, 2006):

$$N = \frac{D^2 f}{4c}. \quad (4.2)$$

Moreover, the beam divergence is dependent on the transducer frequency and diameter. As the diameter of the transducer decreases, the beam divergence is increased, and vice versa. Beam divergence is also greater for lower frequency transducers.

Near-surface discontinuity. Another problem is a so-called dead zone, which refers to the front surface pulse width and recovery time. When a small discontinuity is just below the surface of the test object, the intermediate echo is then within the initial pulse, and therefore covered by it (Fig. 4.3(a)). However, when the discontinuity is large enough and shadows a noticeable part of the ultrasound beam, the back-wall echo becomes smaller, which may be the indicator of the existing near-surface discontinuity (Fig. 4.3(a)) (Berke, 1996).

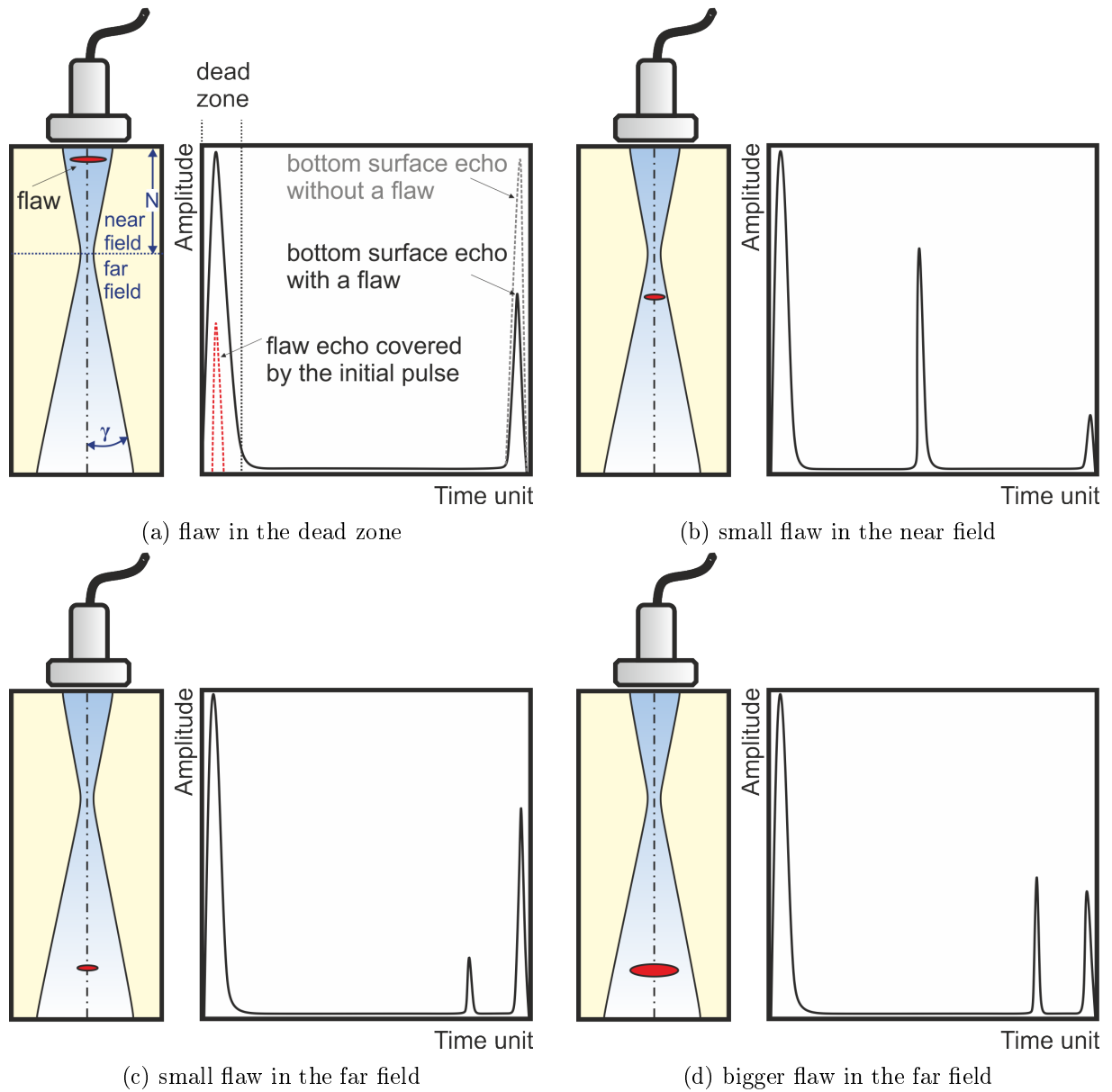


Fig. 4.3: Influence of a flaw size and location on the echo amplitude

Small discontinuities and beam diameter. There are difficulties in the evaluation of small discontinuities that are contained within the ultrasound beam. The evaluated size of such a discontinuity using UT is not the size of the flaw, but the diameter of the ultrasound beam. The echo amplitude is greater the larger the ultrasound beam area is, which covers the flaw. A general rule can be assumed for such small flaws that their echo heights increase with their areas (Berke, 1996) (cf. Fig. 4.3(c) and Fig. 4.3(d)).

Similar effect occurs when evaluating a boundary of larger defects, namely, location of the boundary becomes more exact the smaller the diameter of the ultrasound beam is at the flaw position (Berke, 1996).

Moreover, additional distance dependence of the echo heights for the same discontinuities positioned at different depths is established. This dependence is valid only for the far field of the ultrasound beam and assumes that the echo heights inversely reduce to the square of their distance (cf. Fig. 4.3(b) and Fig. 4.3(c)) (Berke, 1996).

Echo display and rectifier modes

Another factor, which is important during interpretation of ultrasonic data, is the echo display (and capturing) mode. The raw voltage signal, produced by the transducer during receiving the reflected ultrasonic pulses, is inconvenient for the display purposes at an ultrasonic system screen. For this reason, these voltages must be processed by the amplifier and associated electronics before they can be displayed in the useful format. The required operations are carried out by the electronic receiver, whose most important function is amplification of the voltages. The raw echoes are initially processed as RF waveforms, which represent the positive and negative voltages associated with the positive and negative pressures of the acoustic waves. One of the processing operations is rectification, in which the negative voltages are converted to positive values, and then the rectified RF waveform is smoothed using a low-pass filter, producing the signal envelope.

Nevertheless, there are different kinds of single A-Scan presentations possible (see Fig. 4.4): both half waves unrectified RF, positive half wave, negative half wave, or full wave – rectified and unfiltered, or rectified and filtered.

The RF display mode is useful when working with very thin test elements. Half wave positive rectification shows only the positive peaks, while half wave negative rectification shows only the negative peaks, flipped to the positive side of the baseline. Full wave rectification displays both positive and negative echo lobes together on the positive side of the baseline (Olympus Corporation, n.a.). Selection of the display mode of the signal rectification should be carefully accomplished. For the elastic waves propagation the phase change during reflection, which is basically a phase inversion due to the impedance change, may occur.

4.1.3 Calibration

Obtaining reproducible UT results assumes knowledge of the influencing factors described in the previous subsections. However, not all of them have to be seriously regarded by the operator and some of them can be neglected due to permitted measurement tolerances. The measurement uncertainty can be reduced by exploiting a reference block made of the same material as the test object, with artificially introduced flaws of known dimen-

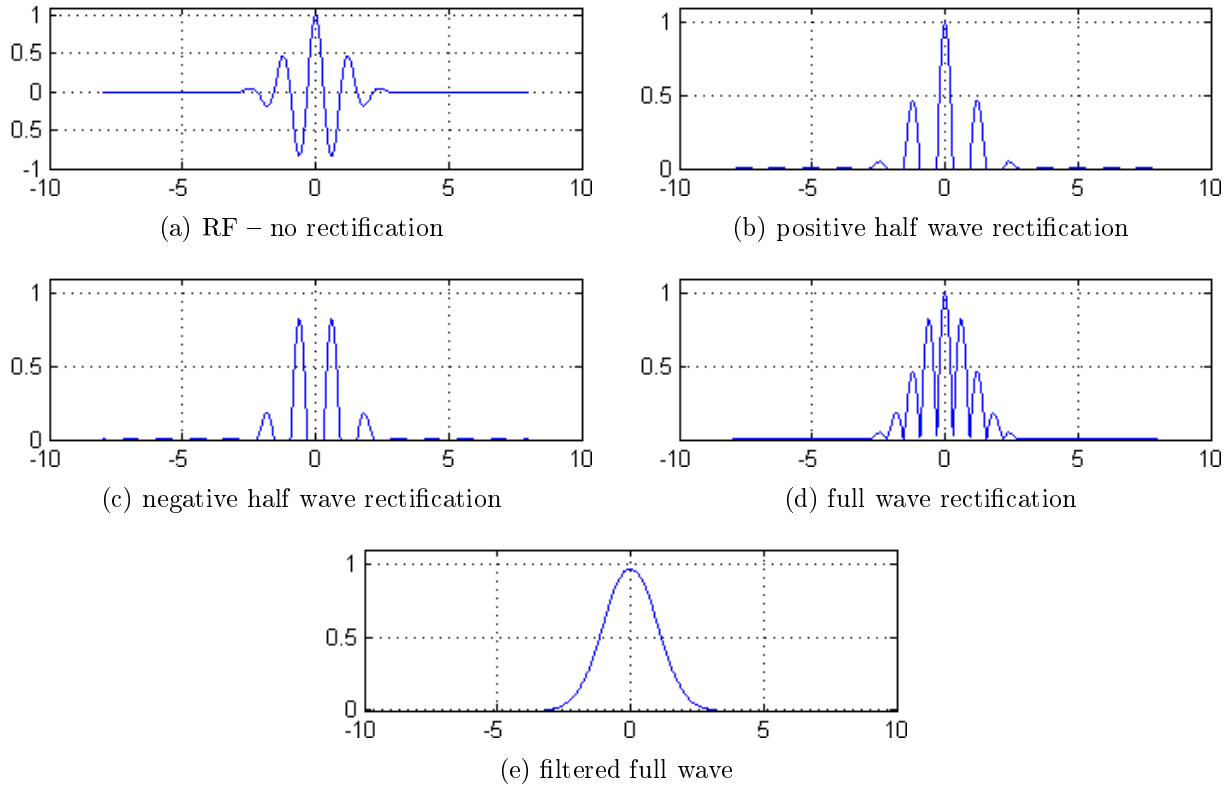


Fig. 4.4: Illustrative examples of the echo display modes

sions (usually FBHs of various diameters) (Berke, 1996; Mix, 2005). According to the PN-EN ISO 16810:2014 standard (Standard, 2014a), the surface condition (roughness) and geometrical condition of the calibration block should also be comparable with the structure to be examined. The detailed description of the sensitivity and timebase range setting for manually operated UT flaw detectors is provided in the PN-EN ISO 16811:2014 standard (Standard, 2014b). There are different methods for calibration of UT equipment using the reference block method, e.g. by comparison of echo amplitudes, Distance Amplitude Correction (DAC), or Distance Gain Size (DGS) technique (Standard, 2014b). The aim of these procedures is to evaluate and adjust the precision and accuracy of measurement equipment.

In the comparison of echo amplitudes technique, the test object is tested with a high gain setting, which allows for displaying the smallest detectable flaw. This can be achieved by adjustment of the gain to a predetermined height, e.g. 80% of the screen height for the peak of the reference flaw echo (Berke, 1996).

In the DAC technique, all flaws in the reference block are scanned, their maximum echo amplitudes marked on the display scale and joined by a curve (Berke, 1996). This provides a graphic reference sensitivity level as a function of distance on the A-Scan display.

The DGS technique uses the theoretically derived distance amplitude curves of disk-shaped reflectors to evaluate the echo height of unknown reflectors (Standard, 2014b).

It should be mentioned that, according to the PN-EN ISO 16811:2014 standard, for all these sensitivity setting methods a transfer correction should be applied to compensate for any coupling losses and differences in material attenuation (Standard, 2014b).

The reference blocks offered by suppliers on the market are produced mainly from steels and metal alloys, whereas other materials are available only upon request. The latter situation applies to composite materials, especially due to their great variety.

4.1.4 Post-processing of ultrasonic scans

The last factor described in this section that influences on the measurement uncertainty is post-processing of ultrasonic C-Scans, by which the detected flaw extent is calculated.

A good measure of flaw detectability is the SNR, i.e. the ratio of the amplitude of the flaw echo over the amplitude of background reflections (noise). The SNR is calculated differently in specific cases, for instance, for the purpose of delamination sizing, a so-called 6 dB drop (or 50%) method is commonly applied. The 6 dB drop method, together with other approaches to characterisation and sizing of discontinuities, is defined in the PN-EN ISO 16827:2014 standard (Standard, 2014c). The 6 dB drop method involves locating pixels in a C-Scan, for which the measured response is at least 50% of its maximum value, and then extraction of a boundary of these pixels. However, the accuracy of this method depends on the size and shape of the delamination relative to the ultrasound beam. Moreover, for small defects it may be impossible to obtain the required 6 dB signal drop (Smith *et al.*, 1997). The 6 dB rule tends to underestimate the delamination size, e.g. detect only the strongest damage region while leaving smaller discontinuities around it. Holloway notes (Holloway, 2015) that the 6 dB drop method is best suited for ideal reflectors like drilled holes in reference blocks but tends to fail when applied to real, irregularly shaped discontinuities. Useful findings about defect sizing using the decibel drop methods were elaborated in a research report of Murphy (Murphy, 1987).

As mentioned earlier, in addition to the methods of defect sizing provided in the standards, there is a need of using additional methods to verify the calculated defect extent. A review of found damage detection methods using non-standardized approaches based on image processing and analysis is presented in section 4.2.1.

In the literature, one can find studies focused on a quantitative estimation of the measurement error obtained during damage evaluation with the use of UT. In a study (Heida and Platenkamp, 2011), where the authors tested two different ultrasonic systems

enabling testing with the Phased Array method, the reached accuracy was about 2 mm for defect sizing and 0.2 mm for depth estimation in specimens made of a CFRP composite. It should be mentioned that the defects of diameters in the range of ca. 6–50 mm were considered. The authors rated very well the detectability of flaws such as delamination, disbond and impact damage, whereas small disbonds with the size of 6 mm were qualified as undetectable, or weakly detectable.

The authors of (Broughton *et al.*, 1999), in their experiment on inspecting a PMC using a double-through transmission technique and the 6 dB drop method, concluded that sizes of artificial defects of circular and square shapes were generally overestimated (the highest error was equal to 3.5 mm) and that the uncertainty in defect sizing increased with the defect size decrease. The authors tested simulated delaminations of 6.35, 12.7 and 25 mm in size.

In the paper (Dragan *et al.*, 2012a), fibre metal laminates (FML) were tested using, among others, the Pulse-Echo UT technique with a frequency of 5 MHz, and the air-coupled technique that uses low frequency waves. The ultrasonic scans were processed with the use of an image processing procedure based on the calculated SNR. The results obtained with use of the Pulse-Echo method enabled detection of 70% of all flaws and a relative error was in a range of 2.07–17.08%, whereas with the use of the air-coupled technique – 50% of flaws were detected with the error of 44.76–79.02%.

The problem was also investigated by the authors of (Hasiotis *et al.*, 2011), where CFRP and GFRP composite specimens were tested using the Pulse-Echo technique with a frequency of 5 MHz. In this case, the obtained results were processed using a clustering software. The authors stated that the resulting size of defects were significantly overestimated (from 14% to even 73%) in the case of the CFRP specimens, whereas it was not possible to estimate any size at all in the case of the GFRP specimens. The authors also concluded that testing the GFRP specimens with a lower frequency should give better results.

4.1.5 Summary

The above-mentioned studies demonstrated that there are numerous factors influencing on the measurement uncertainty, thus, flaw size assessment should be performed in an individual way for an undertaken problem and should be verified using a reference block before ultrasonic tests. During industrial inspections, decisive interpretation of ultrasonic scans is performed by a certified expert, who is familiar with the specificity of UT as well as the internal design of the test structure with location of embedded elements,

bolted connections, etc. Adequate knowledge of the test object and its manufacturing history makes it feasible to assess probable nature of detected discontinuity (Standard, 2014c). The qualification of the examining personnel is performed in accordance with the PN-EN ISO 9712:2012 standard (Standard, 2012).

The performed review indicated a lack of comprehensive studies focused on PMC structures that are aimed at the analysis of the measurement uncertainty in flaw sizing based on ultrasonic scans with taking various factors into consideration (including the testing parameters and flaw characteristics). Such an analysis based on CFRP structures, performed within the framework of this thesis, is presented in chapter 5.

4.2 Damage detection using image analysis methods

As previously noted, the C-Scan presentation mode of UT data is used for the purpose of damage sizing. A C-Scan is then treated as an image and processed using methods of image and/or signal processing. In order to calculate the extent of damage observed in the ultrasonic scan it is necessary to firstly separate the pixels representing damage from other pixel regions visible in the C-Scan. Therefore, a very important step in damage evaluation is appropriate processing of the ultrasonic scan in order to extract the damage region properly before calculation of its extent. In order to simplify the damage evaluation procedure the application of image processing methods to the acquired C-Scans is necessary.

4.2.1 A review of related work

Various attempts can be found in the literature that are aimed at the application of image processing methods for aiding or automating the analysis of ultrasonic scans. Starting from one of the first from published works, the authors of (Corneloup *et al.*, 1996) presented a method of B-Scan image segmentation by thresholding using co-occurrence matrix analysis. Kotropoulos *et al.* (Kotropoulos *et al.*, 1994) proposed algorithms based on signal-adaptive filters and self-organizing neural networks for processing of ultrasonic images. The authors of (Bozzi *et al.*, 2007) presented a procedure of detecting porosity in materials used in the aerospace industry employing a 2D wavelet transform, a feature extraction process, a principal component analysis, and decision rules. A method of Momtaz and Sadr (Momtaz and Sadr, 2009) concerning detection and clustering of defects in ultrasound images is based on features extraction using a rosette pattern. Another approach of C-Scan image processing for damage evaluation proposed in (Rashli *et al.*, 2012) is based on extraction and analysis of features specific to analysed damage sites. Several studies on automation of damage detection from C-Scan images were based on the application of the Hough transform (Meksen *et al.*, 2003; Merazi-Meksen *et al.*, 2012a; Merazi-Meksen *et al.*, 2012b), which enables detection of defects of defined geometrical properties. The same group of authors also applied artificial neural networks to distinguish between a noise signal from a defect signal in ultrasonic images (Meksen *et al.*, 2013). Another approach presented in (Li *et al.*, 2013), that is aimed at delamination detection in CFRP panels, is based on fuzzy logic. Other approaches to delamination sizing in composite materials can be found, e.g. a developed Gauss-Hermite beam model presented in (Minachi *et al.*, 1993), or its modification together with other model-based size estimation approaches proposed in (Margetan *et al.*, 2013). Further examples of the application of image processing to ul-

trasonic scans of composite elements are the methods based on data clustering (Samanta and Datta, 2012), or image segmentation based on statistical mean and standard deviation (Li *et al.*, 2012).

Several attempts towards improving the damage evaluation procedure based on ultrasonic scans of aircraft elements were performed by the AFIT specialists. In (Dragan, 2011), Dragan presented an approach to damage detection and identification in C-Scan images based on edge detection and the SNR. In (Dragan *et al.*, 2012b), the authors proposed another method with the use of edge detection algorithm. Stefaniuk and Dragan (Stefaniuk and Dragan, 2016) proposed an algorithm based on image filtering, thresholding and morphological operations. Other preliminary studies (Dragan *et al.*, 2013; Stefaniuk and Dragan, 2014) were related to the application of the extracted damage sites for construction of finite element models in order to predict structural behaviour and residual life of aircraft composite elements after damage occurrence.

As shown, there have been diverse approaches proposed for aiding the damage detecting and evaluating procedures based on ultrasonic C-Scans. However, the approaches found in the literature were adapted to specific tested cases and are not universal. A shortage can be observed that there is so far little work devoted to the development of a universal method suitable for any type of composite structure being tested as well as any damage type and shape. Some methods that succeed in the case of inspection of simple structures, e.g. with a uniform thickness, may fail in the case of testing more complex structures, e.g. with a varying thickness, and vice versa. Moreover, some of the mentioned methods are computationally ineffective when considering the application of image processing algorithms in the on-line mode. Furthermore, no reports were found in the literature on a comparative analysis of detection accuracy of applied image processing methods.

There is a vast number of methods of image processing that might be helpful for the purpose of damage extraction from ultrasonic scans. One of the research objectives is to analyse and compare various types of image segmentation methods in the light of their effectiveness in damage extraction and select the most useful methods. A description of the principles of image segmentation and a review of its methods is presented in section 4.2.2. It should be highlighted that in the case of the use of image segmentation methods in the NDE applications in the aircraft industry, where the precision of damage sizing is of a critical importance, their accuracy must be at a very high level. The study on the effectiveness of image segmentation methods in the area of damage detection is introduced in section 6.

4.2.2 A review of image segmentation methods

In this section, a brief review of image segmentation methods that potentially could be applied in the NDE applications is presented. Image segmentation results in partitioning of an image into fragments (sets of pixels) corresponding to objects visible in the image. Main criteria considered in such procedure can be a colour, intensity or texture. Segmentation algorithms may either be applied to the images as originally recorded, or after the initial processing, e.g. the application of filters. After the segmentation, methods of so-called mathematical morphology can be used to improve the results. Finally, the segmentation results are used to extract quantitative information from the images. The review presented in this section was included in (Wronkiewicz *et al.*, 2018b).

In the literature, there is a large number of surveys on image segmentation methods, from the former general overviews (e.g. introduced in (Fu and Mui, 1981; Haralick and Shapiro, 1985; Shaw and Lohrenz, 1995)) and those focused on threshold-based methods ((Weszka, 1978; Sahoo *et al.*, 1988)) to more recent surveys – from the overall ones (see e.g. (Sonka *et al.*, 2014; De *et al.*, 2016; Kumar *et al.*, 2014; Zaitoun and Aqel, 2015; Zhu *et al.*, 2016)), to those focused on image binarization (Stathis *et al.*, 2008; Chaki *et al.*, 2014), thresholding (Sezgin and Sankur, 2004; Glasbey, 1993), or colour image segmentation (Skarbek and Koschan, 1994).

The mentioned surveys and comparative studies found in the literature are mainly based on object detection from photographs, where problems have a different character than in the case of ultrasonic scans. These are, for instance, the noise content in the photograph or the influence of the uniformity of the illumination. Moreover, many studies are dedicated to problems related to a text/background separation (see e.g. (Stathis *et al.*, 2008; Kefali *et al.*, 2014)) for the optical character recognition (OCR) systems. Surveys of image segmentation found in the area of UT relate mainly to medical applications (e.g. (Noble and Boukerroui, 2006; Saini *et al.*, 2010; Sridevi and Sundaresan, 2013)). In the survey considering segmentation of X-ray and C-Scan images of composite materials performed by Jain and Dubuisson (Jain and Dubuisson, 1992) only four methods, mainly adaptive thresholding, were tested and compared. The authors of (Sezgin and Sankur, 2004) compared more image thresholding methods for the NDT applications. However, there seems to be a lack of comprehensive analyses of image segmentation methods in the context of processing of ultrasonic images in industrial applications, such as diagnostics of composite structures. As mentioned earlier, performing such an analysis is one of the aims undertaken in this research.

Short descriptions of the most common segmentation methods, within the following

categories, are presented below. Considering the introductory character of this section, full descriptions are omitted here, however, a reader can find the details in cited literature.

Threshold-based segmentation

Thresholding is the simplest and one of the most commonly used segmentation methods. The pixels are divided depending on their intensity value. In a basic approach, a threshold value is selected from a grey-scale image and used to separate the foreground of the image from its background. This approach is also called a bi-modal segmentation, since it assumes that the image contains two classes. The threshold can be chosen manually or automatically using one of many methods developed for this purpose, which are described below. Thresholding can be categorized into global, variable, and multiple methods.

Global thresholding. Global thresholding is based on using a single threshold for the entire image. It is performed in such a way that the pixels of the image I which values are higher than a given threshold value T become ones and the lower or equal become zeros. This operation can be expressed by:

$$J_{i,j} = \begin{cases} 1 & \text{for } I_{i,j} > T, \\ 0 & \text{for } I_{i,j} \leq T, \end{cases} \quad (4.3)$$

where i, j denote the coordinates of the image, i.e. the ordinal number of a row and a column, respectively.

Several approaches of automated T selection are listed below.

- Methods based on using a Gaussian-mixture distribution. Otsu's method (Otsu, 1979) aims at finding the optimal value for the global T . It is based on the inter-class variance maximization (or the intraclass variance minimization) between dark and light regions, through the assumption that well thresholded classes have well discriminated intensity values. This method can be also categorised as clustering-based thresholding. Riddler and Calvard (Ridler and Calvard, 1978) proposed an iterative version of the Otsu's method. The authors of (Kittler and Illingworth, 1985) presented a minimum-error-thresholding method based on fitting of the mixture of Gaussian distributions.
- Methods based on an image histogram shape, where, for example, the peaks, valleys and curvatures of the histogram are analysed. One of the examples is an approach proposed by the authors of (Prewitt and Mendelsohn, 1966), where the histogram is smoothed iteratively until it has only two local maxima.

- Methods based on maximizing the entropy of the histogram of grey levels of the resulting classes, e.g. proposed by Pun (Pun, 1980), and modified by Kapur et al. (Kapur *et al.*, 1985) or by Pal N. And Pal S. (Pal and Pal, 1989). A faster, two-stage approach based on entropy was proposed by Chen et al. (Chen *et al.*, 1994).

Variable thresholding. The thresholding methods are called variable when T can change over the image. They can be categorised into local or regional thresholding, when T depends on a neighbourhood of a given pixel coordinates (x, y) , and adaptive thresholding, when T is a function of (x, y) . Examples of the most common algorithms are listed below.

- Niblack's algorithm (Niblack, 1985) calculates a local threshold by sliding a rectangular window over the grey-level image. The computation of the threshold is based on the local mean value and the local standard deviation of all the pixels in the window. This approach is the parent of many local image thresholding methods.
- Sauvola's algorithm (Sauvola and Pietikäinen, 2000) is the modification of the Niblack's algorithm, also based on the local mean and the local standard deviation, but the threshold is computed with the dynamic range of standard deviation.
- Wolf's algorithm (Wolf and Jolion, 2004) addresses a problem in Sauvola's method when the grey level of the background and the foreground are close. The authors proposed to normalize the contrast and the mean grey value of the image before computing the threshold.
- Feng's algorithm (Feng and Tan, 2004) introduced the notion of two local windows, one contained within the other. This method can qualitatively outperform the Sauvola's thresholding, however, many parameters have to be determined empirically, which makes this method reluctantly used.
- Nick's algorithm (Khurshid *et al.*, 2009) derives the thresholding formula from the original Niblack's algorithm. The method was developed for the OCR applications, especially for low quality ancient documents. The major advantage of this method is that it improves binarization for light page images by shifting down the threshold.
- Mean and median thresholding algorithm. The mean-based method calculates the mean value in a local window and if the pixel's intensity is below the mean the pixel is set to black, otherwise the pixel is set to white. In the median-based algorithm the threshold is selected as the median of the local grey-scale distribution.
- Bernsen's algorithm (Bernsen, 1986) is a method using a user-defined contrast threshold. When the local contrast is above or equal to the contrast threshold, the

threshold is set as the mean value of the minimum and maximum values within the local window. When the local contrast is below the contrast threshold, the neighbourhood is set to only one class (an object or background) depending on the mean value.

- Bradley's algorithm (Bradley and Roth, 2007) is an adaptive method, where each pixel is set to black if its value is t percent lower than the average of the surrounding pixels in the local window, otherwise it is set to white.
- Triangle algorithm (Zack *et al.*, 1977) calculates the threshold based on a line constructed between the global maximum of the histogram and a grey level near the end of the histogram. The threshold value is set as the histogram level from which the normal distance to the line is maximal.

Multiple thresholding. The thresholding methods are called multiple, or multi-modal, when more than one T is used. The most common examples are listed below.

- A method of Reddi *et al.* (Reddi *et al.*, 1984) can be considered as an iterative form of Otsu's original method, which is faster and generalized to multi-level thresholding.
- Another extension of the Otsu's method to multi-level thresholding is referred to as the multi Otsu method of Liao *et al.* (Liao *et al.*, 2001).
- A method proposed by Sezan (Sezan, 1990) consists in detection of peaks of the histogram using zero-crossings and image data quantization based on thresholds set between the peaks.

Edge-based segmentation

In an ideal scenario, regions are bounded by closed boundaries and by filling the boundaries we can obtain the regions (objects). This assumption was the foundation to develop the edge-based segmentation methods. They are based on detection of rapid changes (discontinuities) of an intensity value in an image.

The edge detection approaches (see a comparative survey of Bhardwaj and Mittal (Bhardwaj and Mittal, 2012)) use one of two criteria, i.e. they locate the edges when:

- the first derivative of the intensity is greater in magnitude than a given threshold. Using this method, the input image is convolved by a mask to generate a gradient image. The most popular edge detectors (filters) are based on Sobel, Prewitt, and Roberts operators;

- the second derivative of the intensity has a zero crossing. This approach is based on smoothing of the image and extraction of zero crossing points, which indicates the presence of maxima in the image. A popular approach is based on a Laplacian of Gaussian (LoG) operator.

Unfortunately, these procedures rarely produce satisfactory results in the image segmentation problems. Noisy and poorly contrasted images badly affect edge detection, thus producing a closed contour is not a trivial task.

There are also many other methods aimed at finding straight lines and other parametrized shapes in images. The original Hough transform (Hough, 1962) was developed for detection of straight lines. This method was later generalized to the detection of analytically described shapes, such as circles (Duda and Hart, 1972), and to the detection of any shape (Ballard, 1981). These methods, however, are not useful for the problem undertaken in this study, since the general assumption is the baseline-free approach, i.e. damage needed to be detected is of unknown shapes.

Region-based segmentation

The region-based segmentation methods are based on the assumption that pixels in neighbouring regions have similar characteristics, i.e. values of a colour and intensity. The two basic methods are listed below.

- Region growing is a method, in which an initial pixel (a seed) is selected and the region grows by merging the neighbouring pixels of the seed until the similarity criteria (colour, intensity value) are met.
- Region splitting and merging methods. Splitting operation stands for iteratively dividing of an image into homogeneous regions, whereas merging contributes to joining of the adjacent similar regions. There are approaches using one of these operations solely (e.g. a statistical region merging (SRM) algorithm of the authors of (Nock and Nielsen, 2004), a region splitting method of Ohlander et al. (Ohlander *et al.*, 1978)), or both of them.

One should mention a group of region-based methods called watershed-based segmentation. The idea of the watershed transforms comes from geography, i.e. the gradient of image is considered as a topographic map. For instance, in one of such approaches, an image is treated as a map of a landscape or topographic relief flooded by water, where watersheds are the borders of the domains of attraction of rain falling over the region (Roerdink and Meijster, 2000). One of the first algorithms based on the watershed transform was proposed in (Beucher and Lantu  joul, 1979). The application of appropriate

morphological operations after the watershed transform enables obtaining the segmented image.

The main disadvantage of the region-based approaches is that they are computational time- and memory-consuming.

Clustering-based segmentation

Clustering is a multidimensional extension of the concept of thresholding. Clustering is mainly used to divide data into groups of similar objects. Clustering can be classified as either hard or fuzzy depending on whether a pattern data belongs exclusively to a single cluster or several clusters with different membership values. Some clustering methods can readily be applied for image segmentation and the most common of them are described below.

- Hard clustering is a simple clustering technique dividing an image into a set of clusters, which is best applicable to data sets that have a significant difference (sharp boundaries) between groups. The most popular algorithm of hard clustering is a k -means clustering algorithm (Hartigan and Wong, 1979), which simultaneously belongs to unsupervised classification methods. In this method, initial centroids of a given number k of clusters are computed, and each pixel is assigned to the nearest centroid. Then, the centroids of clusters are recomputed by taking the mean of pixel intensity values within each cluster, and the pixels are reassigned. This process is repeated iteratively until the centroids stabilize. In this method, k must be determined, which is its main disadvantage. Moreover, it may lead to different results for each execution, which depends on the computation of initial cluster centroids.
- Soft clustering is applicable to noisy data sets, where the difference between groups is not sharp. An example of such a method is a fuzzy c -means clustering, developed by Dunn (Dunn, 1973) and later improved by Bezdek (Bezdek *et al.*, 1984). The algorithm steps in the fuzzy c -means clustering are very similar to the k -means clustering. The main difference in this method is that pixels are partitioned into clusters based on partial membership, i.e. one pixel can belong to more than one cluster and this degree of belonging is described by membership values.
- A mean shift clustering (appeared first in (Fukunaga and Hostetler, 1975)) is another clustering-based method. It seeks modes or local maxima of density in the feature space. Mean shift defines a window around each data point and calculates the mean of data point. Then, it shifts the centre of the window to the mean and repeats the algorithm step till it converges. This method does not need prior knowledge of

a number of clusters but it needs a mean shift bandwidth parameter.

- Expectation Maximization (EM) algorithm (Dempster *et al.*, 1977) is used to estimate the parameters of the Gaussian Mixture Model (GMM) of an image. The method consists in recursive finding of the means and variances of each Gaussian distribution and finding the best solutions for the means and variances. The EM algorithm can be efficient when analysed data is incomplete, e.g. there are missing data points. However, the method is computationally expensive, and prior knowledge of a number of clusters is needed. Exemplary studies on segmentation using the GMM and EM algorithm are presented in (Fu and Wang, 2012).

There are many other advanced clustering-based segmentation methods, e.g. a Normalized Graph Cut method (Shi and Malik, 2000) based on the Graph Theory. In this approach, each pixel is a vertex in a graph and edges link adjacent pixels. Weights on the edge are assigned according to similarity, colour or grey level, textures, or distance between two corresponding pixels. These methods, however, are time-consuming and determining of many parameters' values is needed.

Other segmentation methods

Some other methods, which can be also used to segment images are briefly mentioned below. In most cases these are very advanced algorithms, but being strongly parameter-dependent makes them non-universal with respect to the problem considered in this research.

- Texture-based segmentation approaches are useful when objects that are needed to be detected have a distinguishable texture. These approaches are often based on making use of texture measures, such as co-occurrence matrices or wavelet transforms. By applying the appropriate filters together with morphological operations, an object of a given texture can be identified in the image.
- Template matching methods (see (Brunelli, 2009) for instance) are used when an object looking exactly like a template is expected to be found in images. In such a method, a template is compared to all regions in the analysed image and if the match between the template and the region is close enough, this region is labelled as the template object.

One should also mention the advanced, soft-computing methods that are also used for the purpose of image segmentation. The most common groups of such methods are shortly introduced below.

- Artificial neural network-based segmentation methods simulate the learning strategies of human brain for the purpose of decision making. A neural network is made of a large number of connected nodes and each connection has a particular weight. A well-known example of neural networks used for data clustering is a Kohonen self-organising map (SOM) (Papamarkos and Atsalakis, 2000).
- Genetic algorithms are randomised search and optimization methods guided by the principles of evolution and natural genetics. A study concerning the application of image segmentation using the genetic algorithms was broadly presented in a book (Bhanu and Lee, 2012). Besides the genetic algorithms, there are many other optimisation approaches that can provide similar results of image segmentation.

4.2.3 Summary

The performed overview presented in section 4.2.2 revealed a number of image segmentation methods that possibly could be applied in the UT applications aimed at improved damage detection. Some of these methods, solely or together with other methods of image processing, were applied for related problems and were discussed in section 4.2.1. However, as mentioned, no studied could be found that would cover a comprehensive analysis and comparison of image segmentation methods in the context of their accuracy in damage detection as well as versatility. A vast majority of surveys and comparative analyses found in the literature concerns mainly the problems of segmentation of photographs and documents. Processing of ultrasonic images is mainly addressed to issues connected with medical imaging. Due to the lack of comprehensive analyses in relation to segmentation of ultrasonic images in industrial applications, the undertaken research presented in section 6 covers the analysis of accuracy of damage extraction in C-Scans of CFRP structures with different levels of complexity.

4.3 3D damage reconstruction and visualisation using image processing

The last part of the accomplished review studies is connected with the enhanced visualisation of damage detected in ultrasonic scans. Since interpretation of ultrasonic scans is sometimes difficult due to the presence of noise or the complexity of the structure geometry and the existence of embedded elements, their 3D visualisation could facilitate the diagnostic inference procedure. A 3D reconstruction of damage, or a defect, based on its 2D representation in a form of a C-Scan or a B-Scan may be helpful for quick assessment of the damage type based on its location, shape and extent at particular depths of the tested element. Typical software dedicated to analysing ultrasonic data do not provide tools enabling such a spatial visualisation, nonetheless, these could be added as an option and provide additional support for the UT operators. This necessity has been noticed by researchers and some studies devoted to this problem can be found, which are presented below.

4.3.1 A review of related work

In the literature, various approaches aimed at 3D damage reconstruction based on ultrasonic data can be found, however, few of them concern the inspection of PMCs. The authors of (Osman *et al.*, 2012) proposed an algorithm based on image segmentation and classification procedure applied to already reconstructed ultrasonic data of a CFRP composite, which allowed for the recognition of defects and their 3D visualisation. Another approach used in the area of composite structures was presented in the study (Li and Chu, 2012), where a 3D view was generated by means of a rule and threshold-based algorithm applied to a ROI in B-Scan data sets. In the study of the authors of (Yeh and Liu, 2009), the surface rendering technique was introduced in order to reconstruct internal defects in concrete structures after the use of a frequency-depth transform and wavelet marginal spectrum as a band-pass filter. Reconstruction of 3D images from raw A-Scans was proposed in (Cornwell and McNab, 1999) with a method based on CAD models of the test specimen geometry and a rule-based expert system with implemented fuzzy logic. Other examples of performing 3D reconstruction of ultrasonic images were proposed for medical applications. For instance, the authors of (Migeon and Marché, 1997) presented a 3D reconstruction of long bones of a newborn, based on image segmentation and contour interpolation method. Further example is a study of Qiu *et al.* (Qiu *et al.*, 2011), introducing a hole-filling algorithm using Distance Weight interpolation applied to the

ultrasound data of chicken kidney.

4.3.2 Summary

The presented studies show a good potential in 3D visualisation of UT data for the NDE purposes. Such a visualisation was found to be helpful in the damage characterisation step, i.e. identification of the type of damage and determination of its size at particular depths of the tested structure. However, it should be taken into account that in the case of the reconstructed C-Scan there is a partial loss of information due to possible covering of the defect that is located exactly below other defect being closer to the surface of the structure. Such a situation, for instance, is typical for impact damage which is characterized by a cascade of multiple delaminations (see Fig. 2.9). More complete image of internal defects distribution can be obtained when reconstructed all B-Scans acquired during inspection. The investigation on effectiveness of 3D reconstruction and visualisation of impact damage in the CFRP structure tested in the research covered by this thesis is presented in section 7. Reconstruction of both C-Scan as well as a series of B-Scans was tested and the obtained 3D geometry was verified based on a reference data acquired with the use of X-ray CT method.

5. Analysis of measurement uncertainty in damage detection and evaluation

The aim of this stage of study was to investigate the measurement uncertainty factors in defect sizing based on the selected type of composite structures with variable configurations of FBHs of known geometric properties. Two UT methods, namely the Pulse-Echo and the Phased Array, and variable testing parameters, such as the frequency and the display mode, were tested. The influencing factors described in section 4.1 were analysed and the measurement errors with respect to the applied composite specimens and considered flaw type were determined and compared. The results presented in this chapter were included in (Wronkiewicz *et al.*, 2018a).

5.1 Structures and experiments

5.1.1 Specimens preparation

The CFRP plates used in this study were purchased from Dexcraft s.c. (Poland), which were manufactured using a resin infusion technology and tailored to specimens with nominal dimensions as follow: $100 \times 100 \times 2.5$ mm (width \times length \times thickness). The components used for the production of these plates were: LG 700 epoxy resin that is dedicated to high-strength laminates, and CC 600 T-120 (twill-weave fabric) with CC 200 P-120 (plain-weave fabric) used for the reinforcement. A percentage composition of the plates is 40% of the resin to 60% of the carbon fabric. Then, FBHs imitating flaws of various diameters (from 2 to 10 mm with a step of 1 mm) with various configurations of their depths were introduced (see a picture of the exemplary specimen in Fig. 5.1). The specimens' depths configurations were as follow: four specimens with the same depths of FBHs of: 0.5, 1.0, 1.5, and 2.0 mm, respectively, and one specimen with mixed depths: from 0.25 to 2.25 with a step of 0.25 mm. The FBHs were introduced with the use of a 3 axis CNC milling machine with positioning accuracy less than 0.01 mm with a VHM type milling cutter.

Narrow dimensional tolerances are difficult to be obtained when machining carbon fibre composites due to their heterogeneity and deviations in surface flatness resulting from the manufacturing process. Because of the obtained deviations from the nominal dimensions of

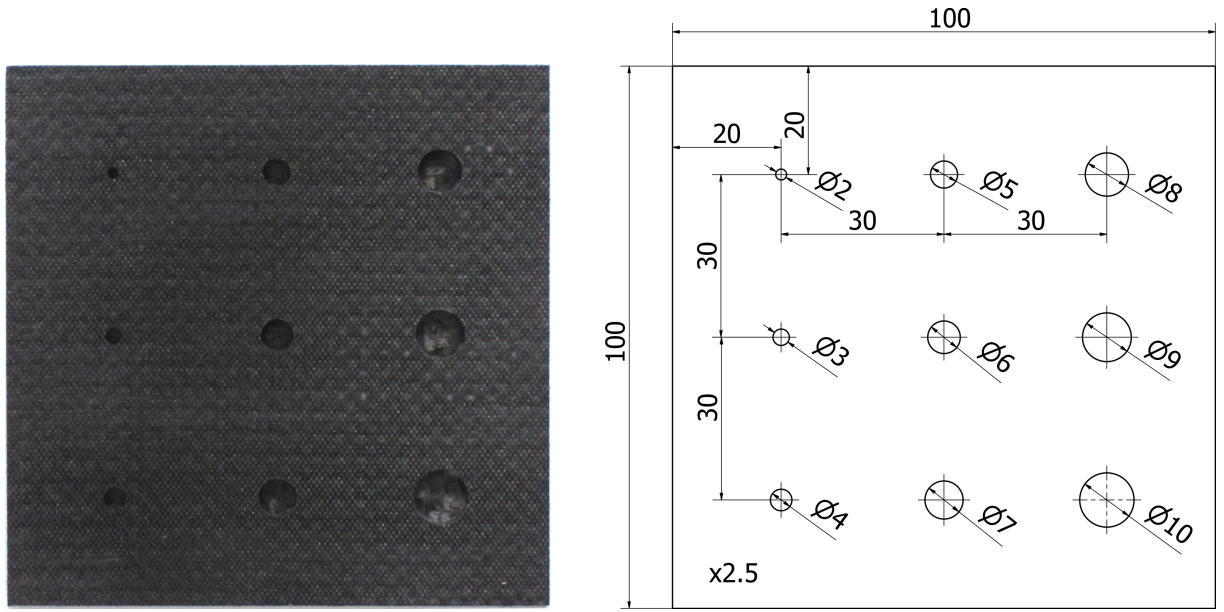


Fig. 5.1: Exemplary specimen and its nominal dimensions (depths configurations are described in the text)

both the specimens' thickness (on average $+0.02$ mm) as well as the diameters of the FBHs (on average $+0.09$ mm) and depths, the finally obtained specimens were measured using a coordinate measuring machine Zeiss C400[®] (see Fig. 5.2) in order to gain knowledge about the exact dimensions. The average deviations of the surface flatness of the specimens as well as the roundness of the FBHs are 0.05 mm.

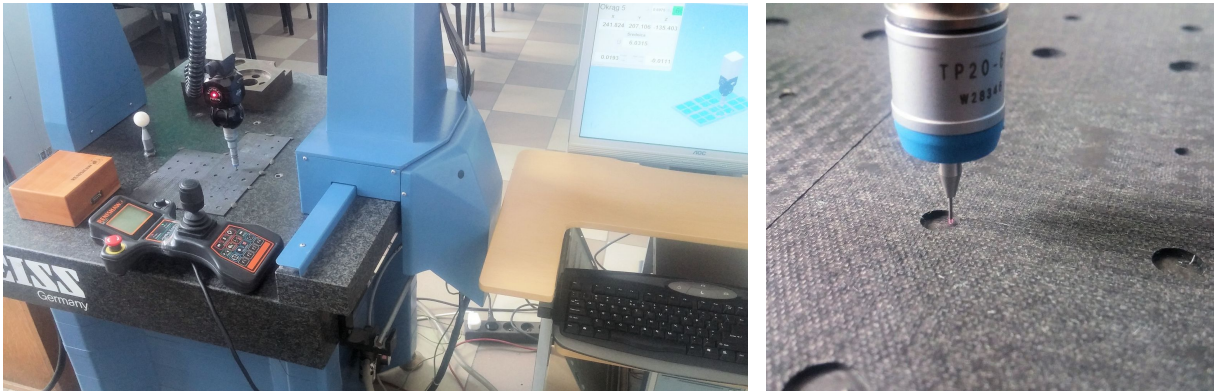


Fig. 5.2: Measurements using the coordinate measuring machine Zeiss C400[®]

The specimens were tested using UT methods from their top side (opposite to milling), i.e. on the smooth surfaces (see Fig. 5.3 on the right). A resulting depth of each FBH was calculated as the difference between the specimen thickness and the depth of the FBH's bottom calculated from the machined side.

5.1.2 UT measurements by the Pulse-Echo method

Firstly, UT of the prepared specimens was performed with the use of the MAUS[®] system (Fig. 5.3). The system enables ultrasonic data (ToF and amplitude peak location) capturing based on selected signal gates. The inspection results can be visualised in a form of C-Scan mapping representing a chosen signal feature, e.g. the amplitude or ToF, with respect to the position of the ultrasonic probe. The signal amplifier enables data generation within the frequency range of 1–20 MHz. For C-Scan mapping, there is a possibility of selecting a single step (X - Y) resolution for either enhancing the image resolution or for fast inspection purposes. The MAUS[®] system enables obtaining an image resolution from 0.01" up to 0.1".

The tests were performed with the use of a single straight-beam probe with a delay line with combinations of parameters: three different central frequencies: 2.25, 5, and 10 MHz, and four different signal rectifier and display modes: peak filtered RF (pfRF) – selection of the highest peak of the signal in the gate; threshold filtered RF (tfRF) – selection from the signal values above the set threshold; threshold RF+ – selection from the positive values of the signal; and threshold RF– – selection from the negative values of the signal. There was also an attempt to test the specimens with a frequency of 15 MHz, however, the noise level was so high that it was too difficult to choose settings of gains and thresholds, thus it was decided to exclude the frequencies higher than 10 MHz. A diameter of the active element of each of the transducers used was 0.25" (6.35 mm) and the scanning resolution was set to the smallest available value of 0.01" (0.254 mm).

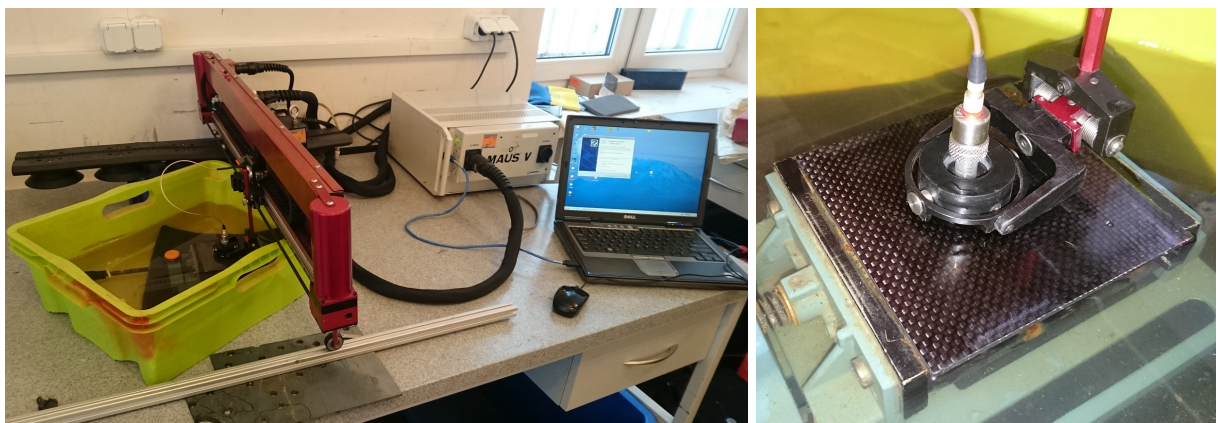


Fig. 5.3: UT with the use of the MAUS[®] automated system

During testing, the appropriate amplitude and depth gains as well as the thresholds for filtering of the ToF signals were set. In order to ensure good coupling between the probe and the test element surface, the specimens were shallowly immersed in water. The

results of the tests were the generated amplitude and ToF representations of C-Scans. The ToF C-Scans were used for calculation of the FBHs' diameters since they are more suitable for the processing purposes in comparison with the amplitude C-Scans that are not filtered and have a lot of noise. In turn, since the amplitude data is not filtered, it gives more reliable information about defect outline and location, which can be used as the reference data in order to verify the shape of the detected defect visible in the ToF C-Scan. Differences in the outlines of the detected defect visible in the ToF and the amplitude C-Scan may indicate incorrectly set gains or filtering thresholds, thus, these two types of C-Scans (see example in Fig. 5.4) were compared and analysed during the tests. More exemplary C-Scans and the results of the calculations of the FBHs' diameters are presented and discussed in the next sections.

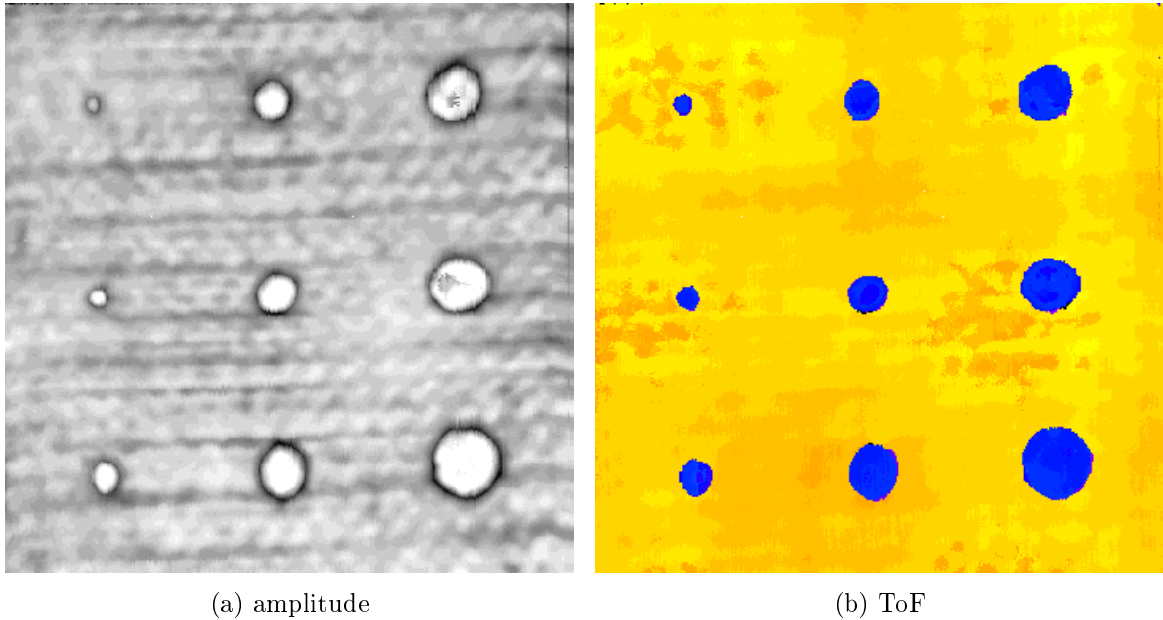


Fig. 5.4: Exemplary pair of ultrasonic C-Scans

5.1.3 UT measurements by the Phased Array method

The second UT method used in this study was the Phased Array testing, performed with the use of FlawInspecta[®] scanner (Fig. 5.5). The signal amplifier enables data generation within the frequency range of 1–15 MHz with a Phased Array transducer containing 128 single active elements (straight-beam probes). For the purpose of the inspection a frequency of 5 MHz and the RF data capturing were used. The scanning resolution was 0.02" (0.508 mm per pixel) and the RF signal was filtered by the highest peak in the gate. These testing parameters were selected as being close to one of the two most accurate sets

of parameters used for testing with the Pulse-Echo method (5 MHz, pRF). The coupling was achieved by applying a small amount of water on the specimens' surfaces.

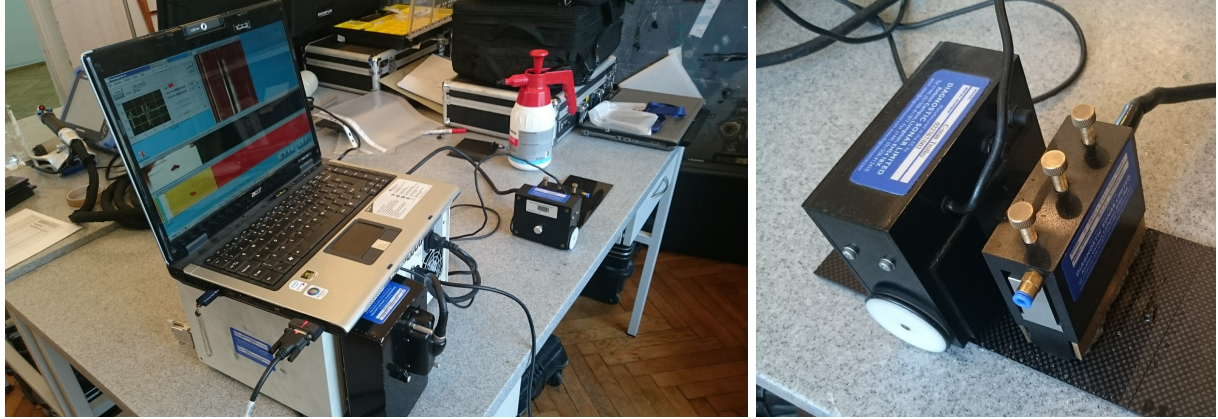


Fig. 5.5: UT with the use of the FlawInspecta[®] scanner

5.2 Image analysis algorithm

The obtained ToF C-Scans were processed using an algorithm as follows. Firstly, an input C-Scan is loaded as an RGB image (see the example in Fig. 5.6(a)), which is later converted into a grey-scale image. The next step is the global image thresholding using one or more selected thresholds, depending on the C-Scan being processed, by which most of noise (i.e. the background reflections) is removed from the image. Afterwards, morphological operations such as morphological opening and flood-fill operation are applied in order to clean very small regions of pixels remaining from the noise and fill missing pixels of FBHs, respectively. All the connected objects (ROIs) in the resulting binary image are then labelled with subsequent indices (see Fig. 5.6(b)) in order to extract their boundaries and calculate their equivalent diameter, i.e. a diameter of a circle with the same area as the region (Fig. 5.6(c-d)). The diameter displayed on the resulting figures is previously converted from the pixel to the millimetre unit using the known scanning resolution. In order to determine the calculated depth of each FBH, the most frequent value occurring within the boundary of the FBH's region is selected as the estimated depth.

It should be highlighted that it was not the aim of this stage of study to evaluate the image analysis algorithm (that stage is presented in chapter 6). The displayed contours on the input C-Scans allowed for visual assessment of the correctness of the obtained ROIs and correction of the selected values of the algorithm's parameters if needed.

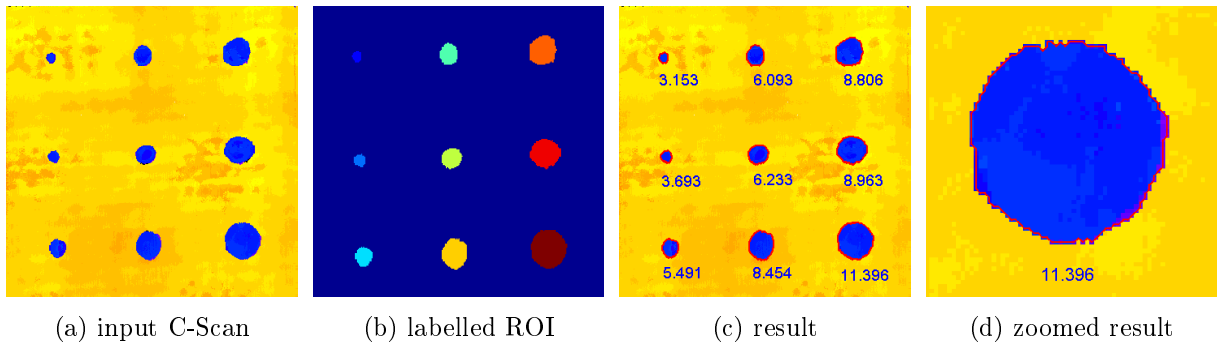


Fig. 5.6: Selected steps of the image analysis algorithm

5.3 Results and discussion

5.3.1 Results from the Pulse-Echo UT

Selected ToF C-Scans obtained for different configurations of the operating parameters are presented in Figs. 5.7, 5.8, 5.9, for the specimens with the FBHs located at depths of 0.5 mm, mixed, and 2.0 mm, respectively.

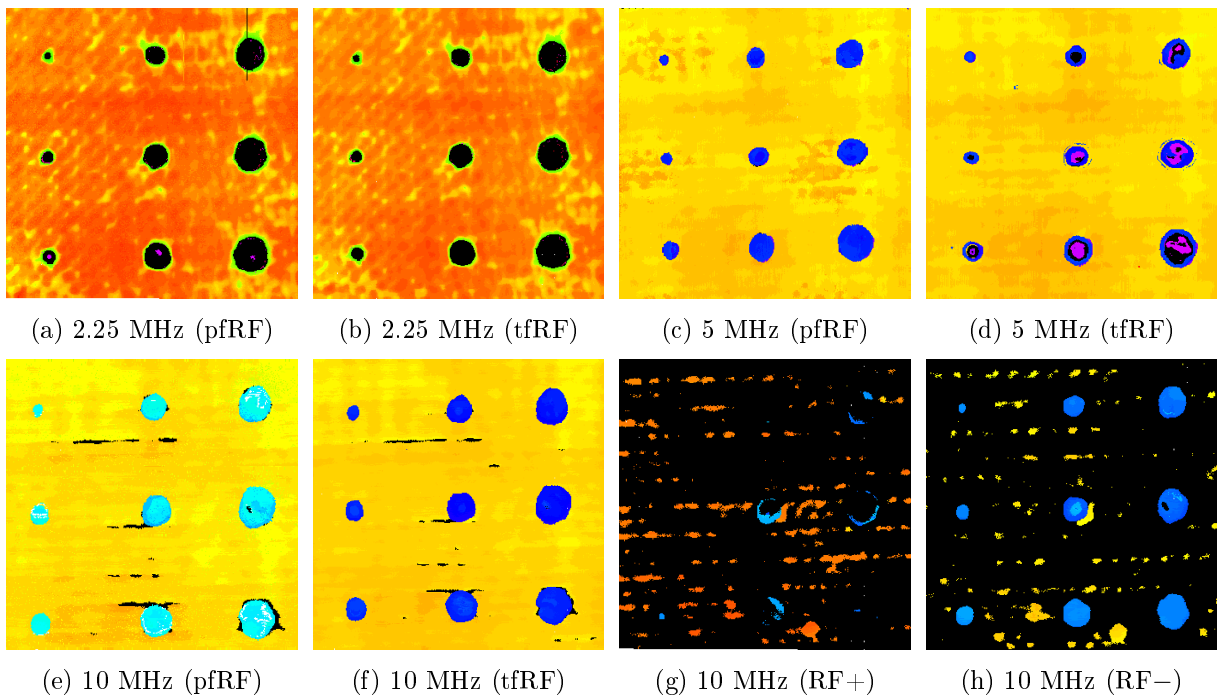


Fig. 5.7: ToF C-Scans obtained using the Pulse-Echo UT method for the specimen with FBHs at a depth of 0.5 mm

From visual analysis of the C-Scans obtained for the specimen with the FBHs at a depth of 0.5 mm (Fig. 5.7) and mixed depths (Fig. 5.8) it can be concluded that the

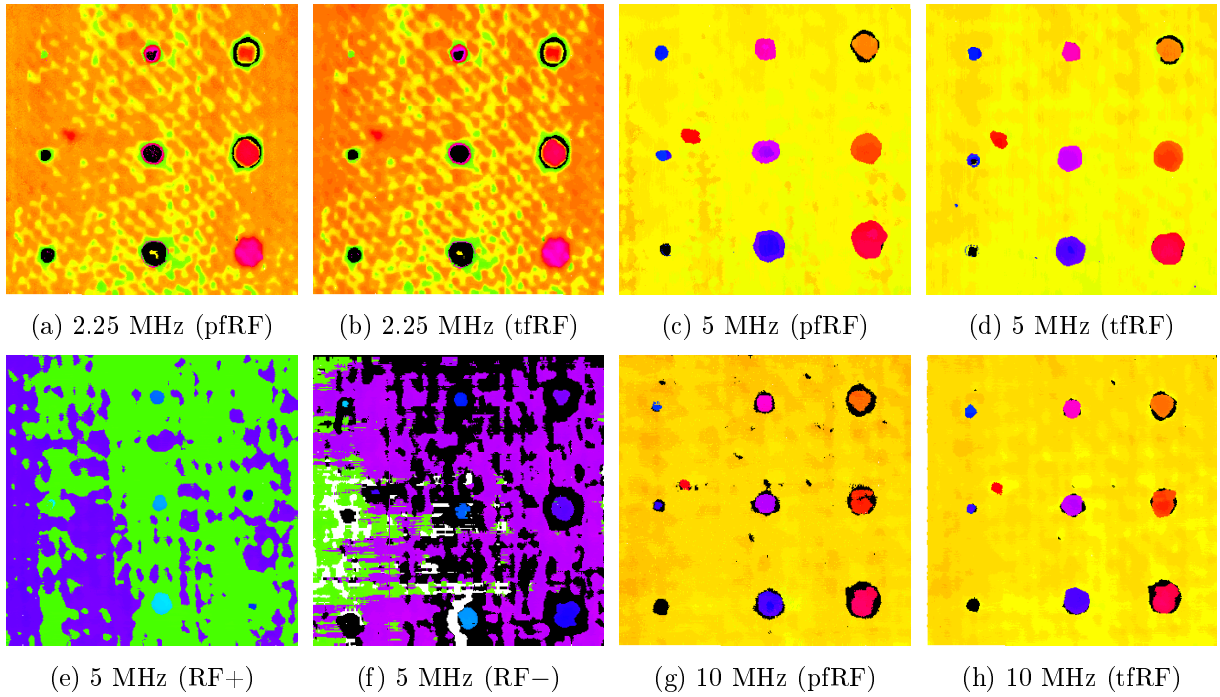


Fig. 5.8: ToF C-Scans obtained using the Pulse-Echo UT method for the specimen with FBHs at mixed depths

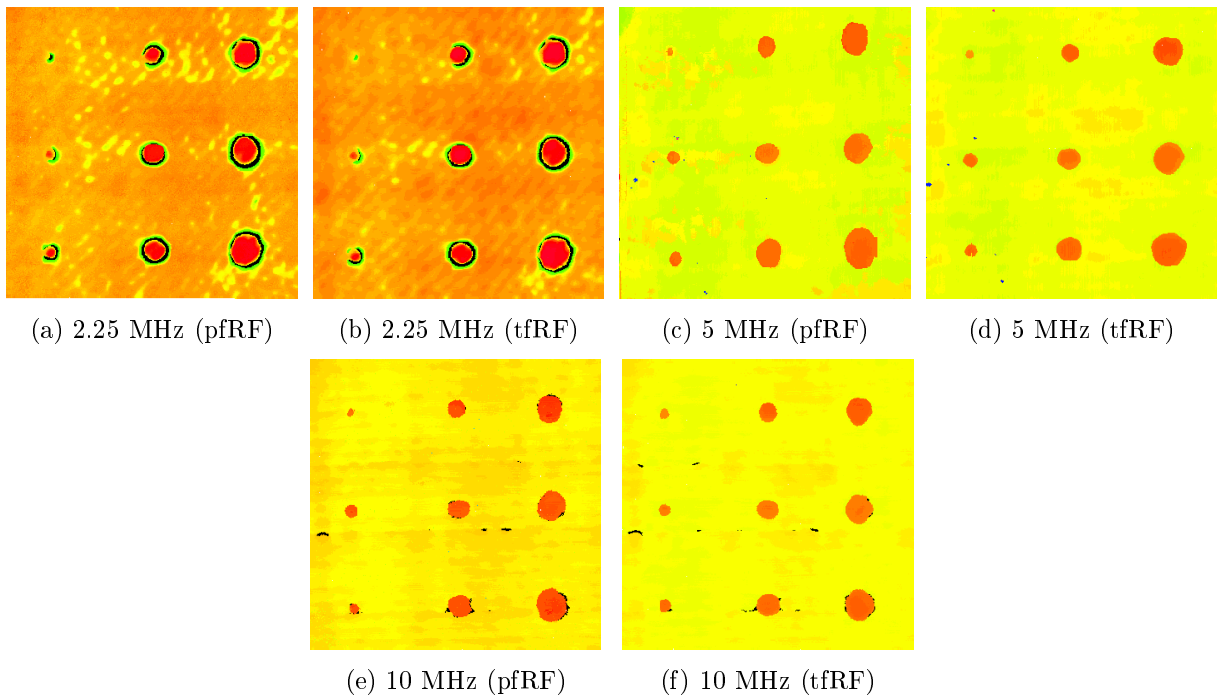


Fig. 5.9: ToF C-Scans obtained using the Pulse-Echo UT method for the specimen with FBHs at a depth of 2 mm

RF+ and RF− display modes are not appropriate for the defect sizing purposes since many FBHs were detected improperly or not detected at all. Moreover, in the C-Scans displayed with these modes there is a significant lack of signal values (the black pixel regions are the measurement points where the signal values were e.g. beyond the set thresholds or within the ultrasonic transducer dead zone), thus these modes were excluded from testing of the rest specimens. The difference between the quality of C-Scans obtained with the pfRF and tfRF display modes is, in most cases, insignificantly noticeable. By observation regarding the frequency it can be noticed that frequencies of 5 MHz and 10 MHz seem to be more suitable since in the case of 2.25 MHz – values of signals reflected from significant parts of FBHs were not measured (the black pixel regions), which causes a lack of information about the defects' depths.

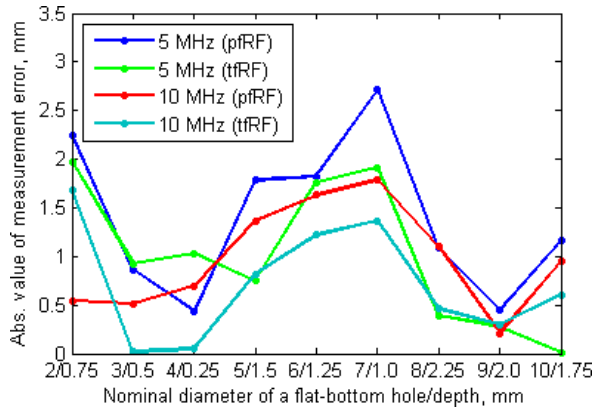
Statistics of the calculated measurement error of the FBHs' diameters from ToF C-Scans obtained using various parameters of the Pulse-Echo UT method is presented in Fig. 5.10. Fig. 5.10(a,c,e,g,i) presents absolute values of the measurement errors (in mm) with respect to the FBHs' parameters (i.e. their nominal diameter and depth location) obtained using different UT operating parameters. For each calculated FBH diameter using different UT operating parameters, the presented boxes in Fig. 5.10(b,d,f,h,j) denote as follow: the central marks denote median values, boundaries of the boxes represent 25th and 75th percentiles, whiskers reflect extreme data points, and red signs + are the singular data points beyond the whiskers.

From analysis of the results presented in Fig. 5.10 one can notice that:

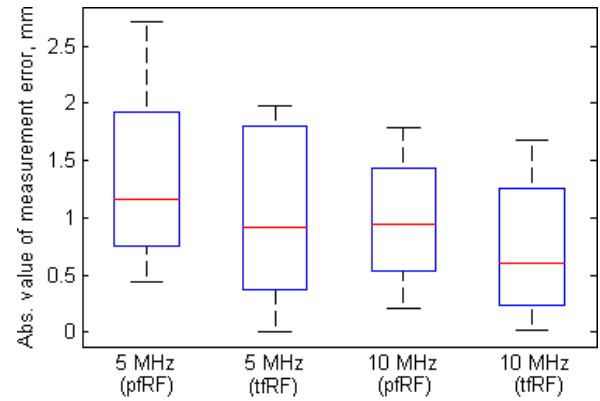
- the measurement error for the FBHs located at the 0.5 mm depth was the smallest (below 1.2 mm) when tested with the frequency of 2.25 MHz, however, taking into consideration that the diameters of the regions representing the lack of signal values (the black regions visible in Fig. 5.7(a–b)) were calculated, this frequency is not recommended for testing the specimens used in this study, as it was mentioned before. The measurement error calculated for the RF− mode was also relatively low (below 1.3 mm), however, testing with the RF+ and RF− display modes were also excluded based on the visual analysis of the obtained C-Scans. The results obtained in the RF+ mode did not allow for calculations of the diameters at all. Therefore, for this specimen, optimal results were obtained with the use of 5 MHz frequency (the error for pfRF is below 1.5 mm, for tfRF – below 2.2 mm) and a little worse with the use of 10 MHz (the error for pfRF – below 2.5 mm, tfRF – below 2.9 mm).
- the measurement error for the FBHs located at the 1.0 mm as well as the 1.5 mm depths was the lowest in the case of testing with the frequency of 10 MHz and the pfRF capturing mode. The error is below 1.8 mm in the case of a depth of 1.0 mm,

and below 1.3 mm in the case of a depth of 1.5 mm.

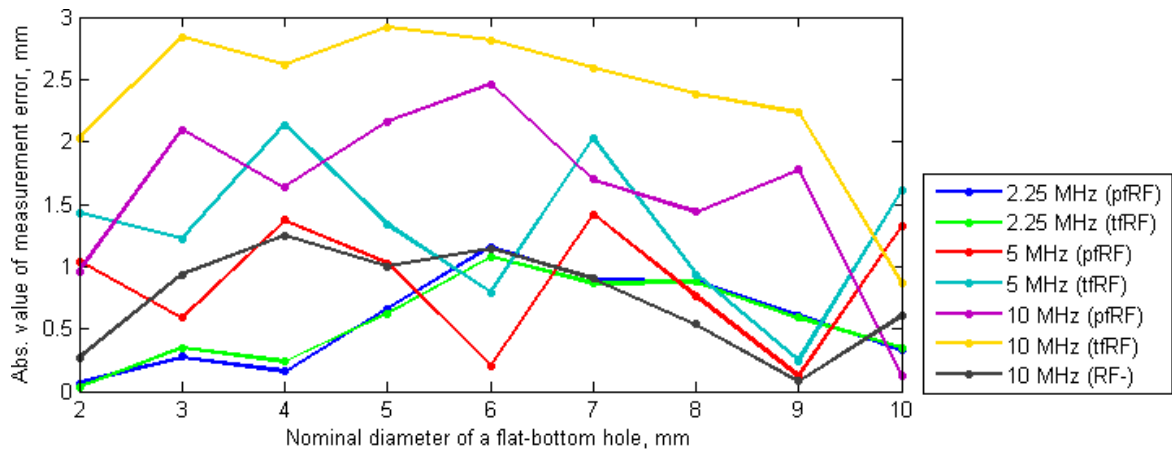
- for the FBHs located the deepest – at the 2.0 mm, the lowest maximum measurement error (below 0.9 mm) was observed when tested with the frequency of 5 MHz and again the pfRF mode.
- in the case of the specimen with mixed FBHs' depths, no dependency was observed



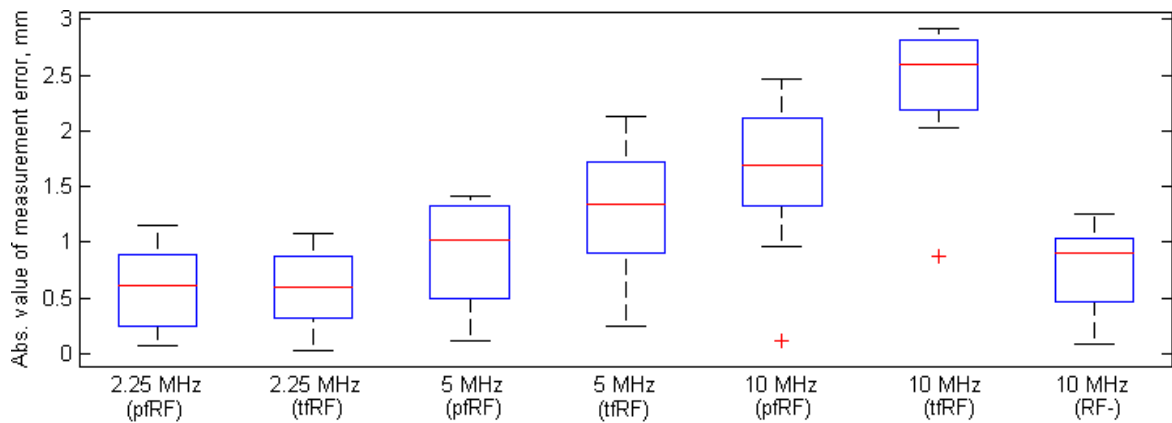
(a) mixed depths



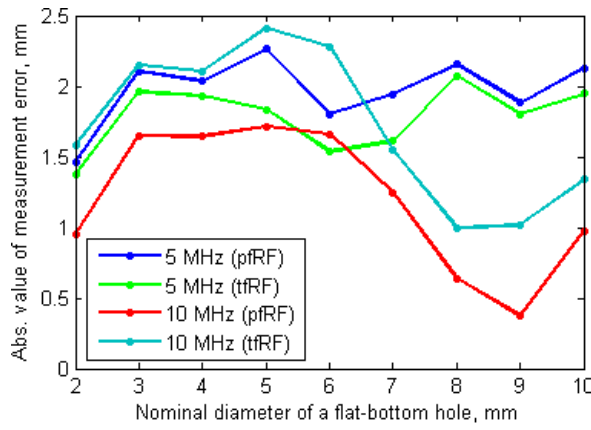
(b) mixed depths



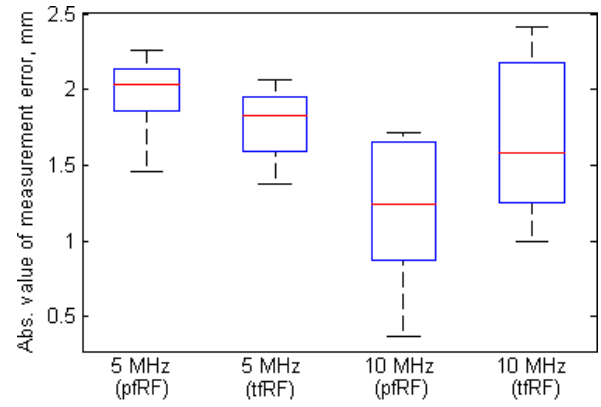
(c) a depth of 0.5 mm



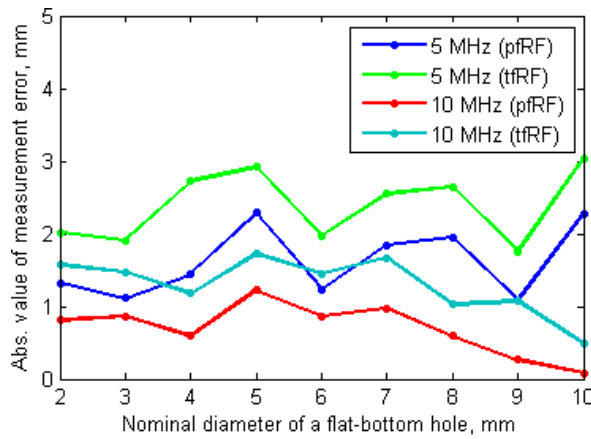
(d) a depth of 0.5 mm



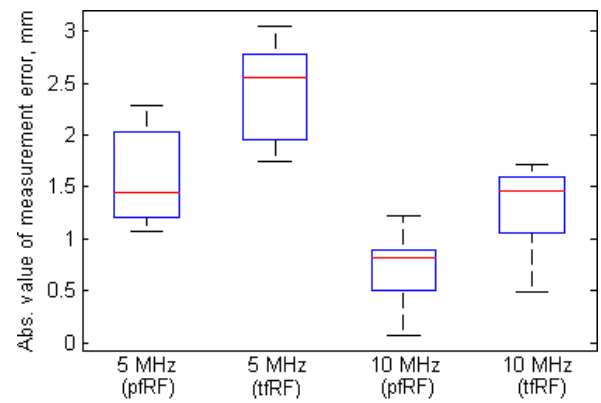
(e) a depth of 1.0 mm



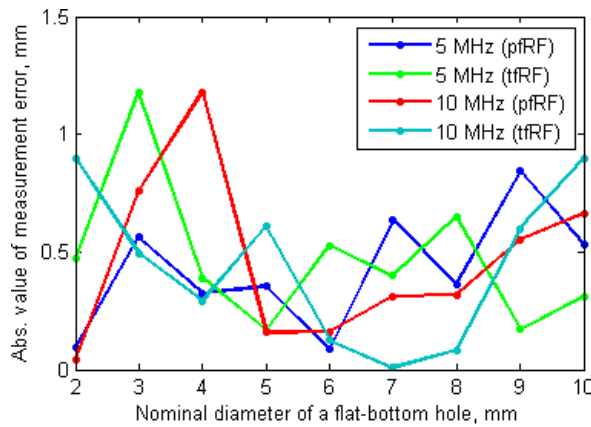
(f) a depth of 1.0 mm



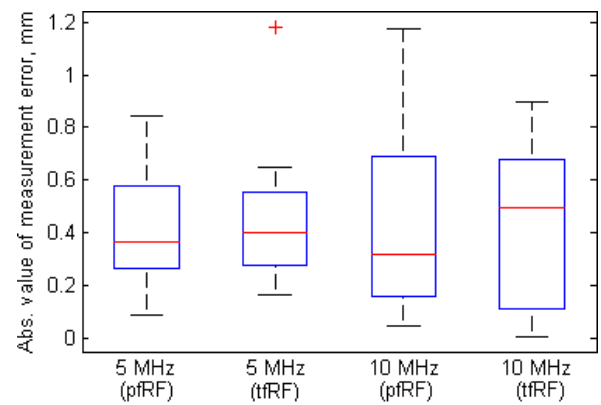
(g) a depth of 1.5 mm



(h) a depth of 1.5 mm



(i) a depth of 2.0 mm



(j) a depth of 2.0 mm

Fig. 5.10: Measurement diameter error statistics for ToF C-Scans obtained using the Pulse-Echo UT method

concerning the measurement accuracy with respect to the FBHs' diameter or depth. There are several cases where the frequency of 10 MHz brought more accurate results, and the same applies for 5 MHz.

The FBHs' diameters were not calculated for the rest results obtained with the frequency of 2.25 MHz, since it was difficult to decide which regions should be considered as the ROI (see e.g. Figs. 5.8(a–b), 5.9(a–b)), thus, the image processing steps could significantly affect the calculation accuracy.

The presented measurement errors (given as their absolute values) in most cases relate to over-sizing of the FBHs, i.e. only in several cases the calculated diameters were smaller than the actual ones.

In general, one can conclude that for the CFRP specimens tested with the Pulse-Echo UT method the most suitable parameters for defects' diameters assessment is the frequency of 5 MHz and 10 MHz and in most cases the pRF display mode brought the most accurate results. No clear dependency could be observed concerning the measurement error in relation to the testing frequency and the diameter or depth of the FBHs, which may be due to the applied delay line that improves the near-surface resolution.

The measurement errors concerning the calculated depths of the FBHs obtained for the different operating parameters are presented in Fig. 5.11. In these results one can notice that the best accuracy in depth estimation was obtained when tested with the frequency of 10 MHz, especially with the pRF mode (the measurement error was mostly below 0.08 mm). This proves that applying higher frequencies allows obtaining thickness location precision, which was described in section 4.1.2. In the case of the specimen with mixed depths, the FBH located at a depth of 0.25 mm (the black one in the left-bottom corner in Fig. 5.8) could not be determined at all, which is caused by location of this FBH within the ultrasonic transducer dead zone. It can be also noticed that there is an exceptional case for one of the FBH (located at a depth of 0.5 mm), which was located with the lowest accuracy when tested with the frequency of 10 MHz, where the error is little over 0.5 mm (see Fig. 5.11(e)).

5.3.2 Results from the Phased Array UT

The ToF C-Scans obtained for the tests performed with the use of the Phased Array UT are presented in Fig. 5.12. In these results one can see that the FBH of a 2 mm diameter was not detected in all cases and the FBH of a 3 mm was detected only in the specimen where the FBHs are in the deepest location (at a depth of 2 mm).

Statistics of the calculated measurement error of the FBHs' diameters from ToF C-Scans obtained using the Phased Array UT method is presented in Fig. 5.13. The mean value of these measurement errors for all the obtained diameters equals 1.7 mm, among which the lowest error equals 0.17 mm and the highest equals 3.77 mm. One can also

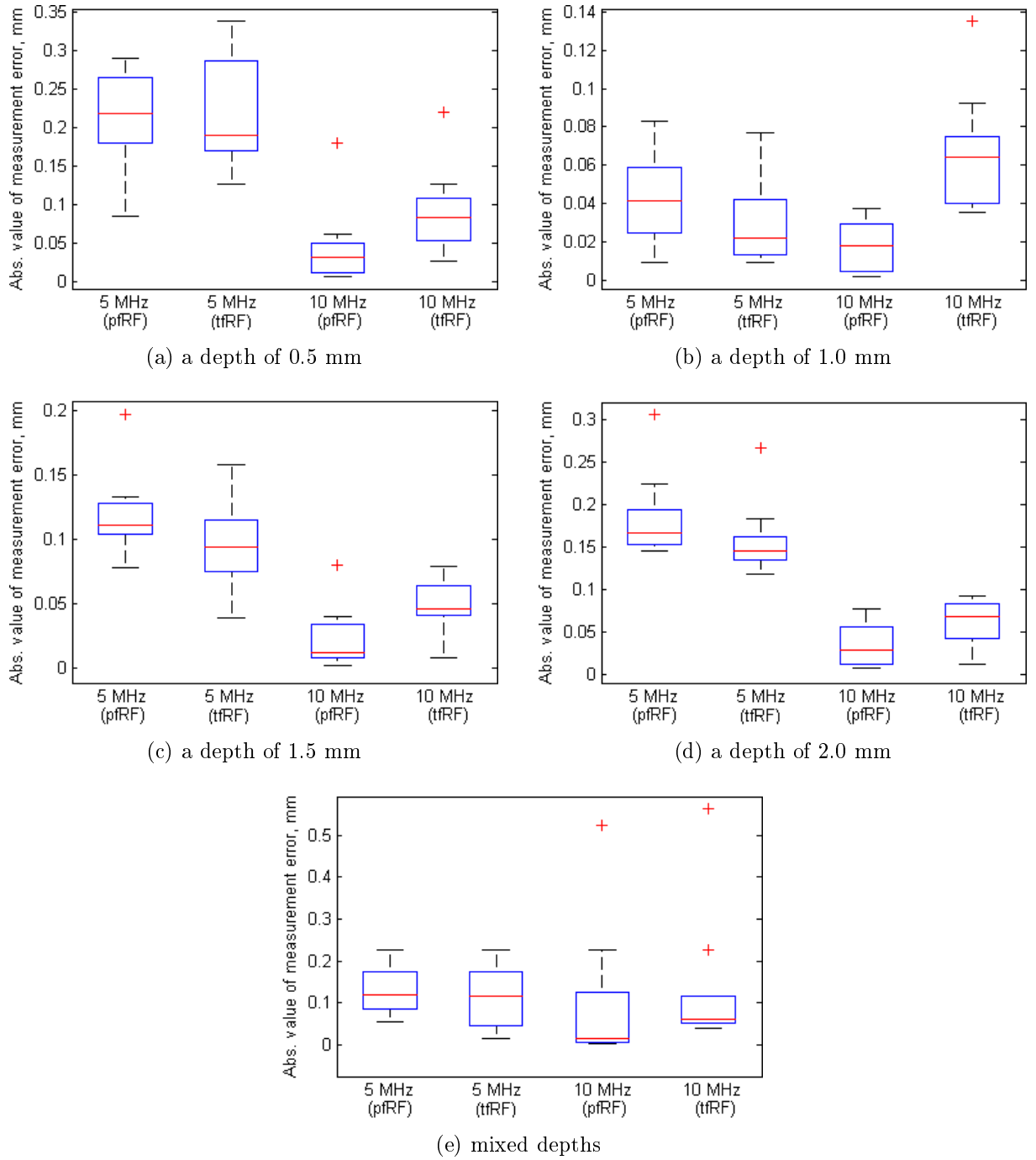


Fig. 5.11: Measurement depth error statistics for ToF C-Scans obtained using the Pulse-Echo UT method

observe a slightly increasing trend of the measurement error together with the increase of a diameter of the FBHs. This can be explained by the fact that the FBHs diameters are close to the size of the ultrasonic probe.

When compared the results obtained using the Pulse-Echo and the Phased Array

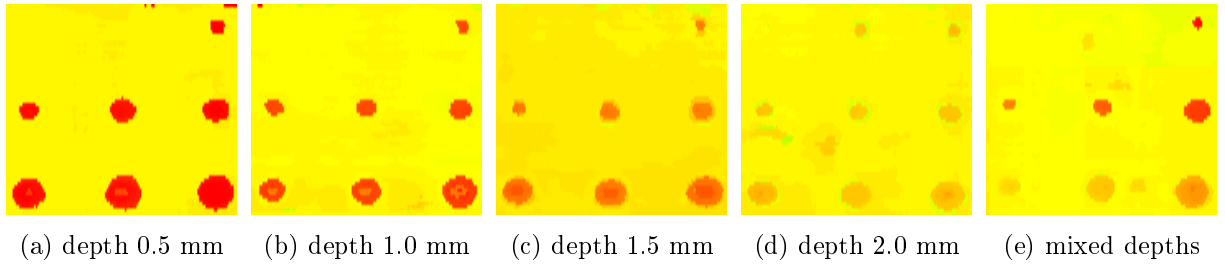


Fig. 5.12: ToF C-Scans obtained using the Phased Array UT method

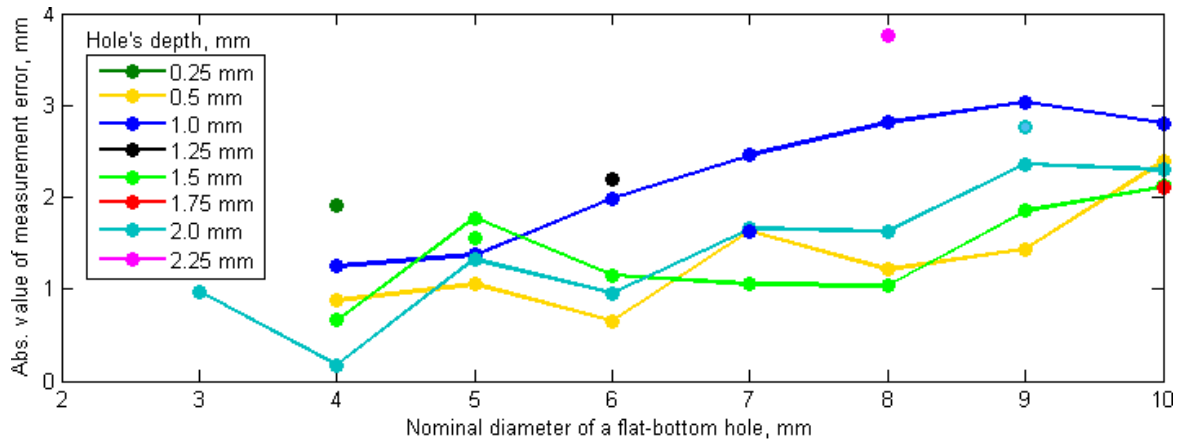


Fig. 5.13: Measurement diameter error statistics for ToF C-Scans obtained using the Phased Array UT method

methods, both with a frequency of 5 MHz and the pRF display mode, it can be noticed that the obtained mean measurement error is similar for both methods, however, when analysed all the obtained diameters, the error is in most cases lower when used the Pulse-Echo method except the FBHs located at a depth of 1.5 mm, where the error obtained with the use of the Phased Array method is lower for all the diameters. Moreover, opposite to the results obtained with the Pulse-Echo method, the presented measurement errors (given as their absolute values) obtained with the Phased Array method relate in most cases to under-sizing of the FBHs, i.e. only in two cases the calculated diameters were bigger than the actual ones.

5.4 Conclusions

In this chapter, the investigation was presented that covers the factors influencing on the measurement errors in flaw sizing based on UT of composite structures. It should be highlighted that this investigation was limited to the selected type of composite structures examined in this research studies and the selected type of defects, namely the CFRP

specimens with a variety of FBHs. Two UT methods, i.e. Pulse-Echo and Phased Array, were applied with variable testing parameters, such as the frequency and the display mode. The obtained results for the tested CFRP specimens of a 2.5 mm thickness indicated the essential observations as below.

- The highest measurement accuracy was obtained when tested with the frequencies of 5 MHz as well as 10 MHz and with a single straight-beam probe (Pulse-Echo technique) with a delay line and using the pRF display mode. Lower and higher frequency values as well as other display modes returned higher measurement errors and/or problems with the defects detection.
- Testing with the Phased Array method returned slightly higher errors when compared to the Pulse-Echo analogously with a frequency of 5 MHz and pRF display mode (except the FBHs located at a depth of 1.5 mm), however, the smallest FBHs were not detected at all.
- For the Pulse-Echo testing most diameters were over-sized whereas for the Phased Array testing they were mostly under-sized.

These observations allowed for the selection of the most suitable operating parameters for further experiments. Taking the obtained findings into consideration it was decided that the CFRP specimens used in further studies will be tested with a frequency of 5 MHz and the pRF display mode as the optimal parameters. It should be kept in mind that the evaluated sizes of damage sites considered in further studies might be over-sized or under-sized depending on the selected testing technique.

6. Analysis of damage detection accuracy using image segmentation methods

This chapter presents a comparative analysis of various image segmentation methods in the light of accuracy of damage detection in ultrasonic C-Scans of composite materials. The selected methods, namely the threshold-, edge-, region-, and clustering-based ones, were tested using ultrasonic C-Scans of an impacted composite specimen and an aircraft panel with delamination. A problem with selection of appropriate input parameters using most of the segmentation methods is discussed and non-parametric histogram-based approaches are proposed. A quantitative analysis of accuracy of damage detection using the segmentation methods is presented and the most suitable approaches are introduced. The results presented in this chapter were included in (Wronkiewicz *et al.*, 2018b).

6.1 Structures and experiments

The comparative analysis of image segmentation methods was performed based on ultrasonic C-Scans acquired during testing of two elements made of composite structures.

The first tested element is a specimen (see its fragment in Fig. 6.1(a)) made of a CFRP composite with an impact damage of a BVID type. As it can be noticed, there are only barely visible marks of the impact damage on the specimen's surface in the middle of the photograph. This specimen was prepared using a CFRP plate taken from the same manufacturing series of plates as those used in chapter 5 and described in section 5.1.1. The BVID was introduced artificially using a test rig for the drop weight impact tests, which is presented in section 8.1 and described in detail in (Katunin, 2015c; Katunin, 2015b). The specimen was impacted with the energy of 20 J using a so-called blunt impactor (with a rounded ending; see the impactor E presented in Fig. 8.1(c)).

The second element is a composite panel used in military aircrafts with delamination formed during maintenance. As an exemplary structure, a part made of CFRP KMU-4e: ELUR-0.1p and ENFB based on epoxy resin was chosen. The laminates were manufactured

with layers of the stacking sequence: 0,90,-45,+45. The thickness of the inspected panel is equal to 4 mm. A demonstrative fragment of the tested element is presented in Fig. 6.1(b). In the tested panel, the delaminated areas developed around a hatch of an elliptic shape as well as in the area of rivet holes. This more complicated structure was intentionally chosen for this study since the analysis aims at selecting universal segmentation methods that are suitable for both simple and more difficult tested cases.

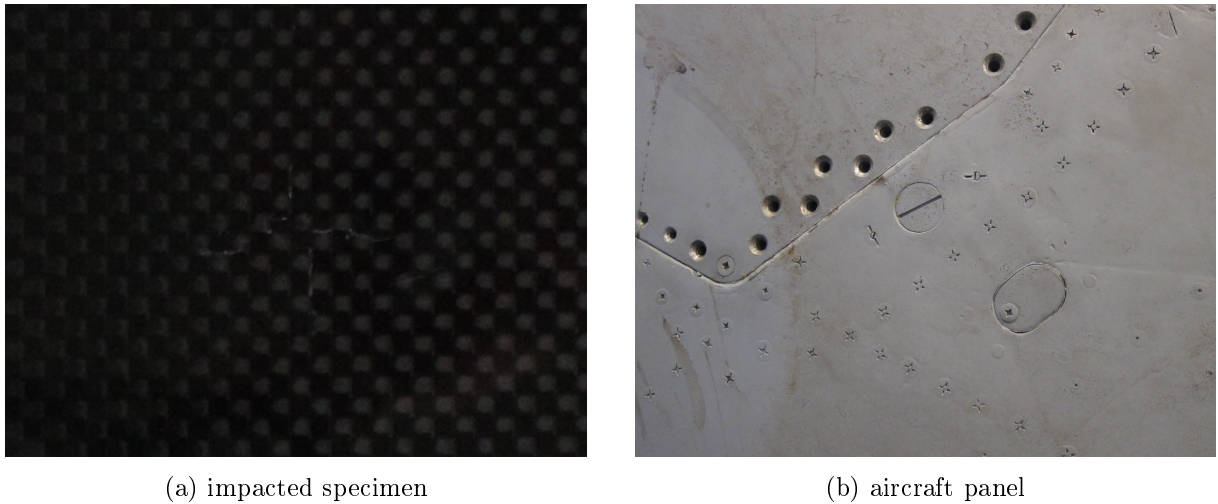


Fig. 6.1: Tested elements made of CFRP composites

Both elements were tested using the MAUS[®] system with a 5 MHz single transducer and a resolution of 0.01". The obtained ToF C-Scans of the impacted specimen and the aircraft panel are presented in Fig. 6.2(a,c). The ground-truth binary images of these C-Scans are presented in Fig. 6.2(b,d), where the thresholds were carefully selected manually to extract all potential damage regions. These ground-truth images are the reference data, to which the results obtained in this study will be compared.

6.2 Comparative analysis of image segmentation algorithms

In order to consider a segmentation method as a candidate for the analysis of ultrasonic C-Scans during inspections of composite materials, the method should not require setting of many input parameters, thus it should be universal and fast. Based on the performed review of image segmentation methods (see section 4.2.2) and taking into consideration their advantages, disadvantages and limitations, appropriate methods were selected for the comparative analysis.

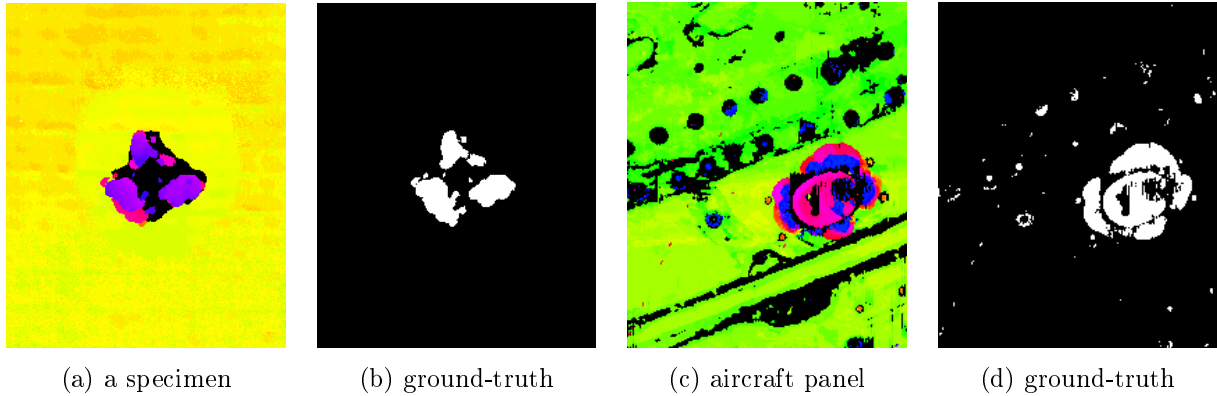


Fig. 6.2: C-Scans of the tested elements (a,c) and corresponding binary images (b,d)

Two main criteria should be taken into consideration when analysing accuracy of damage detection in ultrasonic C-Scans: a segmentation accuracy, and a number of the resulting classes (segments). The accuracy was calculated as a correlation between the resulting binary image and the reference ground-truth image, given in the range of 0–1. The resulting number of classes obtained as a result of image segmentation is also very important since, for instance, obtaining high accuracy but through detection of a large number of little segments that perfectly cover the area of the ground truth object is not desirable.

6.2.1 Analysis of bi-modal threshold-based segmentation methods

Firstly, the threshold-based bi-modal segmentation methods were tested, namely the Bernsen's, Bradley's, Feng's, Niblack's, Nick's, Otsu's, Sauvola's, Triangle, Wolf's, as well as the Mean and Median thresholding algorithms. The exemplary results obtained with selected values of the algorithms' parameters are presented in Fig. 6.3 and Fig. 6.4, respectively, for the C-Scan of the impacted specimen and the aircraft panel.

From these results one can notice that bi-modal segmentation did not bring the expected results in any case. It can be observed that such approaches are not appropriate for the UT applications, since C-Scans should not be respected as having only two classes, i.e. the damaged and undamaged regions. It is especially visible in the case of the aircraft panel that beyond damage and the healthy structure there are also other regions, such as stiffeners, rivet holes, or just noise, which should be segmented separately. This fact entirely eliminates the bi-modal segmentation methods from further considerations.

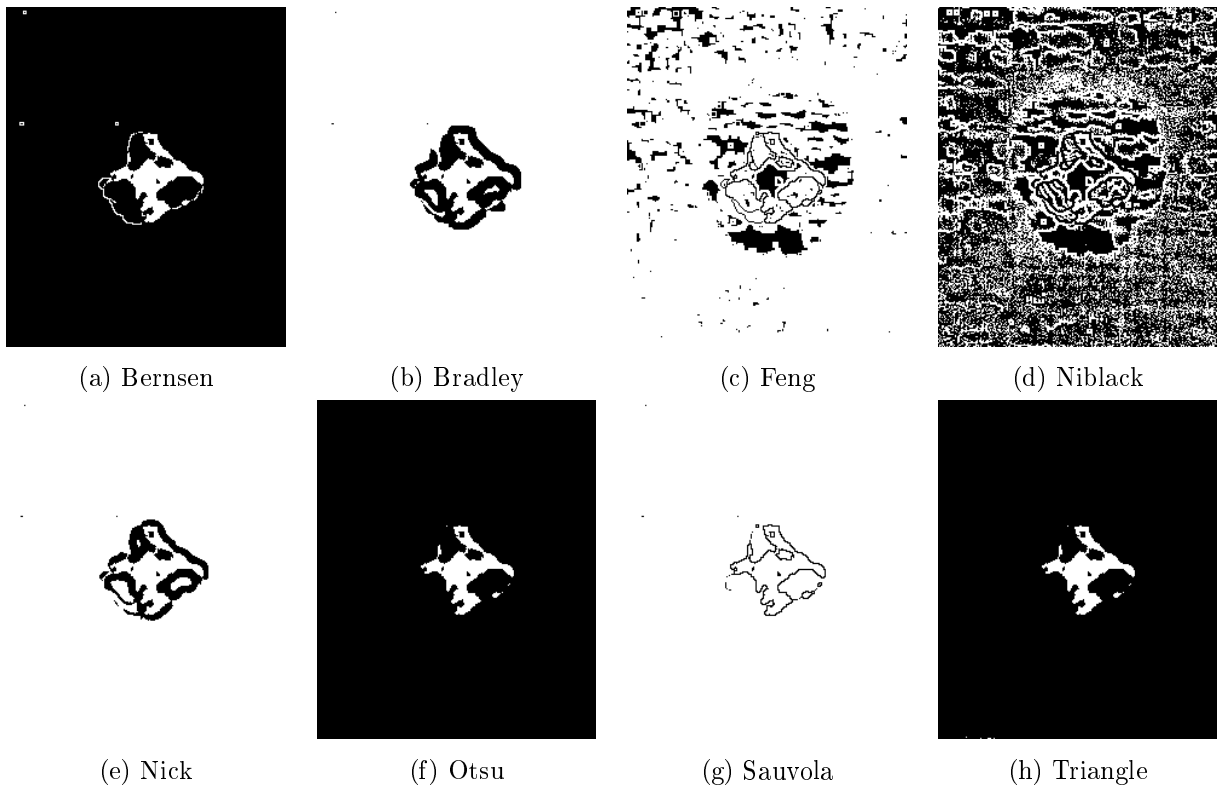


Fig. 6.3: Exemplary results of image thresholding (C-Scan of the impacted specimen)

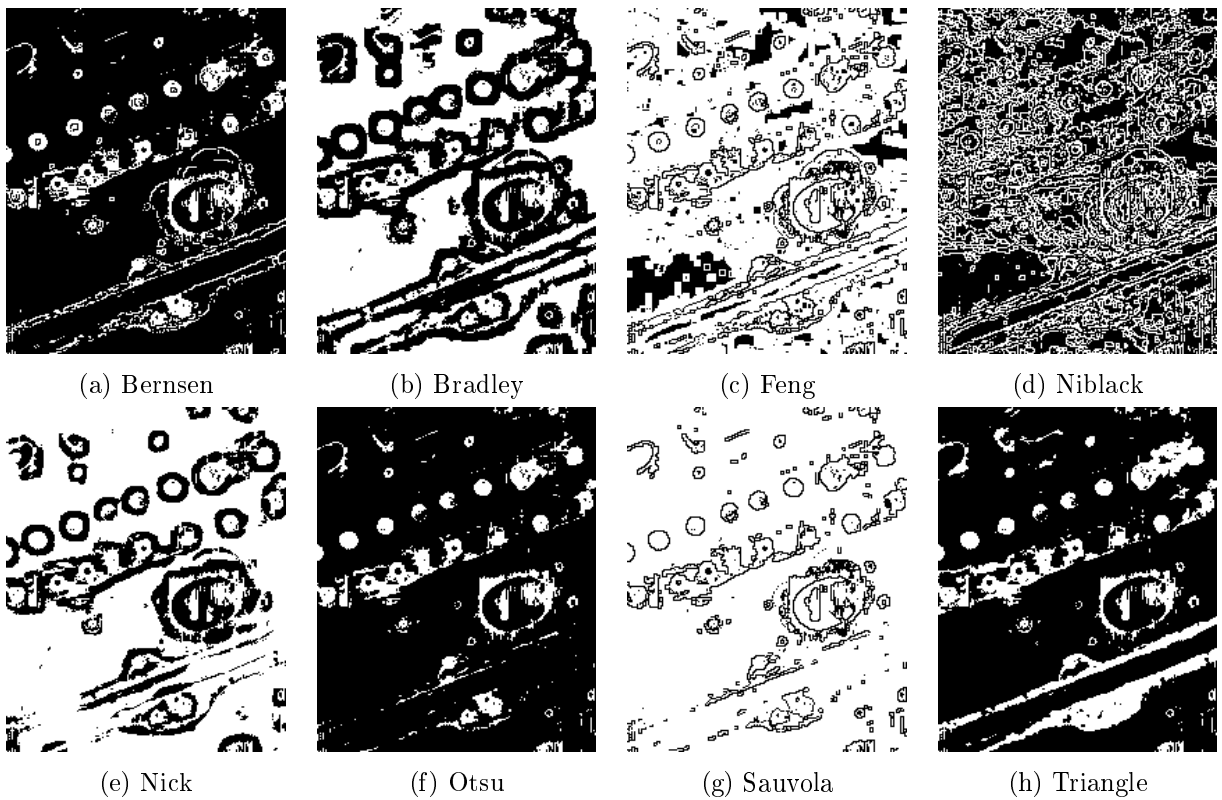


Fig. 6.4: Exemplary results of image thresholding (C-Scan of the aircraft panel)

6.2.2 Analysis of edge-based segmentation methods

The second group of tests was aimed at edge-based segmentation algorithms, where the Canny, Prewitt, Roberts, Sobel, and LoG detectors were used. In Fig. 6.5, the exemplary results of edge detection algorithms are presented.

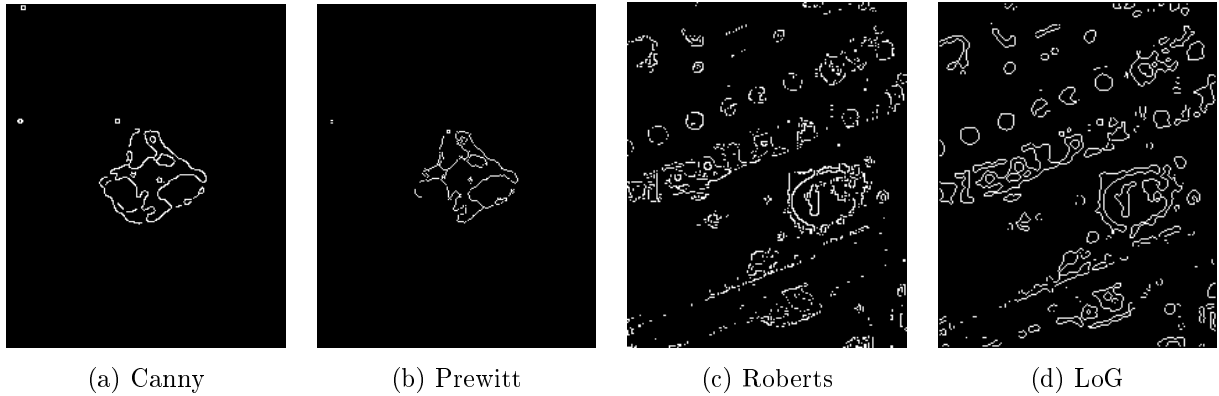


Fig. 6.5: Exemplary results of edge detection obtained for: the C-Scan of the impacted specimen (a,b); C-Scan of the aircraft panel (c,d)

In many cases, the produced edges do not have closed contours and a significant part of these edges does not represent contours of damage only. Using this approach, similarly as in the case of the bi-modal thresholding, it is not easily possible to extract damage regions only (i.e. clearly separate them from other elements or noise), thus the edge detection methods are regarded as not suitable for the considered problem.

The above-mentioned observations lead to the conclusion that multi-modal segmentation approaches are needed to be applied, i.e. the methods that enable obtaining more than two classes.

6.2.3 Analysis of clustering-based segmentation methods

Further tests were performed with the use of several methods, where the number of classes k must be provided as an input, namely the k -means, fuzzy c -means, multilevel Otsu, and GMM with EM clustering method. The experiment was performed for variable values of k in the range of 2–10 with a step of 1 in order to observe its influence on the segmentation accuracy. The exemplary segmentation results are presented in Fig. 6.6, for the impacted specimen, and in Fig. 6.7, for the aircraft panel.

A quantitative analysis of the segmentation results was performed and its summary is presented in Fig. 6.8. The segmentation accuracy was calculated as a correlation between the ground-truth image and the resulting binary image obtained by selection of one or

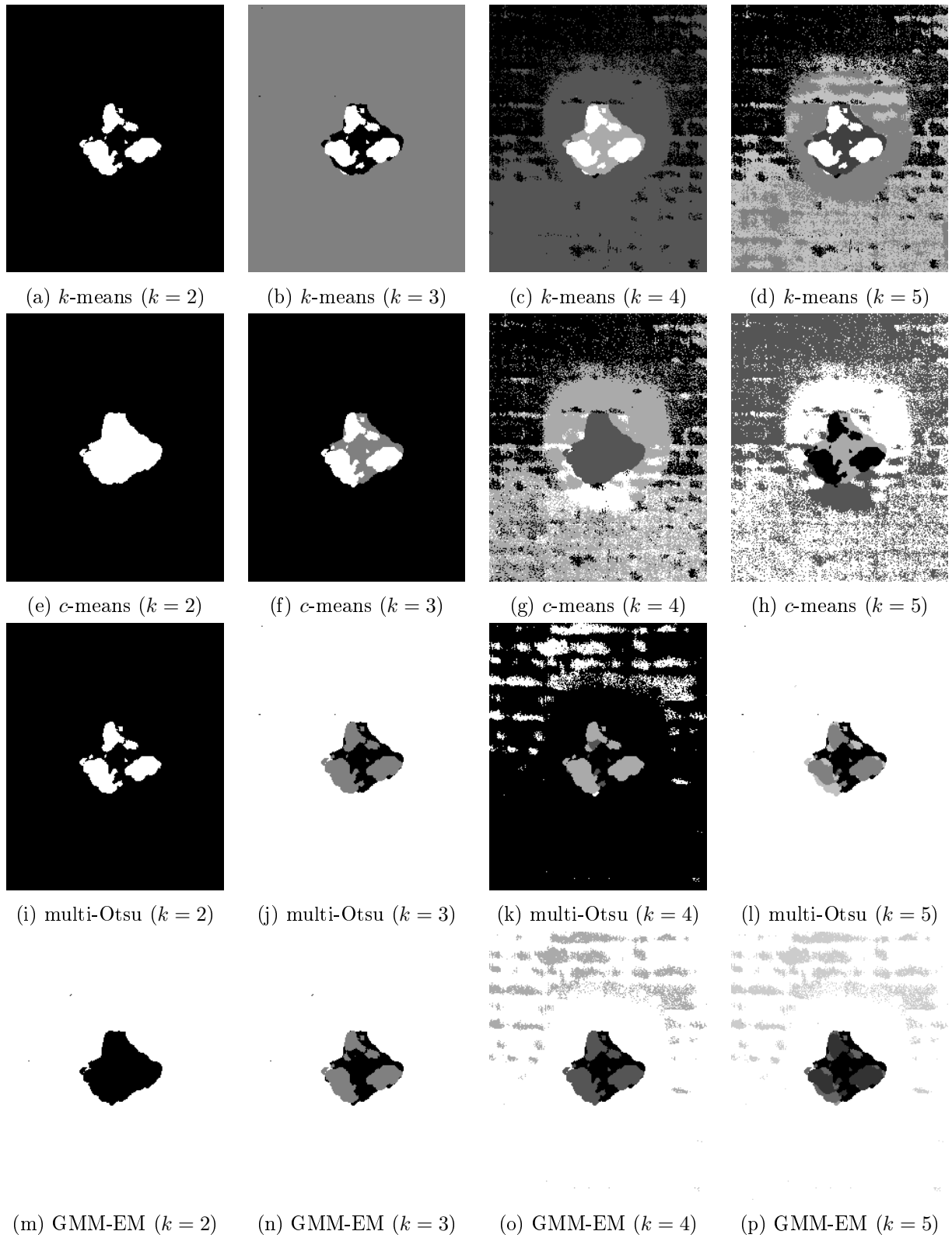


Fig. 6.6: Exemplary results of image segmentation (C-Scan of the impacted specimen) with different numbers of classes (given in brackets)

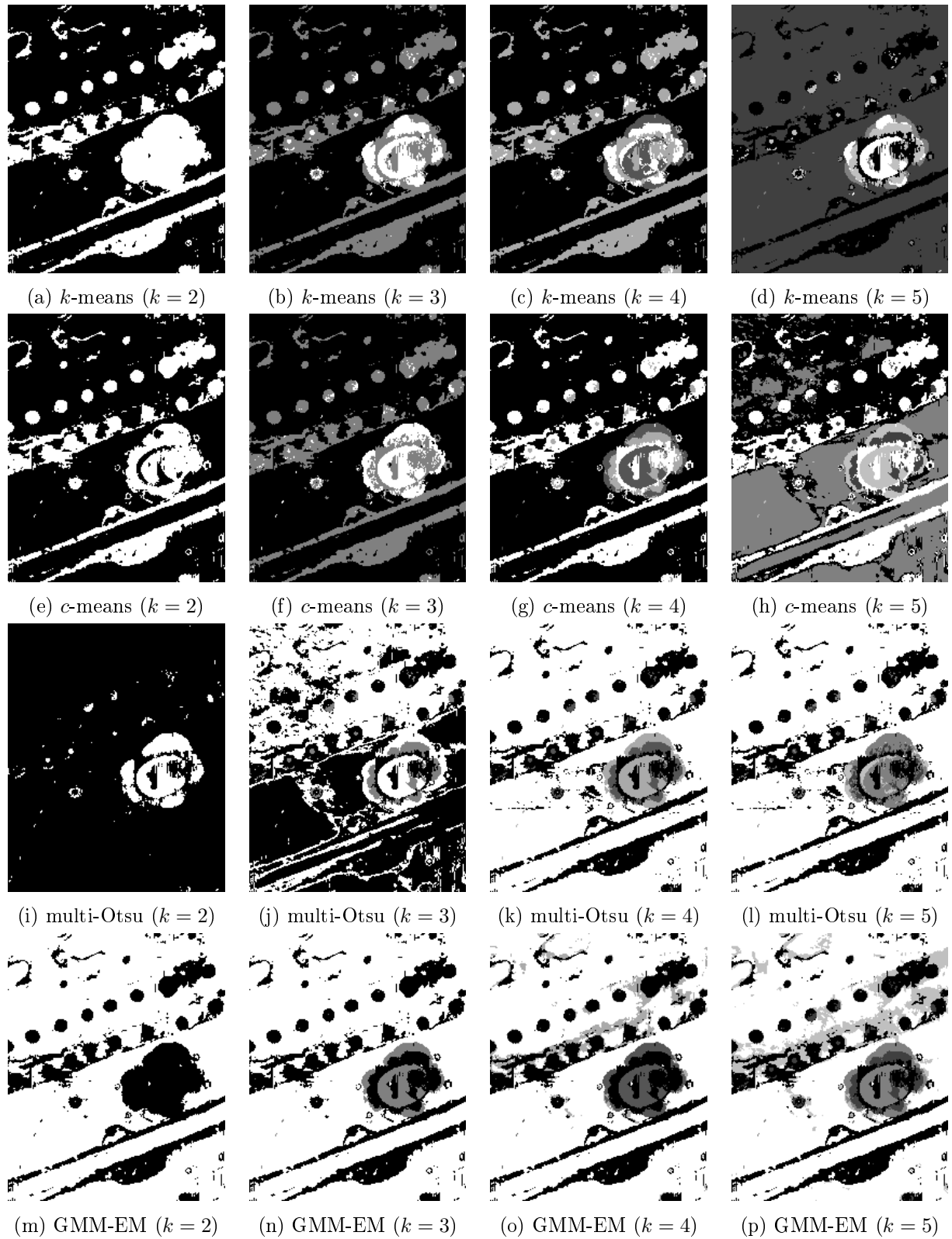
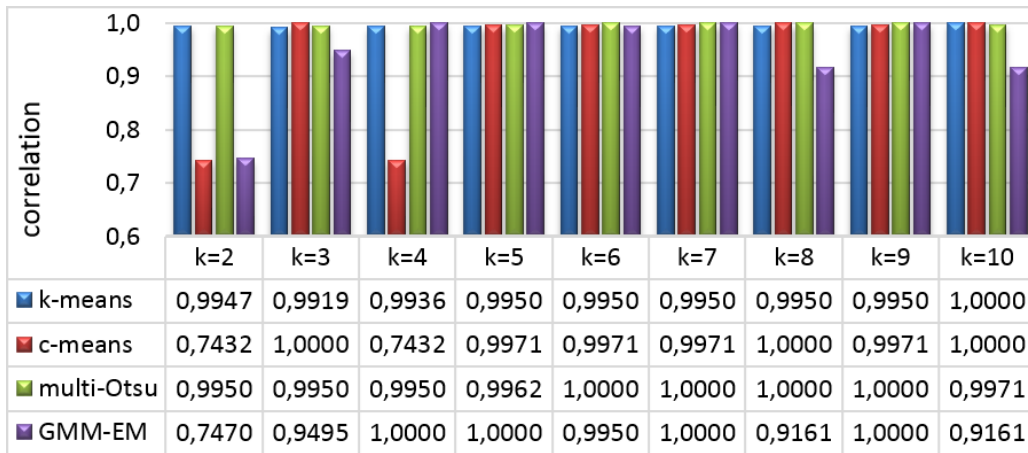
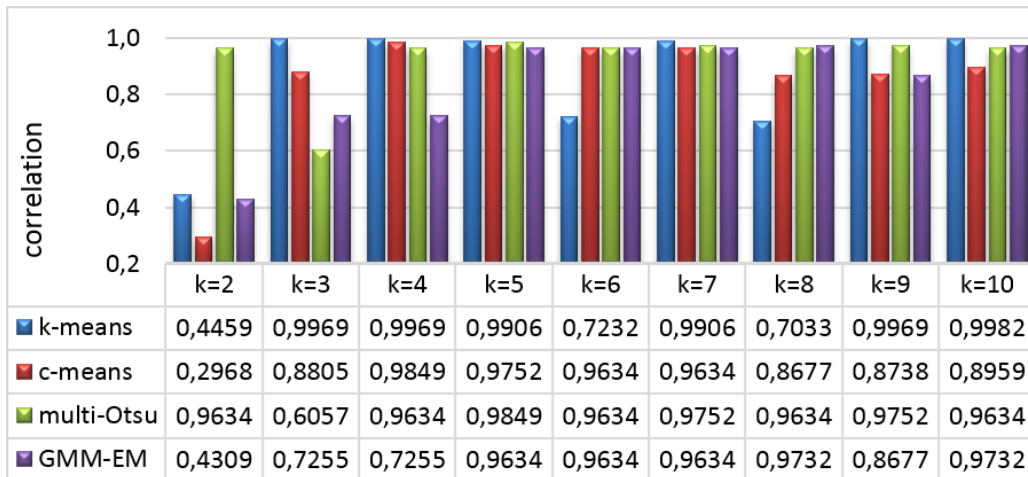


Fig. 6.7: Exemplary results of image segmentation (C-Scan of the aircraft panel) with different numbers of classes (given in brackets)

more classes from the segmented image – as damage. In the case of the impacted specimen, the segmentation accuracy using the k -means clustering and multilevel Otsu thresholding is in most cases very high, whereas using the c -means clustering and GMM-EM clustering it is changeable with the k variation. However, when analysed more complicated data, i.e. the C-Scan of the aircraft panel, the segmentation accuracy is very changeable for all the tested segmentation methods. These observations prove that selection of the number of classes k strongly affects the segmentation accuracy. Although the accuracy is in many cases very high, the necessity of the k selection makes these methods non-universal and inappropriate for the NDT applications.



(a) C-Scan of the impacted specimen



(b) C-Scan of the aircraft panel

Fig. 6.8: Segmentation accuracy obtained with the use of methods: k -means, c -means, multilevel Otsu thresholding and GMM-EM clustering

The next from the tested methods is the Mean Shift clustering algorithm. As it was mentioned earlier, the advantage of this approach is that selection of a number of classes

is not needed, however, a mean shift bandwidth parameter has to be provided. The experiments and quantitative analysis were performed for the bandwidth in the range of 0.1–0.9 with a step of 0.1. The exemplary segmentation results are presented in Fig. 6.9, and the summary of the quantitative analysis of the segmentation accuracy in Fig. 6.10.

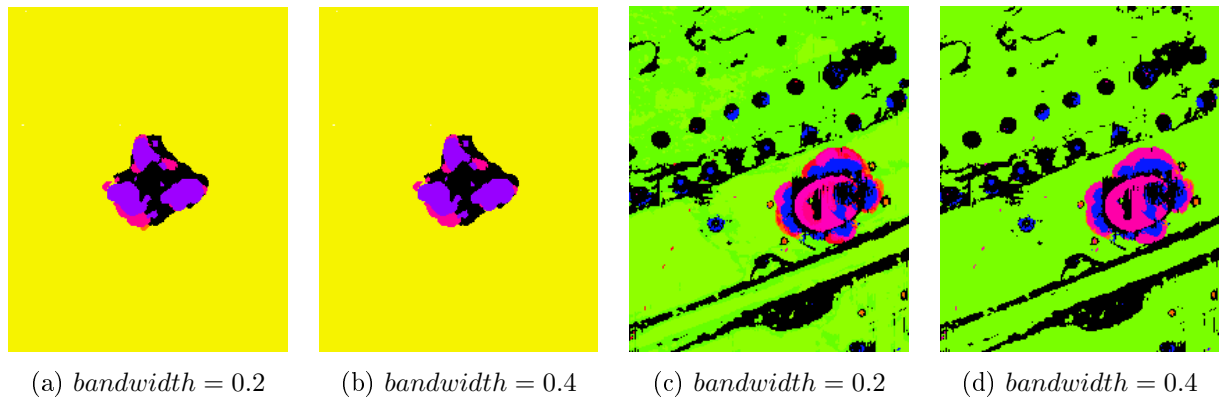
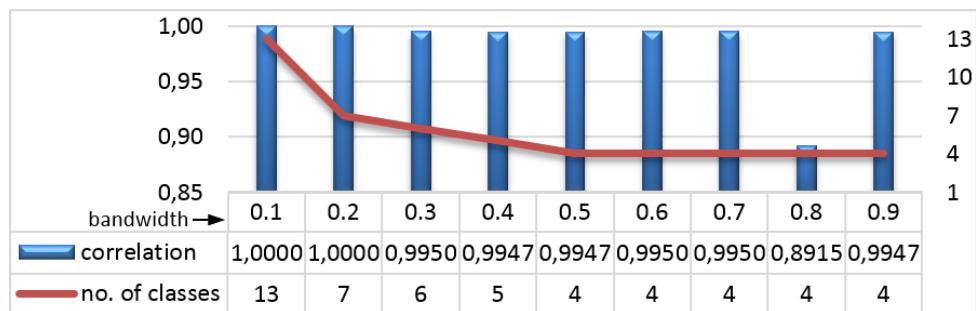
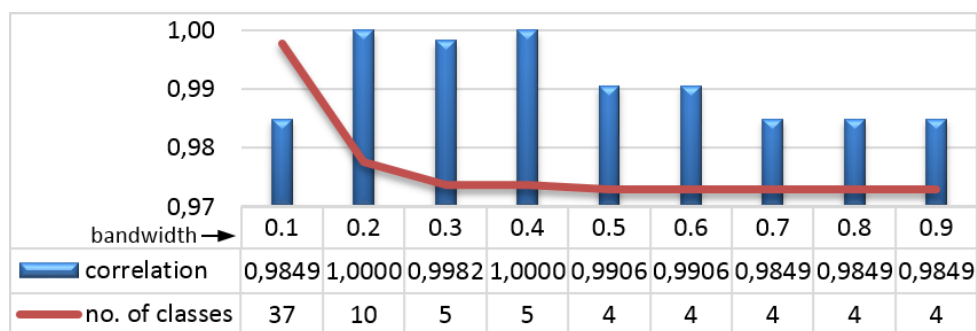


Fig. 6.9: Exemplary results obtained using the Mean Shift clustering algorithm for: the C-Scan of the impacted specimen (a,b); C-Scan of the aircraft panel (c,d)



(a) C-Scan of the impacted specimen



(b) C-Scan of the aircraft panel

Fig. 6.10: Segmentation accuracy obtained using the Mean Shift clustering algorithm

In the latter, the calculated correlation as well as the resulting number of classes for each selected bandwidth are set together. It can be observed that, although the segmen-

tation accuracy is in many cases very high, it is very dependent on the selection of the bandwidth, and there are several cases where, especially in the case of the aircraft panel, the accuracy is not satisfactory.

6.2.4 Analysis of region-based segmentation methods

The next of the tested groups of methods is the region-based segmentation. In Fig. 6.11, the exemplary results after the application of the SRM method are presented. Here, the number of classes is the output parameter, however, other input data, such as filtering parameters and a size of the smallest region allowed to be obtained, have to be defined. As it can be noticed in Fig. 6.11, for a small number of classes the damaged region is entirely filled or merged with other neighbouring regions. For larger numbers of classes the regions seem to be better segmented, however, it does not find a proof in the results of a quantitative analysis, presented in Fig. 6.12. The segmentation accuracy is far from satisfactory in all the cases, especially when considering the C-Scan of the aircraft panel. Moreover, the computing time of this algorithm is long.

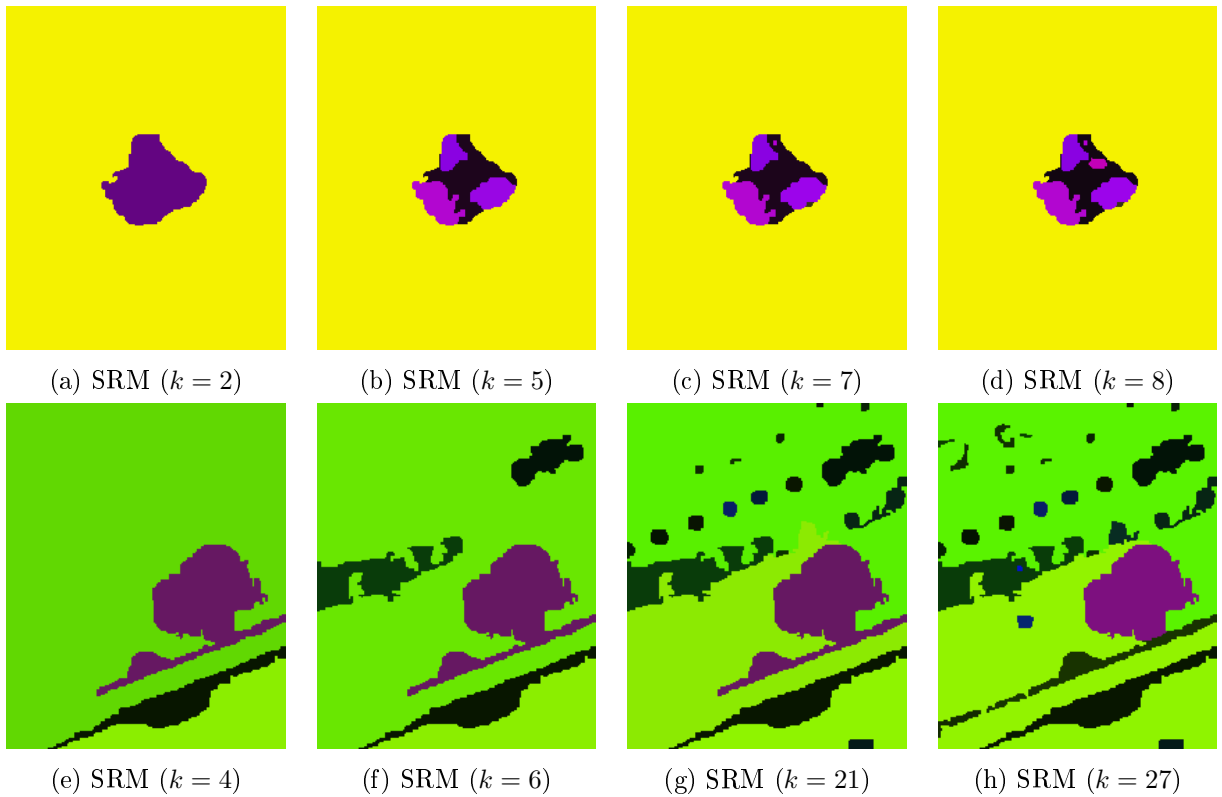


Fig. 6.11: Exemplary results obtained using the SRM algorithm for: the C-Scan of the impacted specimen (a–d) and the aircraft panel (e–h)

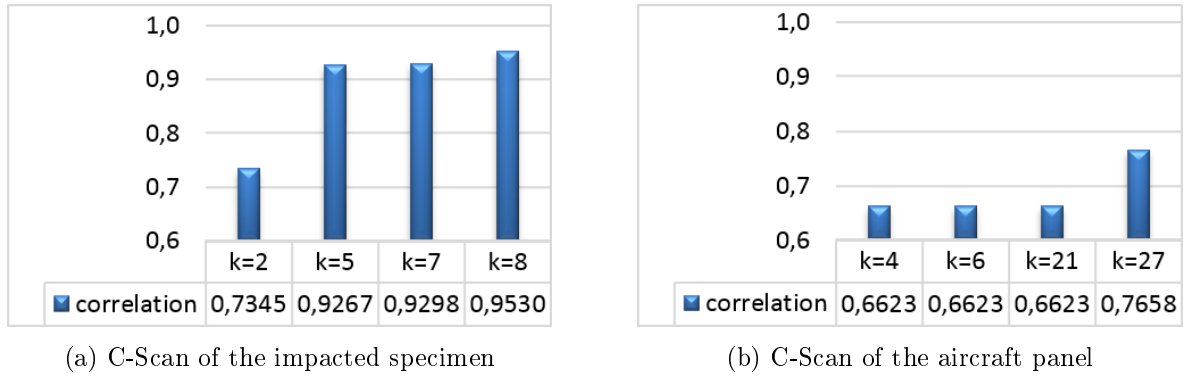


Fig. 6.12: Segmentation accuracy obtained using the SRM method

6.2.5 Analysis of other histogram-based segmentation approaches

Since all of the tested methods described above have some disadvantages, i.e. the main problem is the necessity of selection of input parameters, and thus, the lack of universality, it was decided to test several non-parametric histogram-based approaches based on own-developed algorithms.

The first approach is called a multilevel segmentation using a Minima-Between-Peaks (MBP) criterion. This consists in selection of all the local minima of the image histogram as the thresholds. Optionally, to reduce a number of the resulting classes, single pixels of particular intensity values can be excluded from the histogram, i.e. the frequencies lower than a given value are set to zero. The histograms of the tested C-Scans are presented in Fig. 6.13(a) and Fig. 6.14(a), respectively, for the impacted specimen and the aircraft panel. The dotted lines show locations of the obtained thresholds. The resulting images after segmentation using this approach are presented in Fig. 6.13(b) and Fig. 6.14(b), where one can also observe the resulting numbers of classes.

The second approach is based on the MBP algorithm with the difference that the histogram is smoothed before the minima detection step. Remarkably the elimination of some local noisy maxima in the histogram produces sharper distinction between the relevant segments. For the smoothing purpose, the one-dimensional median filters of a 2nd, 3rd, and 4th order were tested. The exemplary results, i.e. the smoothed histograms with indication on the thresholds' locations, and the corresponding segmented images are presented in Fig. 6.13(c,d), for the impacted specimen, and in Fig. 6.14(c,d), for the aircraft panel.

Filtering of the input C-Scans before processing of their histograms was also tested. Various types of two-dimensional filters, such as the averaging, or Gaussian low-pass

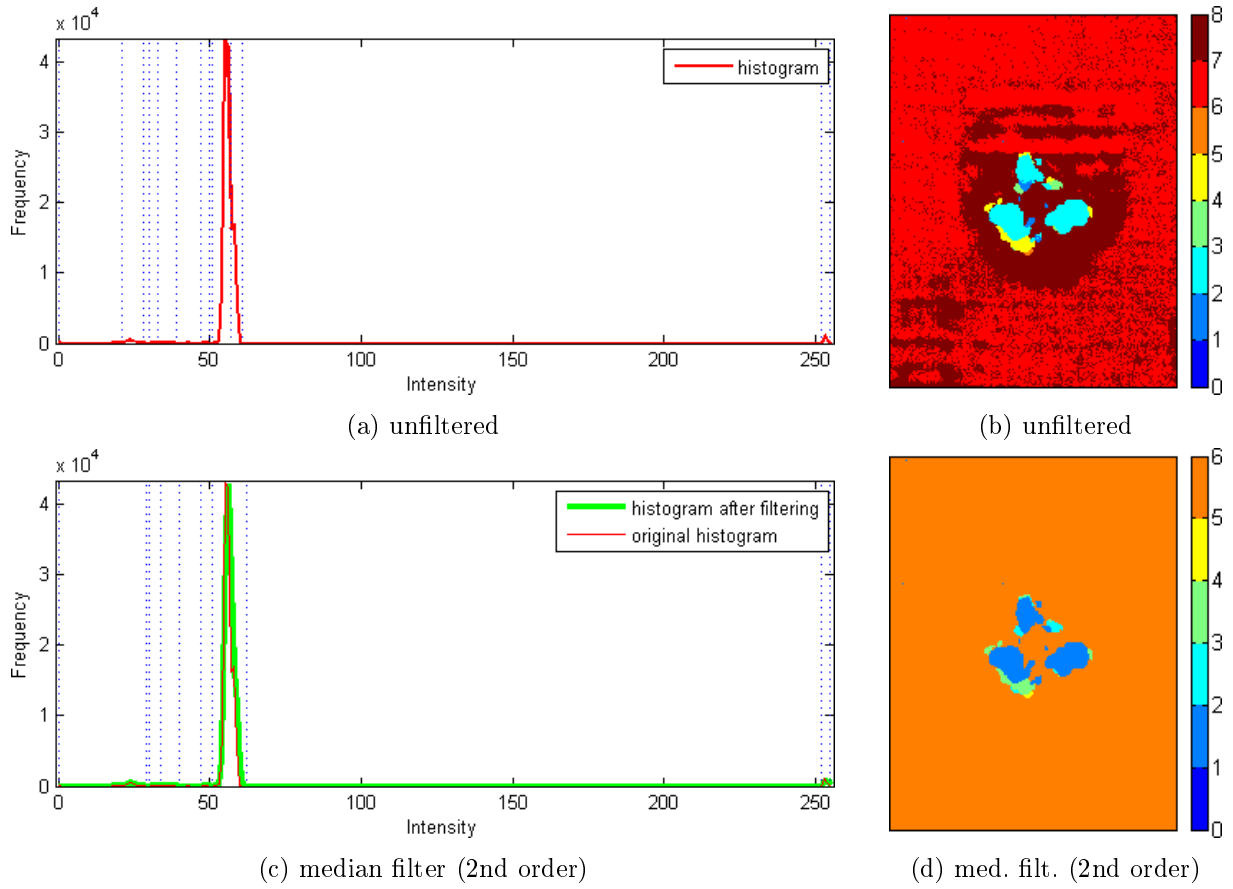


Fig. 6.13: Exemplary results obtained using the MBP approaches (for the impacted specimen)

filters, and variable scenarios of their sizes were tested. However, this approach did not bring satisfying results, since the segmented images have too large number of classes (for the C-Scan of the aircraft panel it is in the range of 37–54). Interestingly the post-filtering (smoothing the histogram) appears to be more efficient than applying filters on the physical image itself.

The last approach is based on the MBP algorithm and a probability distribution model criterion, which is called here Gaussian-MBP. In this approach, the histogram is initially segmented into levels using the basic MBP algorithm and then, a one-term Gaussian Model is fitted to each histogram level individually. With opportune normalisation, the interpolation by Gaussian density functions provides immediate probabilistic interpretation of the pixel assignment to one or another region. The intersection points of all the obtained Gaussian Models are the new threshold values. The resulting Gaussian models of the histogram (based on the C-Scan of the aircraft panel) are presented in Fig. 6.15(a) and their zoomed fragment, together with the original histogram and detected thresholds

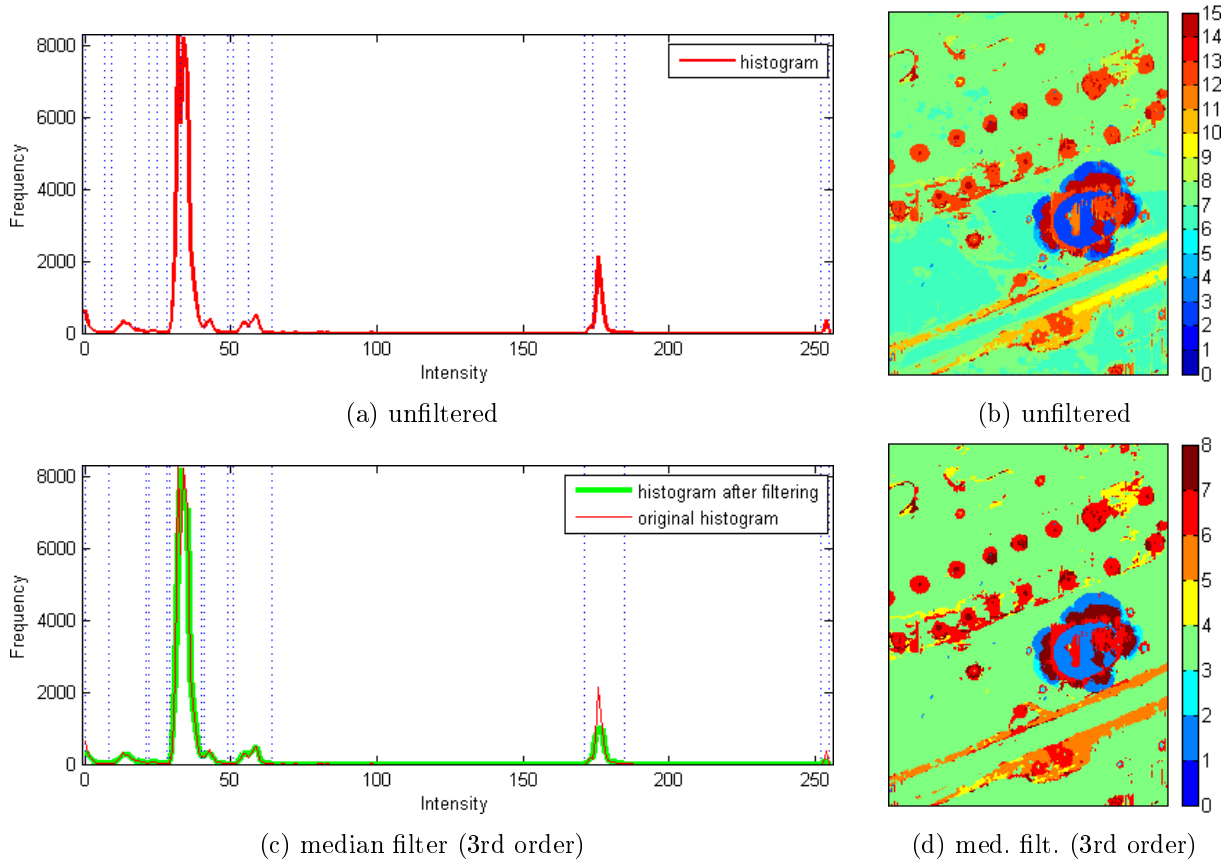
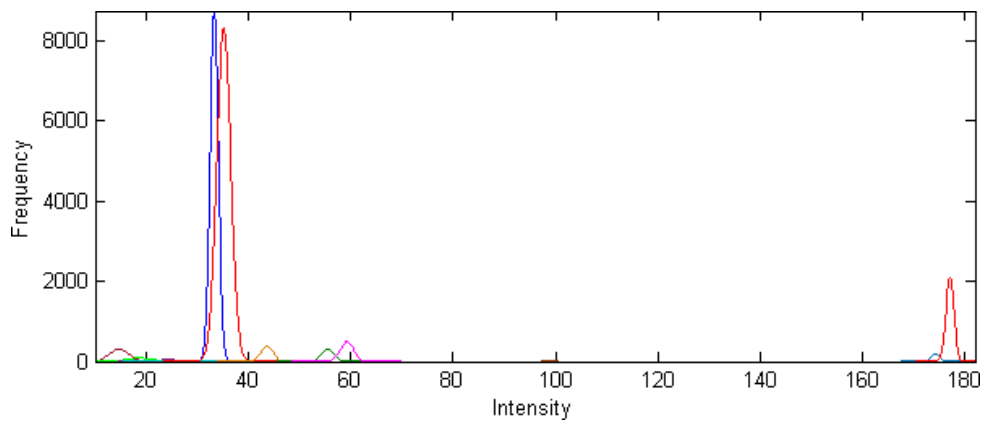


Fig. 6.14: Exemplary results obtained using the MBP approaches (for the aircraft panel)

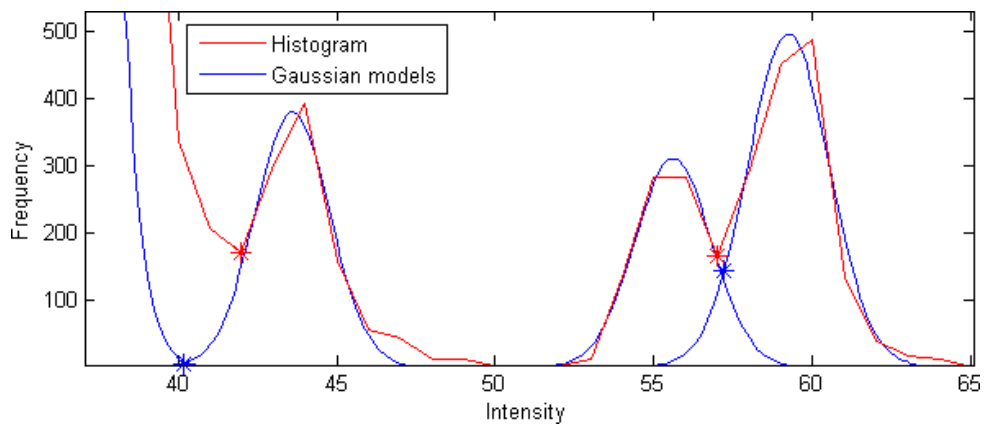
using both methods (MBP and Gaussian-MBP), in Fig. 6.15(b).

The segmentation accuracy obtained using the three approaches described above, together with the resulting number of classes, are summarised in Fig. 6.16. From these results one can notice that these very simple, non-parametric, approaches turn out to be of very high accuracy. The MBP approach without any filtering brought perfect results for the both tested C-Scans. Median filtering of the histogram enables reducing the number of classes along with the increase of the filter order, however, with a little loss of accuracy in certain cases. The Gaussian-MBP algorithm returned the exact results in the case of the C-Scan of the impacted specimen, whereas in the case of the more complicated C-Scan, the segmentation accuracy slightly decreases.

The proposed approaches have a main significant advantage over other segmentation methods tested in this study, that they do not require setting any input parameters, such as a number of classes k . The resulting k value is selected automatically and the algorithms are universal for both simple and more complicated tested cases.

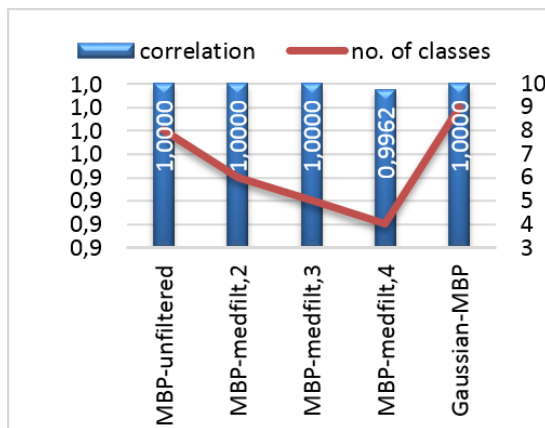


(a) Gaussian models of the histogram

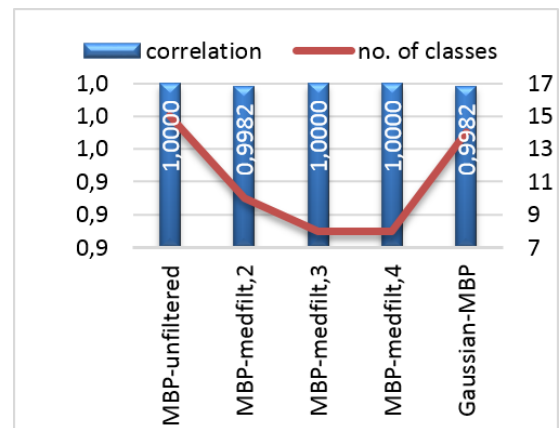


(b) a fragment of the Gaussian models and the original histogram

Fig. 6.15: Exemplary results of the Gaussian-MBP algorithm (for the aircraft panel)



(a) C-Scan of the impacted specimen



(b) C-Scan of the aircraft panel

Fig. 6.16: Segmentation accuracy obtained using the MBP and the Gaussian-MBP algorithms

6.3 Conclusions

The presented study was aimed at performing a comparative analysis of various types of image segmentation methods in the light of the accuracy of damage detection in ultrasonic C-Scans of composite structures. Several threshold-, edge-, clustering-, region-based, as well as proposed non-parametric histogram-based segmentation approaches were tested and the quantitative analysis of the results was depicted. The following summary conclusions were made after the analysis of the obtained results.

- The presented findings indicated several problems and drawbacks of the tested methods of image segmentation, mainly related to the necessity of the selection of the input parameters, such as the number of classes k , which strongly affect the detection accuracy, or long computation duration.
- Several simple, very fast and non-parametric histogram-based approaches were proposed and their calculated accuracy revealed their suitability for the aim of the analysis of ultrasonic scans of composite materials.
- The high detection accuracy for the proposed methods was obtained both for simple as well as more difficult tested cases, which allows considering these approaches as universal.

Considering the obtained results and presented conclusions it was decided that the proposed MBP-based image segmentation, for which the detection accuracy was the highest, will be used in the algorithms applied for further experiments.

7. Analysis of 3D damage reconstruction and visualisation

The aim of this research stage was to develop a method for 3D damage reconstruction and visualisation based on ultrasonic scans in order to facilitate interpreting data during the NDT&E procedures. This chapter presents proposed approaches to such a 3D visualisation based on an ultrasonic C-Scan as well as based on a sequence of B-Scans. In order to check the suitability of such a reconstruction, one of the most complex type of damage commonly occurring in CFRP structures was considered, namely the impact damage. For this purpose, ultrasonic data obtained by testing of a CFRP composite element with BVID was used. It is assumed that the damage extraction using image segmentation methods and its 3D reconstruction and then visualisation by volume rendering may be useful in quick assessment of the damage character. Another advantage is a possible reconstruction of the internal design of the structure, which can be useful for precise assessment of the damage location, e.g. with respect to composite layers, as well as to determine the true size of damage.

Additionally, to verify the obtained reconstruction results – they were compared with the reference data being the 3D damage representation extracted based on the X-ray CT scans. The CT was chosen since it is considered the most sensitive and precise method for analysing inner and outer geometry of various types of objects. It should be highlighted that the extensive dimensions of composite aircraft components disqualify them from regular inspections with the use of CT. Taking into account the limitations of the CT method regarding the maximal dimensions of elements to be tested, a small specimen with artificially introduced impact damage was employed for this research stage. Initially obtained results presented in this chapter were published in (Wronkiewicz *et al.*, 2016).

7.1 Structures and experiments

7.1.1 Specimen preparation

The CFRP specimen used in this research stage consists of I7 carbon fibres and MTM45-1 epoxy matrix. The laminate has a balanced stacking sequence of $[0,45,90,-45]_S$ and 32 plies

are superposed to obtain the thickness of 4 mm. The planar dimensions are 100×150 mm. The fabrication process consisted of debulking, vacuum bagging and curing. The specimen was cured at 180°C for 3 hours under 6 bar pressure.

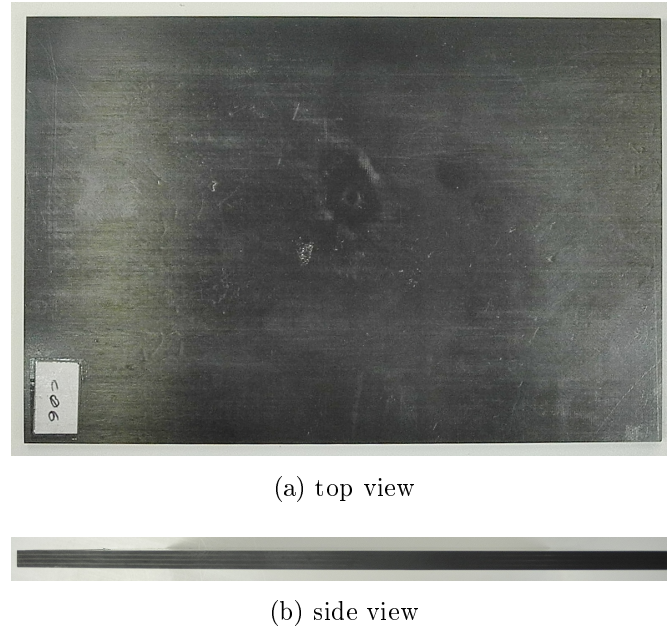


Fig. 7.1: Views of the CFRP specimen with BVID

The specimen underwent an impact test, which was performed by means of a drop test apparatus. The experimental set-up consisted of a plexiglas tube to guide an impactor toward the specimen, which was grounded with steel frames in order to assure proper boundary conditions. The speed of the impactor was measured by laser acquisition, thus allowing to estimate the impact energy, resulting in 30 J. The top and side views of the specimen are depicted in Fig. 7.1. The impact caused BVID with global dimensions of 50.3×64.5 mm (Fig. 7.2), as measured by means of UT described below.

7.1.2 Ultrasonic testing

UT of the specimen was performed with the use of FlawInspecta[®] scanner, described in section 5.1.3, with a frequency of 5 MHz. The UT results are depicted in Fig. 7.2 (amplitude and ToF C-Scans) and Fig. 7.5 (selected sequence of B-Scans). One can observe that the damaged regions contain many areas coloured in different manner which is related to damage existence at various depths. This phenomenon is connected with a specific nature of impact damage in composite structures, as described in section 2.2.2.

The colour scales that correspond to ranges of the echo amplitude and the ToF are presented on the left to these C-Scans. A particularly useful when considering the spatial

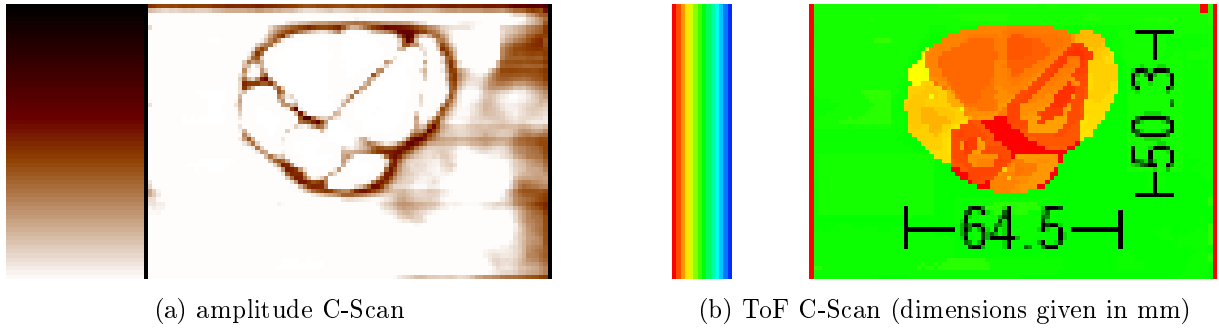


Fig. 7.2: The results of ultrasonic inspection of the specimen (C-Scans)

assessment of damage is the ToF scale (visible in Fig. 7.2(b)) which gives information about depth location of particular BVID regions. In this case, the regions visible as yellow pixels are located the deepest with respect to the areas of red pixels and of the shades of orange located between them.

7.1.3 X-ray CT testing

The specimen was investigated using the X-ray CT system – GE phoenix v|tome|x m industrial CT Scanner, manufactured by GE® Measurement & Control Solution (Billerica, MA) with a maximal power of 500 W at 300 kV voltage and a GE® DXR detector array. The tests were carried out under the following conditions: voltage of 120 kV, current intensity of 120 μ A and timing of 330 ms. The specimen was located 80–100 mm from the radiation source, determining a voxel size of around 20–50 μ m. The specimen was installed on a rotating holder at an angle of 30 degrees with respect to the beam in order to provide a uniform illumination. The rotation step was 0.25 degree. The tomogram (produced CT image) was reconstructed using a graphical station with Phoenix Datos|x CT software dedicated to automated data acquisition. Then, Volume Graphics VGStudio MAX 2.2 software was used for initial processing of the tomogram, where the contrast properties between the damaged and healthy regions were enhanced. After that, the pre-processed CT scan was exported as a sequence of 962 planar slices to be further processed. Selected CT slices from the top view of the specimen are presented in Fig. 7.3.

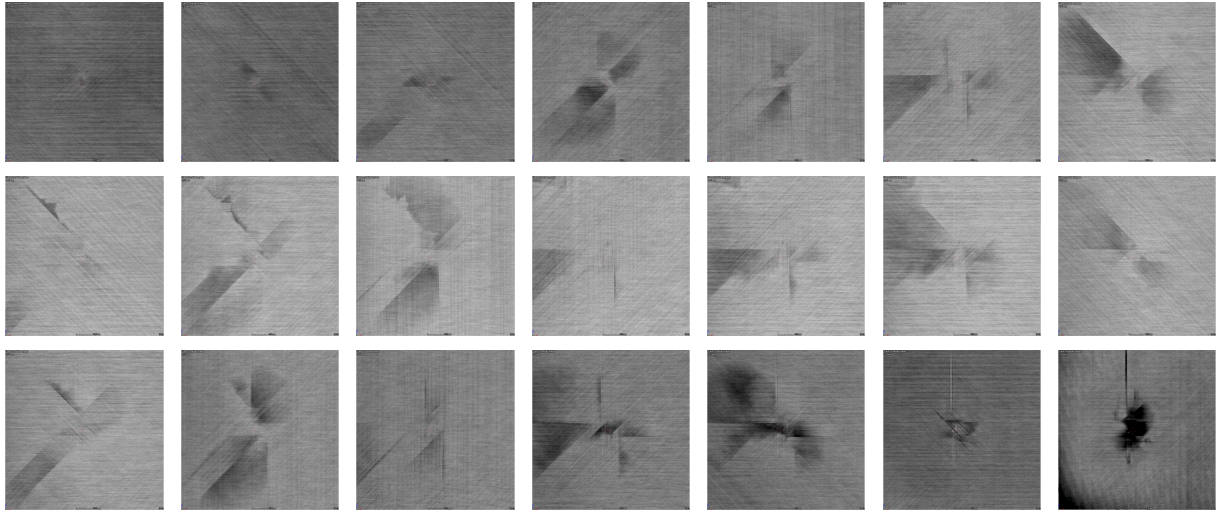


Fig. 7.3: Selected slices of the tomogram (no. of slices between 80–820)

7.2 3D damage reconstruction based on ultrasonic C-Scan

The applied in this step image processing algorithm can be divided into two steps: damage extraction and 3D reconstruction with its visualisation. Firstly, the raw ToF C-Scan of the tested specimen, in a form of 8-bit matrix, was loaded into the Matlab® workspace as an image. Then, this image was segmented using the MBP-based image segmentation algorithm, introduced in section 6.2.5. After that, the BVID regions were initially extracted by selection of the segments that are to be left in (or removed from) the image. This means that the pixels for which the labels are different than the selected ones are assigned to zeros. An additional step was the extraction of a contour around the obtained BVID regions and calculation of their surface area, which reached 2219.1 mm² for the considered specimen.

The second step was the reconstruction of the extracted damage to a 3D form in such a way that the values of the 2D image were distributed to a 3D data array, where each unique value lies on a level (layer) corresponding to this value. This means that the additional dimension represents colours (depths) of particular damaged regions. The obtained 3D image can be rotated in three axes in any manner (see selected views in Fig. 7.4).

Analysing the obtained results one can observe that this very simple 3D reconstruction of the C-Scan allowed for the expected improvement in damage visualisation. The distribution of the BVID regions at particular depths of the specimen are more clearly

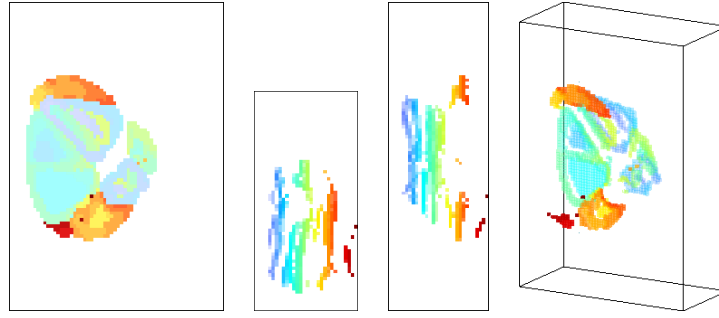


Fig. 7.4: 3D damage visualisation based on the reconstructed ToF C-Scan

visible when compared to the raw 2D C-Scan and they can be promptly noticed without necessity of comparing the C-Scan areas with the colour scale. However, the reconstructed 3D geometry of the BVID is incomplete due to the character of C-Scans since, as it was mentioned before, delamination regions which are closest to the front surface hide delaminated areas located underneath. It is expected that appropriate processing of all the obtained B-Scans will allow for more complete damage characterisation.

7.3 3D damage reconstruction based on ultrasonic B-Scans

The consecutive steps of the B-Scan-based damage reconstruction are as follow. A series of B-Scan maps, originally recorded in a form of a video, was converted into a sequence of 93 images, presenting the consecutive cross-sections of the specimen (selected sections are presented in Fig. 7.5).

Then, all of these images were converted into a 3D matrix by stacking them sequentially according to the order of the ultrasonic scanning path. Visualisation of the obtained raw 3D matrix is presented in Fig. 7.6(a) as well as with set transparency in Fig. 7.6(b), where one can notice the existence of the internal damage. In order to quickly obtain two matrices – the first one with voxels representing only the damaged regions of the specimen and the second one with voxels of the undamaged areas, it was decided to apply global thresholding. In this case, the threshold value for the entire 3D matrix was selected manually. Then, three versions of 3D damage representation were proposed. Firstly, both matrices (the BVID and the healthy regions) were displayed simultaneously with selected transparency, while the values of voxels in the matrix with the damage were emphasized in a resulting image by multiplying their values (Fig. 7.6(c)). The second version is the display of only the matrix with the damage without any transparency (Fig. 7.6(d)).

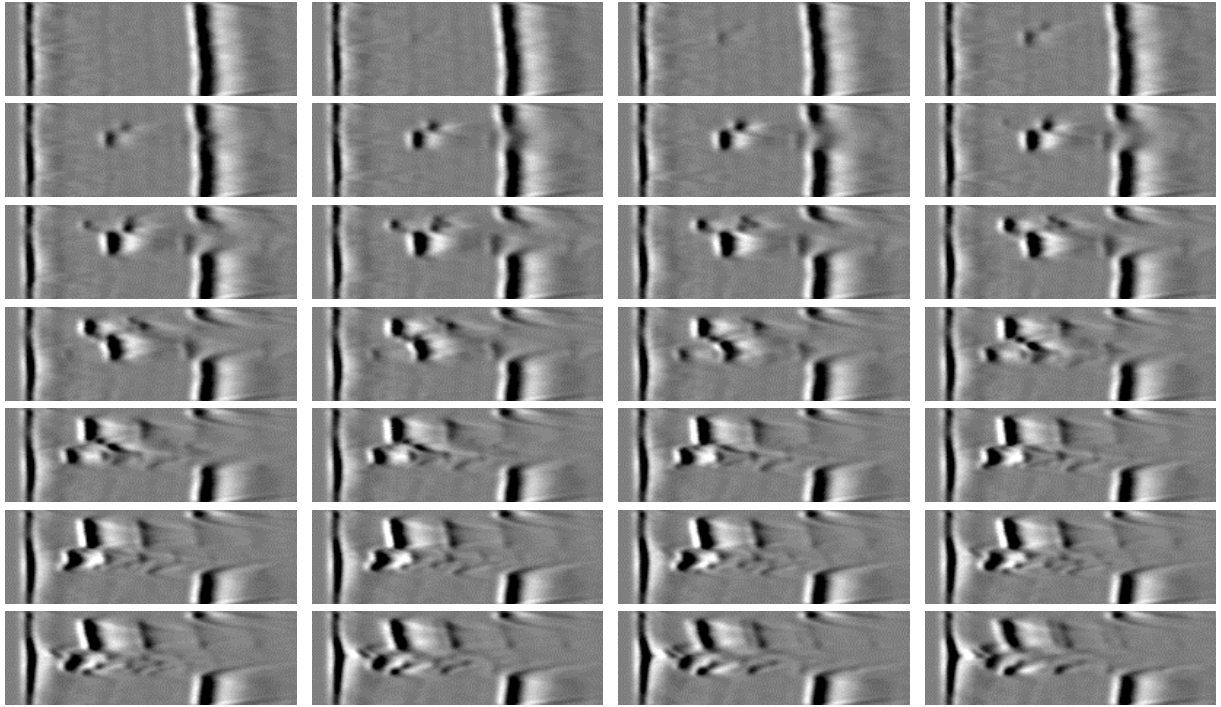


Fig. 7.5: Selected sequence of ultrasonic B-Scans (sections no. 18–45)

Fig. 7.6(e) presents a semitransparent damage visualisation where the delaminated regions at different layers are distinguished with individual colours. This was achieved by changing the non-zero values in the matrix with the new values that decrease along with the increase of the specimen's depth (i.e. the third dimension of the matrix).

As can be observed in Fig. 7.6, not only the internal damage is visible but also the top and bottom surfaces of the specimen. In order to obtain better visualisation results, the matrix was limited by excluding a selected range of columns. Final graphical representations in two selected versions analogously to the above described ones are depicted in Fig. 7.7 (shown from bottom side of the specimen). It can be noticed that the BVID is very well visible on the resulting visualisations and the reconstruction of B-Scans provides more details than the reconstruction of the C-Scan. Additionally, in Fig. 7.7(b,c), some of the layers of the CFRP composite are distinguishable, which can also be useful in the assessment of the damage location.

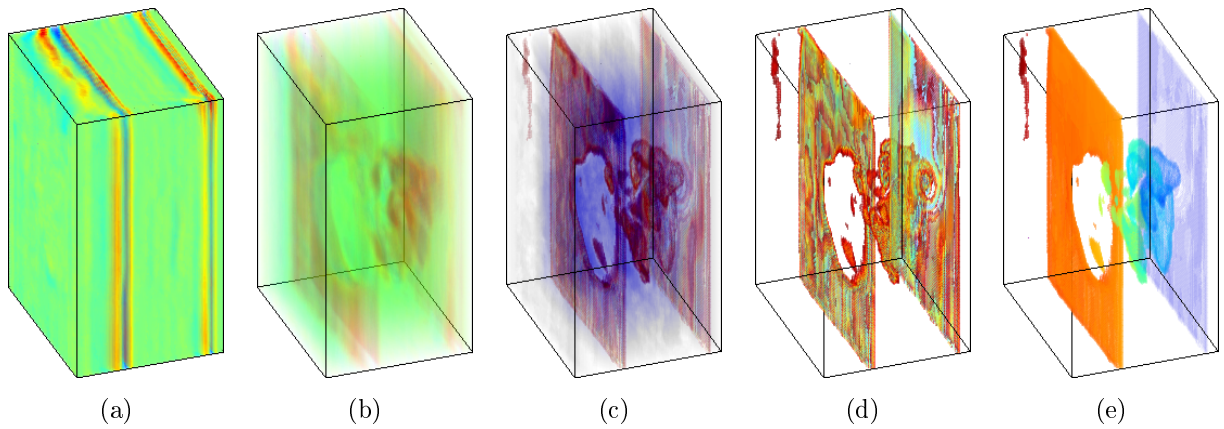


Fig. 7.6: Raw 3D matrix of a series of B-Scans without (a) and with set transparency (b) and three versions of their initial processing (c-e)

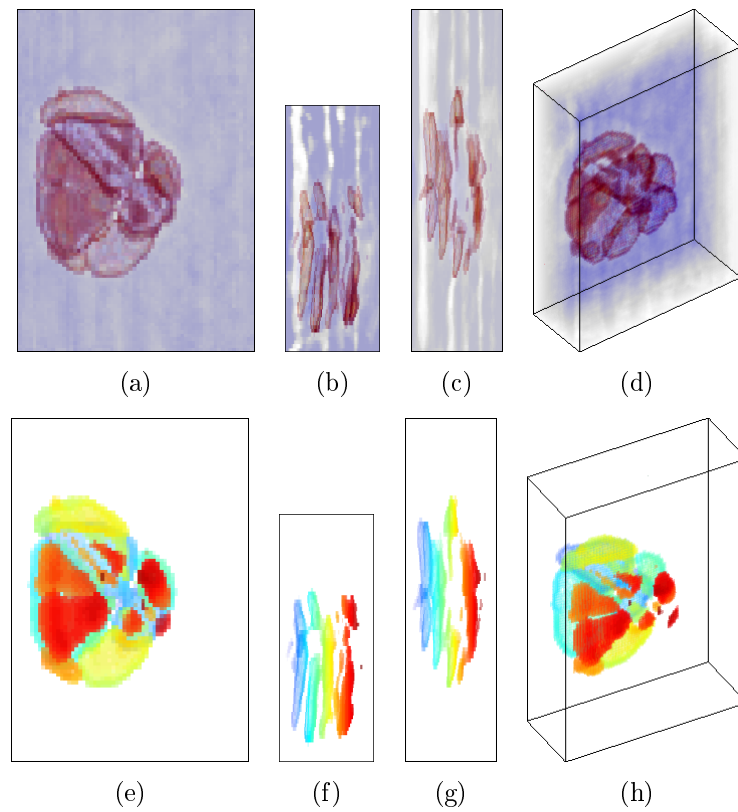


Fig. 7.7: 3D damage visualisation based on the reconstructed series of B-Scans (emphasized BVID (a-d), only BVID with changed colour map (e-h))

7.4 Verification of 3D damage reconstruction based on CT method

As previously mentioned, the aim of the last step of this research stage was to verify the conformity of the 3D reconstruction of the internal damage from the ultrasonic scans on the basis of the reference data acquired with the X-ray CT method.

The raw 3D image of the specimen (shown from its bottom and lateral sides) is presented in Fig. 7.8(a–d), where a crack at the bottom of the structure is very well noticeable. The CT slices extracted from the tomogram were processed using a similar algorithm to the one used for the B-Scans processing with the main difference that adaptive thresholding instead of global thresholding was applied. Firstly, adaptive thresholding with manually selected parameters was applied for each particular slice to initially extract the BVID regions. Then, morphological opening was applied in order to clean small clusters of voxels probably being noise. After that, all resulting slices were stacked sequentially to form a 3D array. 3D graphical representation of the resulting matrix with exclusion of the layers representing external surfaces of the specimen is presented in Fig. 7.8(e–h). One can notice that most delaminated regions are convergent with those detected using UT, however, CT revealed more delaminations being the closest to the top surface of the specimen. It is caused by location of these missing near-surface delaminations in a transducer dead zone during UT. After limiting the range of the displayed CT slices of the 3D matrix to the ones being in compliance with the ultrasonic data, and changing the colour map, the results depicted in Fig. 7.8(i–l) were obtained. When compared the results of 3D reconstruction of the ultrasonic scans and the limited range of the CT scans one can notice a good correlation between the delaminated areas (cf. Fig. 7.8(i–l) with Fig. 7.7(e–h)). It can also be seen that the delaminated regions are more widespread in the case of the results obtained from X-ray CT, however, their location and general shapes are comparable. This is due to the very high sensitivity of the CT method and necessity of applying additional advanced operations for the purpose of removing artefacts from the tomogram, which was not included in this study. These fundamental results and observations made are sufficient to state that 3D damage reconstruction from ultrasonic scans, especially B-Scans, allows for reliable visualisation of damage geometry and location inside the tested composite element. However, it should be kept in mind that near-surface damage being in the dead zone cannot be visualised, which is a drawback of the UT method.

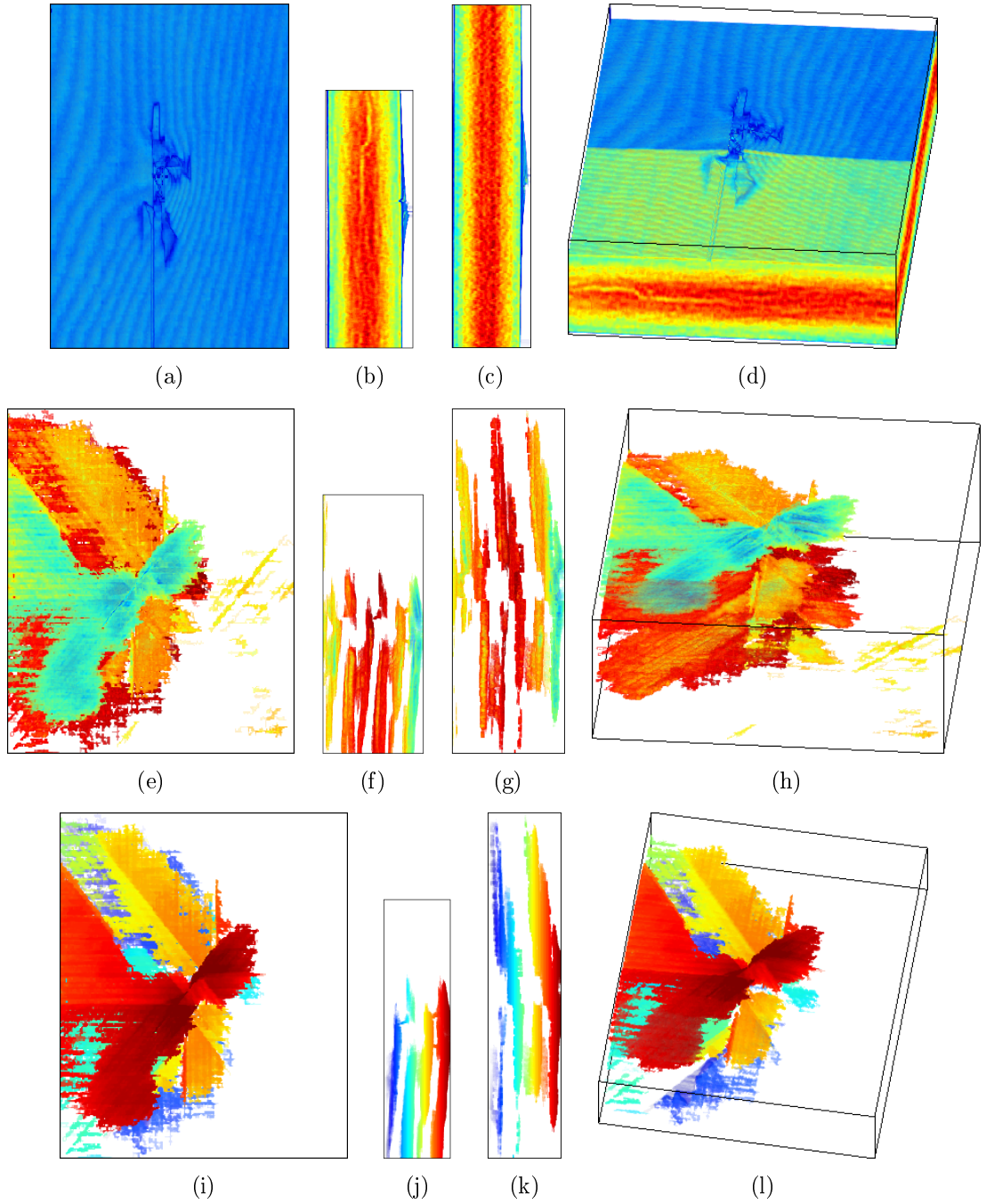


Fig. 7.8: 3D damage visualisation based on the reconstructed CT slices

7.5 Conclusions

In this chapter, approaches to 3D reconstruction and visualisation of ultrasonic scans for the purpose of facilitating NDIs of composite structures were presented. The ultrasonic C-Scan and a series of B-Scans of the CFRP specimen with artificially introduced BVID were used. The proposed algorithms are based on damage extraction using image seg-

mentation methods, reconstruction to a 3D array and volume rendering for the aim of its proper display. Conformity of the 3D reconstruction of the delaminated areas was verified on the basis of the reference data acquired with the X-ray CT method. Since impact damage is characterised by a cascade of multiple delamination regions it was possible to assess whether delaminated areas were properly visualised with respect to their location and composite layers. Accomplishing of these steps allowed for making the observations and summary conclusions as follow.

- A good correlation was noticed between the characteristics of damage areas reconstructed from the ultrasonic scans and the CT scans, especially their shapes and locations. Therefore, it was found out that the proposed approach allows obtaining reliable information about the damage geometry in three dimensions.
- The 3D damage reconstruction based on both C-Scans and B-Scans may facilitate interpretation of ultrasonic data and can be a useful tool during NDE of composite elements. However, delaminated regions near to the top surface of the specimen could not be visualised at all due to their location in the dead zone during UT.
- The B-Scan-based reconstruction returns much more details when compared to the C-Scan-based one. However, reconstructed C-Scans are still more informative than the raw C-Scans and can also be used in the case when acquiring B-Scans is not available in the applied testing equipment.

8. Examples of the application of the developed image analysis algorithms

The proposed image analysis algorithms presented in chapters 5–7 were tested by the application to selected case studies. These are presented in three sections and cover the investigations on:

1. impact damage detection and evaluation in CFRP specimens;
2. delamination size monitoring in CFRP aircraft elements; and
3. 3D damage reconstruction and visualisation in CFRP aircraft elements.

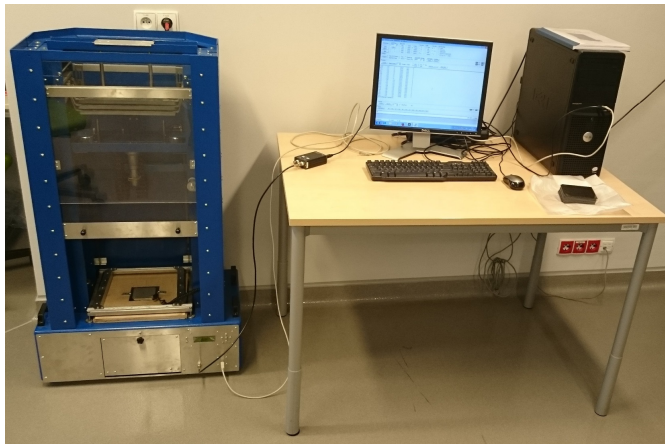
8.1 Impact damage detection and evaluation in CFRP specimens

The aim of the study presented in this section was to investigate the usefulness of the proposed image analysis methods in the area of analysis of low energy impact damage extent in CFRP composite elements. The second purpose was to study the dependency between impact parameters and visibility of the resulting damage on the outer surface of tested specimens and the total area extent of the internal damage. In order to obtain a wide range of impact damage cases, various BVID scenarios were considered, i.e. different impact energies and shapes of impactors were used during preparation of the specimens, which resulted in variable damage shapes and extents.

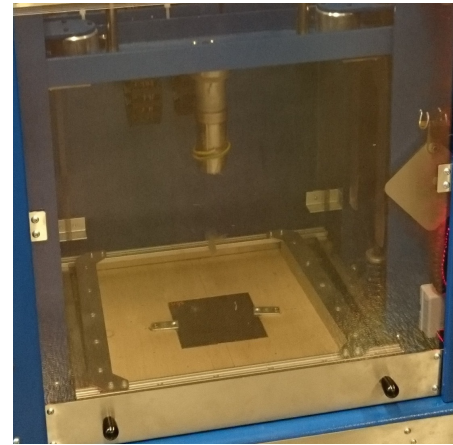
8.1.1 Structures and experiments

In this stage of study, the CFRP plates derived from the same series of plates as those described in section 5.1.1 were used. The specimens were damaged using the impact test rig (see Fig. 8.1) to obtain various BVID scenarios. In order to simulate various impact configurations the hemispherical impactors as well as the impactors with fixed granite stones were used. During the tests seven types of impactors were applied, as presented

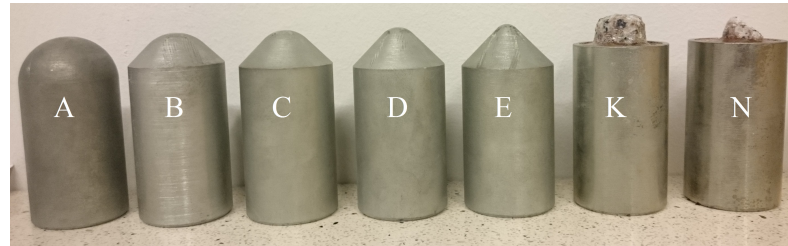
in Fig. 8.1(c). With regard to aircraft structures, the use of these impactors allowed simulating impacts by hail, dropped maintenance tools, or runway debris of various sizes. It was assumed that the range of impact energy causing barely visible damage in the used specimens is in the range of 5–20 J, and the energy step of 2.5 J was established in the study. The combinations of seven impactor types and seven impact energy values gave 49 impact damage cases in total.



(a) test rig



(b) specimen fixing



(c) impactors

Fig. 8.1: Impact test rig (a,b) and used impactors (c) – hemispherical (radii R given in mm): A – $R17$, B – $R14$, C – $R11$, D – $R8$, E – $R5$, stone impactors: K – with flat surface, N – with rough surface

As expected, barely visible or no signs of potential damage could be noticed when visually observed the specimens' surfaces. The photographs of the specimens' surfaces after the impact for selected cases are presented in Fig. 8.2. It was noticed that the impact signs are visible for the cases where the impactors of a rough surface (the impactors K and N) were used as well as for the cases of the impact energy of 15 J and above. For most of the rest cases, the visual inspection with the bare eye revealed no damage.

Afterwards, the specimens were tested with the Pulse-Echo UT method using the MAUS[®] system with the selected parameters described in chapter 5. The raw C-Scans

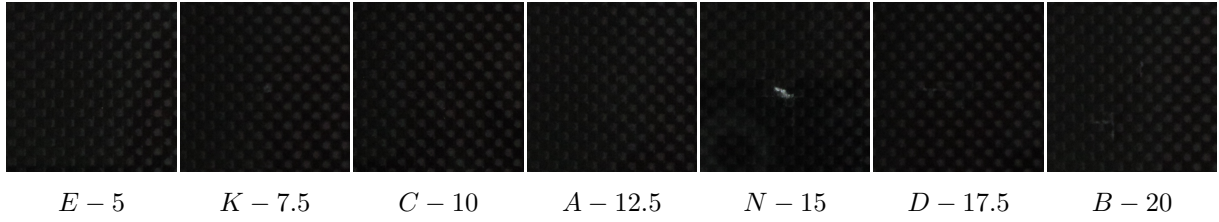


Fig. 8.2: Exemplary photographs of the specimens' surfaces after impact (limited to the central areas of 35×35 mm)

obtained from UT are presented in Fig. 8.3. From these results one can notice that the introduced impacts caused internal damage occurrence for all the cases with the impact energies in the range of 7.5–20 J, whereas not all the cases with the impact energy of 5 J resulted in damage. It is also noticeable that the prepared specimens allowed obtaining a variety of damage shapes including cracks and delaminations.

8.1.2 Image analysis algorithm

Selected steps of the image analysis algorithm prepared for the BVID evaluation, for the exemplary specimen case $K - 15$, are presented in Fig. 8.4. The consecutive steps are as follow. Firstly, the raw C-Scan is segmented using the developed MBP-based algorithm presented in section 6.2.5. The resulting image for the exemplary case is presented in Fig. 8.4(a). Then, the segments presenting undamaged regions are indicated to be removed from the image, i.e. assigned to zeros. This indication is reached by the interactive selection of one pixel point per one segment that is to be removed. The remaining regions (see Fig. 8.4(b)) indicate the presence of BVID but also the presence of a manufacturing flaw. For this reason, the next step is to select a final ROI by drawing a polygon around the identified damage location. This step is interactive and relies on indication of the points of a polygon around the ROI (Fig. 8.4(c)). After that, the pixels outside the ROI are removed. The resulting image after this step is binarised by the assignment of "ones" to the non-zero pixels in order to extract the ROI contour and calculate its surface area. To enable visual verification if the BVID region was extracted properly, the boundaries of the final ROI are displayed on the input C-Scan (Fig. 8.4(d)). Such a quantitative analysis of this C-Scan took only several (ca. 9) seconds, which mostly covered the step of ROI selection.

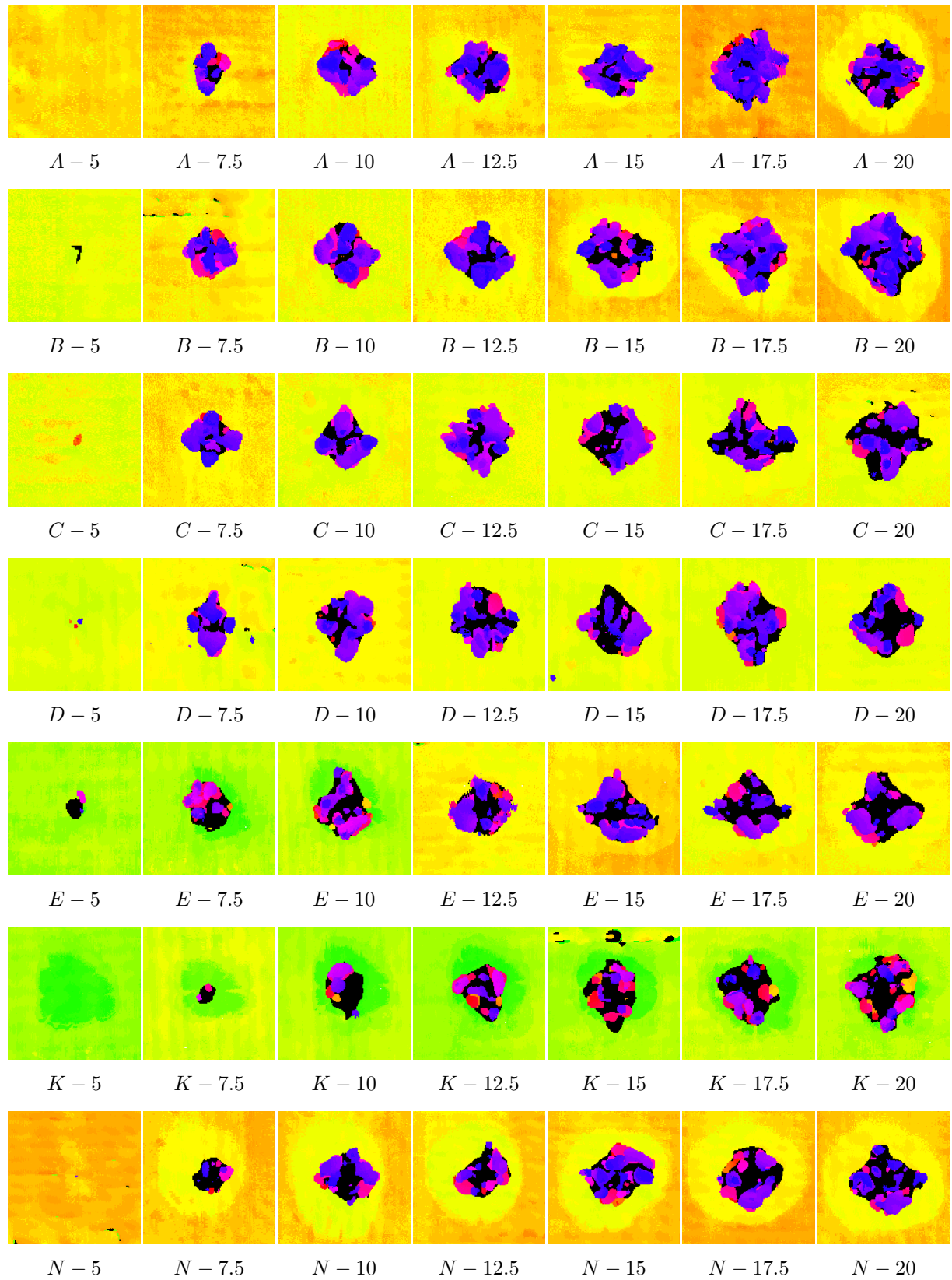


Fig. 8.3: Ultrasonic C-Scans of the impacted specimens (reduced to dimensions of 35×35 mm)

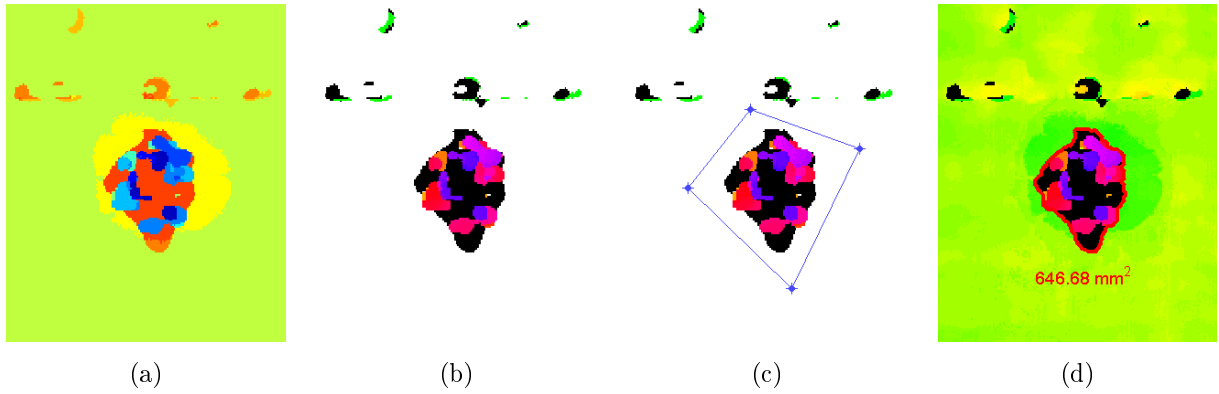


Fig. 8.4: Selected algorithm steps: image after segmentation (a), image after segments removal (b), ROI selection (c), input C-Scan with the BVID contour (d)

8.1.3 Results and discussion

All the obtained C-Scans were processed using the presented image analysis algorithm and a summary of the total area surfaces of the BVID is presented in Fig. 8.5.

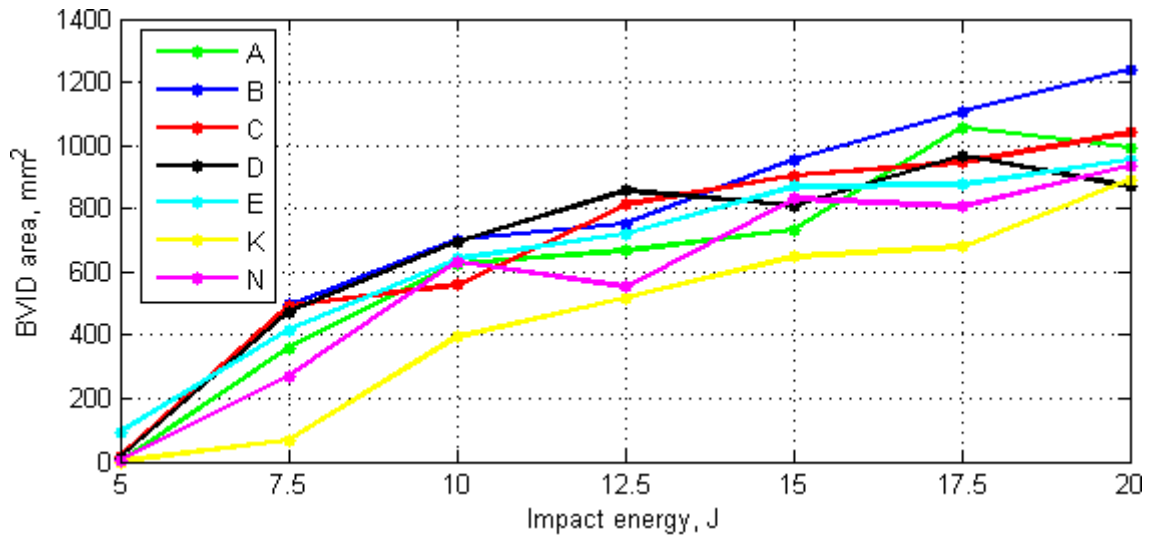


Fig. 8.5: Calculated BVID areas for the specimens impacted with variable energy values and impactor shapes (given in the legend of colours)

These results revealed that in the case of the impactors with the granite stones the more flat impactor *K* caused less damage for all the impact energy cases than the impactor *N* with the sharp ending. This is due to different types of stress distributions obtained when impacted with various shapes of impactor endings (flat solids cause mainly shear stress distribution whereas sharp shapes cause tension stress in the composite fibres and penetrates the matrix during the impact (Katunin, 2015c)). For the cases impacted with

the hemispherical impactors it can be noticed that the BVID produced by the impactor A is less than in the case of the impactor with a smaller radius B for all the impact energies, whereas for the rest impactors with the decreased radii no clear dependency is observable.

Having regard to the visual analysis of the specimens after introducing the low energy impact damage one can also observe that internal damage of the total surface area of even ca. 800 mm² might be completely invisible on the outer side of the structure.

8.1.4 Conclusions

The application of the proposed image analysis algorithm allowed for performing a very fast analysis and qualitative evaluation of impact damage in CFRP structures. The analysis of all the C-Scans that were loaded automatically from a selected computer folder took only about 10 minutes in total for the 49 considered BVID cases. It can be concluded that the proposed algorithm allows for the efficient damage evaluation and can be used for the analysis of numerous and/or large ultrasonic C-Scans. Moreover, the results demonstrated the necessity of the application of NDIs for the composite components since even large internal impact damage can be imperceptible when inspected visually.

8.2 Delamination size monitoring in CFRP aircraft elements

This section presents an approach to damage size monitoring based on C-Scans of aircraft structures and an extended version of the image analysis algorithm presented in the previous section. Additional image processing steps were introduced since the analysis of aircraft elements is difficult due to the complexity of the obtained C-Scans caused by the variable thickness and the presence of other elements, such as hatches, rivets and reinforcements. To test the algorithm, pairs of C-Scans of composite aircraft elements were used that were acquired during inspections carried out at time intervals. The proposed algorithm is based on two input C-Scans and enables the extraction of damage contours, preceded by indication of ROIs by the UT operator, and calculation of a change in the damage surface area as well as comparison of these contours. Initial results of research in this area were published in (Wronkiewicz and Dragan, 2016).

8.2.1 Structures and experiments

In this research stage, C-Scans of the CFRP composite panels used in military aircrafts, described previously in section 6.1 and presented in Fig. 6.1(b), were used. The ultrasonic inspections of these panels were performed using the MAUS[®] system and the Pulse-Echo method with a 5 MHz single transducer. To test the image analysis algorithm described in the next section, several pairs of C-Scans were used that were acquired during UT carried out in two-year inspection intervals during the aircrafts operation. The exemplary pair of C-Scans of a fragment of the aircraft panel is depicted in Fig. 8.6. In these pictures one can notice a delamination that was probably caused by over-tightening during assembly of a hatch as well as a delamination at a riveted joint.

8.2.2 Image analysis algorithm

The proposed algorithm is divided into two main stages: damage extraction and quantification (which is performed for both input C-Scans separately) and damage growth calculation and comparison (where the results of the first stage are analysed together). At first, a pair of C-Scan maps is loaded into the workspace. Then, both of them are individually subjected to the operations described below. Note that the demonstrative results of these steps are shown based on one of the input C-Scans that is presented in Fig. 8.6(a).

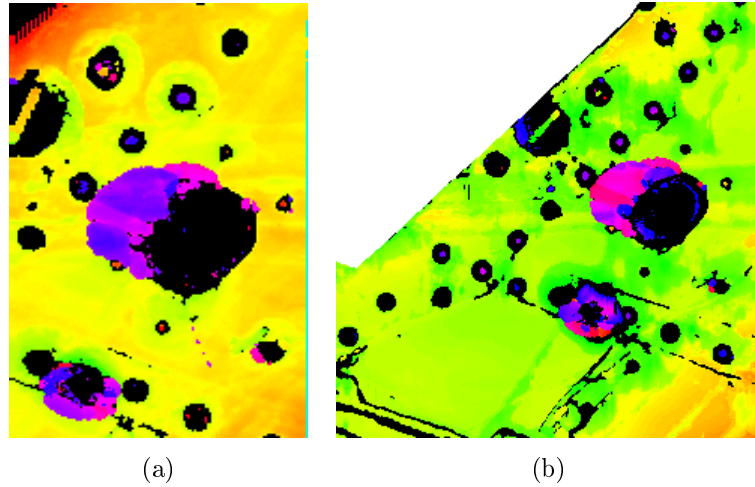


Fig. 8.6: Exemplary pair of C-Scans of a composite aircraft panel acquired during UT performed in an interval of two years

Firstly, the image is processed analogously to the algorithm described in section 8.1.2. Namely, the C-Scan is segmented using the MBP algorithm (see the result for the exemplary case presented in Fig. 8.7(a)). Then, segments of the healthy regions as well as the black-pixel areas (representing attenuation in the adhesive layer and areas of the panel after disassembly of the hatches and rivets visible in Fig. 6.1(b)) are removed from the image (see Fig. 8.7(b)). The next step is the ROI selection (Fig. 8.7(c)) in order to exclude the regions of the embedded elements in the structure (e.g. not removed rivets) or noise. In the presented case, the delamination around the hatch was considered as the ROI.

After that, additional processing is performed in order to clean possibly remaining pixels. Firstly, the fuzzy recursive flood fill with 8 directions algorithm is executed for each pixel belonging to the contour of the drawn polygon (ROI). This operation aims at removing possibly remaining areas being in contact with the ROI contour. It relies on reducing to zero the neighbouring pixels of values that are close to the source pixel (within a given threshold, e.g. ± 3). This enables removal of only the uniform areas intersected by the contour around ROI, while not interfering in the ROI itself, since replacing (cleaning) is stopped when encountering areas with a different value (colour). This operation is helpful in the cases when a damaged region is too close (or adjacent) to other regions left after the background removal, thus drawing a ROI polygon between them is difficult or impossible. Moreover, additional steps were added to ensure cleaning of small regions that could possibly remain after the flood filling. For this purpose, the resulting image is temporarily binarised in order to perform so-called morphological area opening. This operation enables removing all the connected components in a binary image that have fewer

than the specified number of pixels. The resulting image after these steps is presented in Fig. 8.7(d). Finally, boundaries of the resulting object (non-zero pixels) are extracted and its surface area is calculated. The resulting images with the extracted damage boundaries (in red) are presented in Fig. 8.8(a) and Fig. 8.8(b), respectively, for the exemplary pair of C-Scans.

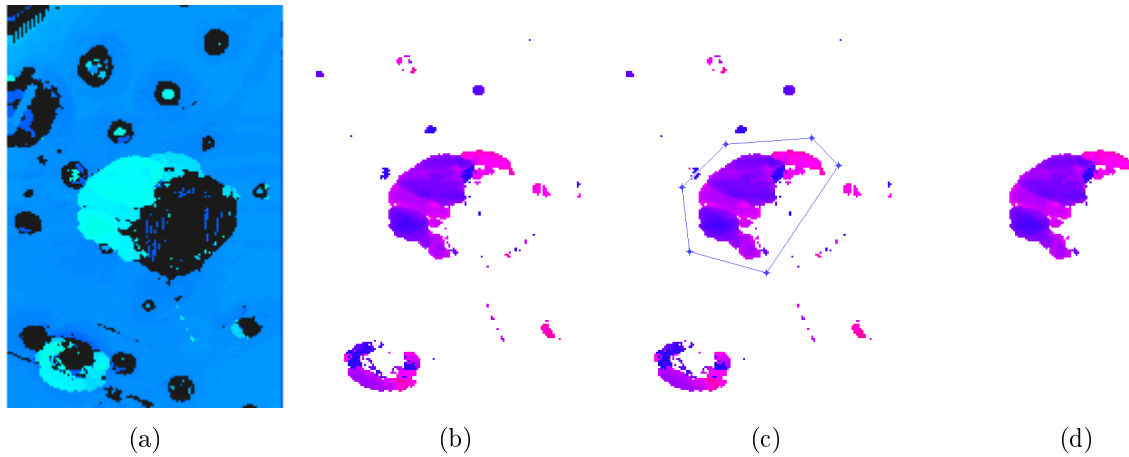


Fig. 8.7: Selected algorithm steps: image after segmentation (a), image after segments removal (b), ROI selection (c), extracted damage region (d)

The second stage of the algorithm includes calculating the difference between the damage areas in both C-Scans and superimposing both input C-Scans with the detected contours onto one figure (Fig. 8.8(c)) based on locations of the centroids of these contours.

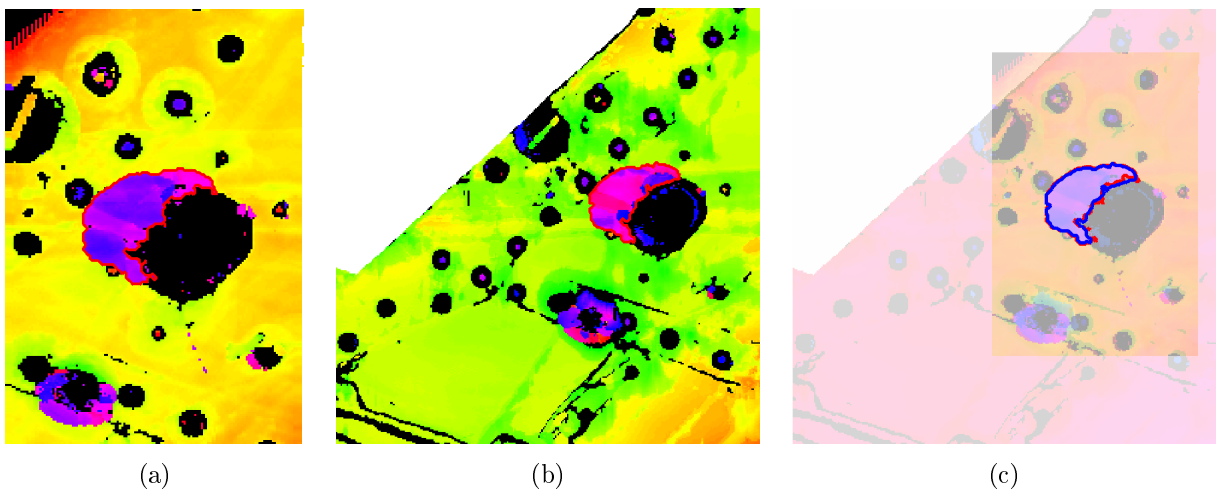


Fig. 8.8: Contours of the selected damage region: in the first C-Scan (a), in the second C-Scan (b), superimposed C-Scans and contours (c)

8.2.3 Results and discussion

The algorithm described above was tested on several pairs of C-Scans described earlier and the exemplary results are depicted in Fig. 8.9. A visual analysis of the results reveals that in all cases the contours of the delaminations were detected properly. The differences in the damage sizes were calculated as follow: 0.65 mm^2 , 7.15 mm^2 , 2.5 mm^2 for the cases presented in Fig. 8.9(a),(b), and (c), respectively, and -0.75 mm^2 for the demonstrative case presented in Fig. 8.8. In fact, obviously, damage size cannot decrease, thus the last of the mentioned results follows most likely from a measurement error. One should be aware that the rest results may also reveal certain measurement uncertainty, which is dependent on numerous factors that were widely discussed in chapter 4.1.

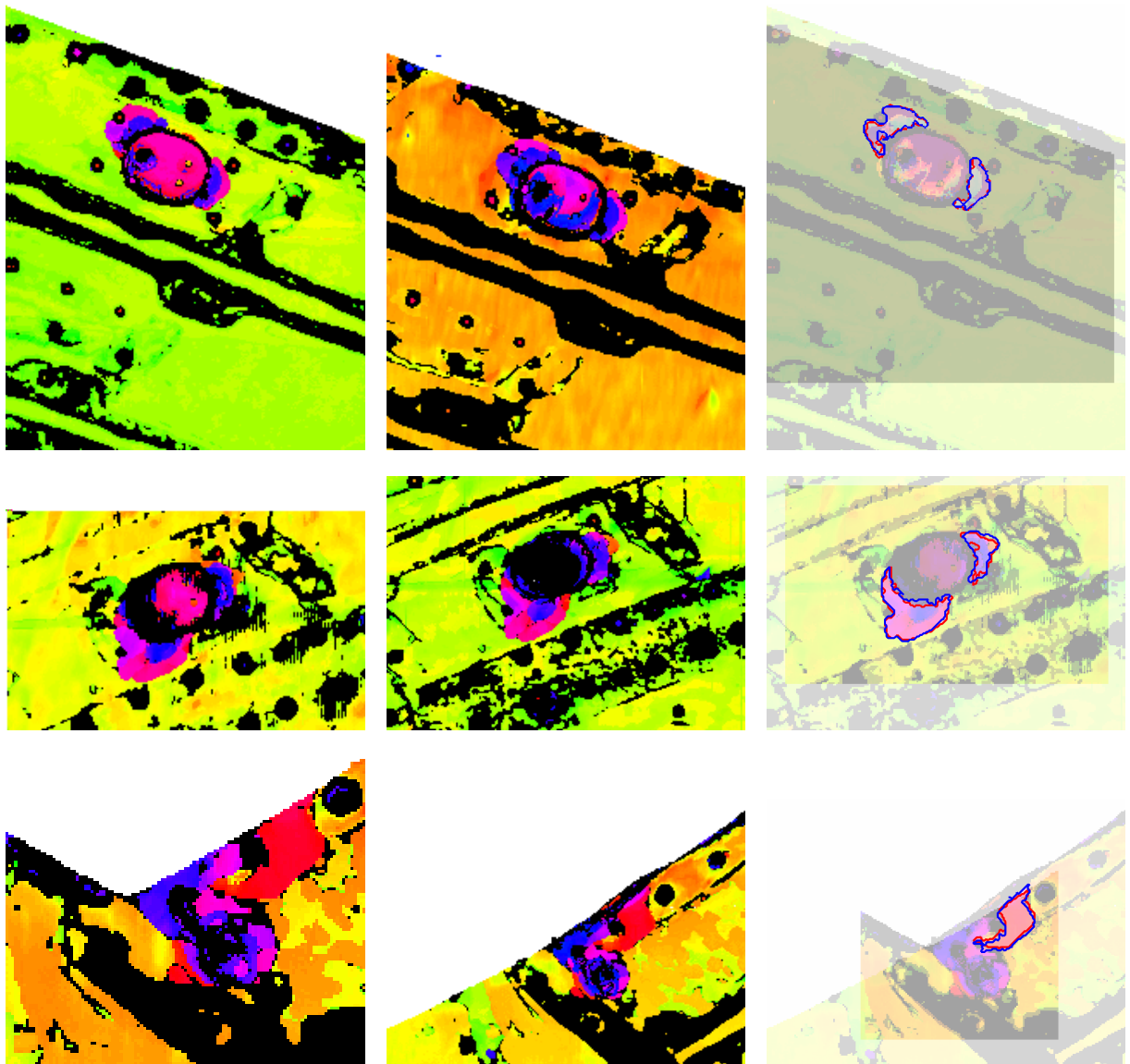


Fig. 8.9: Exemplary pairs of C-Scans and the damage extraction and comparison results

8.2.4 Conclusions

In this section, the approach to damage size monitoring of composite components based on UT with the C-Scan mode and the algorithm based on image analysis was presented. This algorithm was tested on several examples of pairs of C-Scans obtained approximately with two-year inspection intervals during the aircraft operation. The obtained results show that the proposed algorithm may be helpful in the damage evaluation procedures and the superimposing of two C-Scans with damage contours may facilitate the diagnostic inference process. In particular, this may help in the detection of the exact location of potential damage propagation. However, it is recalled that final interpretation of the UT data and the decision about an eventual repair is made by the UT expert based on his experience and requirements of the damage tolerance methodology.

8.3 3D damage reconstruction and visualisation in CFRP aircraft elements

The scope of the last research step was to test the proposed 3D damage reconstruction and visualisation algorithm on ultrasonic C-Scans with more complex nature than in the case of the specimen used in chapter 7. It is aimed at determining whether this algorithm could be potentially applied in practice to support the diagnostic procedures in the aircraft industry. Initial results of the tests presented in this section were published in (Wronkowicz *et al.*, 2015).

8.3.1 Structures and experiments

In this case study, C-Scan parts of the CFRP composite aircraft panel with delaminated areas, analysed in section 8.2, were used. As mentioned in the previous section, the ultrasonic inspection of this panel was performed using MAUS[®] system with a frequency of 5 MHz. For the purpose of the analysis presented here, three ToF C-Scan fragments with detected delaminated areas were extracted, which are shown in Fig. 8.10.

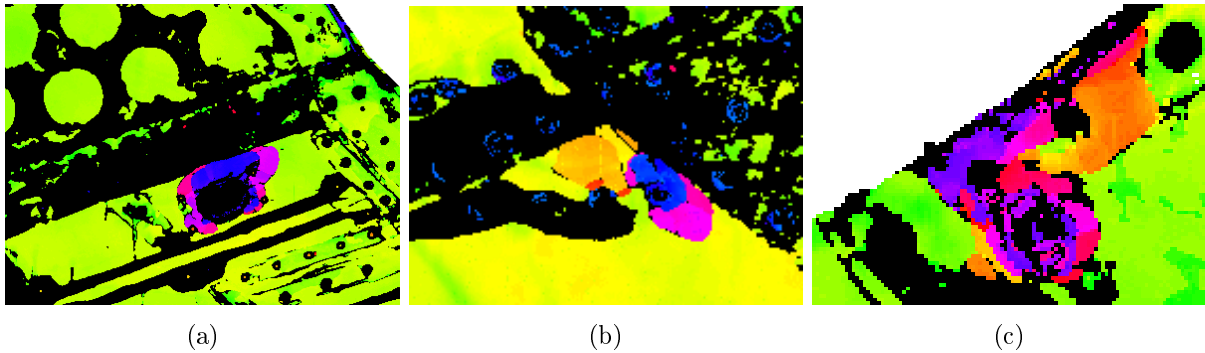


Fig. 8.10: Parts of the C-Scan of the aircraft panel with detected delaminations

8.3.2 Image analysis algorithm

As previously noted, C-Scans of real aircraft structures are characterised by the presence of not only the damaged regions and the background reflections but also, among others, the areas of riveted joints and stiffening ribs. Owing to this, it was noted that the 3D visualisation capabilities might be improved by appropriate showing the damage together with the background reflections. This could be useful in more precise damage localisation with respect to the internal structure of the aircraft panel. Thus, it was decided to extend the primary image processing algorithm presented in section 7.2 by the reconstruction of

both damage and background reflections and graphical representation of them together with different transparency parameters. Moreover, the step of interactive ROI selection should be added due to the complex construction of the considered aircraft elements.

A final form of the implemented image analysis algorithm is as follows. Similarly to the algorithm presented in section 7.2, the algorithm is divided into two main steps: damage extraction and 3D reconstruction with visualisation. The damage extraction step is initially performed using the MBP-based image segmentation algorithm. The exemplary result for the raw C-Scan depicted in Fig. 8.10(a) is presented in Fig. 8.11(a). After that, the additional step of the interactive selection of final ROI is done analogously to the algorithm presented in sections 8.1 and 8.2. This allows removing unwanted regions that are outside the selected polygon (see Fig. 8.11(b–c)). Afterwards, damage contour is extracted and its geometrical properties are calculated. Optionally, the resulting image can be binarized and the morphological area opening performed to remove noise, e.g. single pixels.

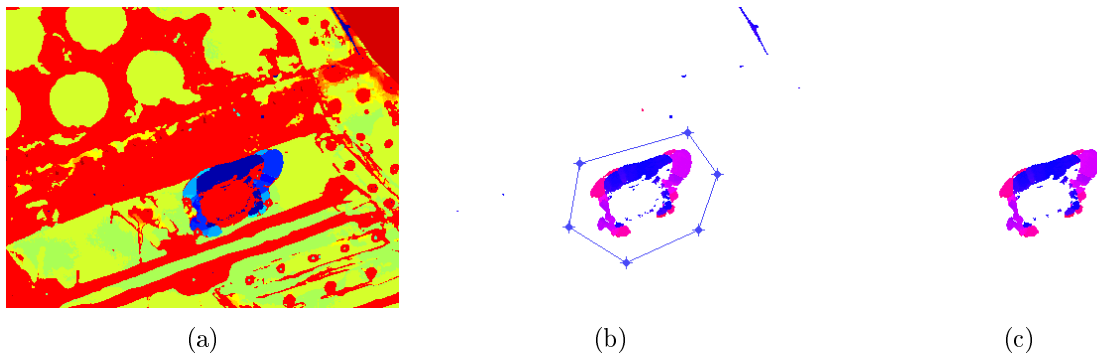


Fig. 8.11: Selected steps of the algorithm: image after segmentation (a), ROI selection (b), extracted damage region (c)

The major difference lies in the second step of the algorithm where not only the extracted damage but also the background reflections are reconstructed from 2D to 3D matrices. The 3D reconstruction itself is performed analogously to the approach described in section 7.2. The last operation relies on volume rendering by semi-transparent displaying of both matrices but with exposed damage regions. This was achieved by multiple dividing the values of the matrix containing the background data, which resulted in displaying it in unique and uniform colour ranges. A selected 3D view obtained for the considered part of the C-Scan is presented in Fig. 8.12(a).

8.3.3 Results and discussion

The algorithm described in section 8.3.2 was tested based on the three presented C-Scan parts. Exemplary views of the obtained 3D damage visualisations are presented in Fig. 8.12. The calculated total surface areas of the detected delaminations are 32.07 mm^2 , 15.87 mm^2 , and 16.52 mm^2 , respectively to a sequence of the input C-Scans presented in Fig. 8.10. The surface areas can be also calculated as well as visualised separately for each delamination laying at particular depth of the tested element.

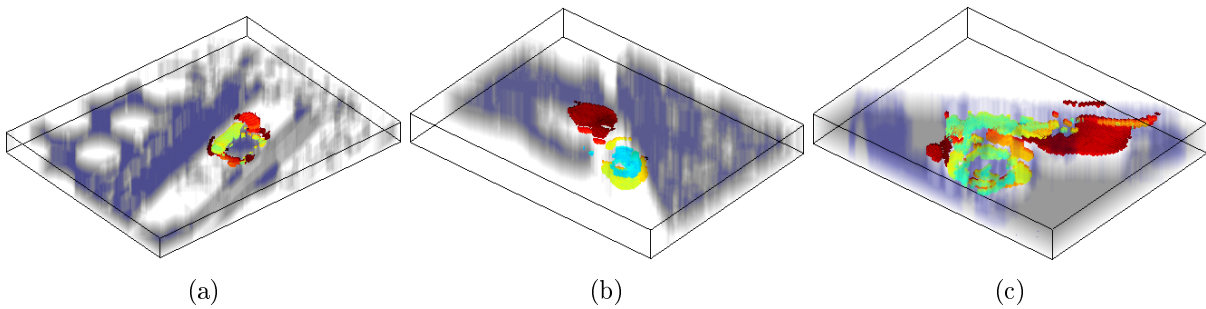


Fig. 8.12: 3D visualisation of damage sites with backgrounds of the tested aircraft panel

When analysed the obtained results one can conclude that the proposed visualisation approach is suitable for analysing composite elements utilised in practice such as aircraft panels. The damage regions are very well noticeable and, additionally, their position with respect to other elements inside the tested object can easily be determined in all three axes. It is supposed that such a form of data displaying during ultrasonic inspections could be a useful tool to support UT operators. For example, distribution of the damage and its directionality as well as 3D shape may help in inferencing about potential damage root cause. However, it should be kept in mind that the C-Scan-based reconstruction does not give complete information about damage and tested structure architecture.

8.3.4 Conclusions

In this section, usefulness of the proposed 3D reconstruction and visualisation algorithm was tested based on data obtained during ultrasonic inspection of the aircraft element. Based on the ultrasonic attenuation levels, the 3D graphical representation of damage sites was performed, which allows observing the damage extent at particular layers of the composite structure within the thickness range. It was found out that the use of such a tool may simplify interpretation of C-Scan images. Moreover, obtaining 3D matrices with damage data as well as background data allows not only for their 3D graphical representation but also analysis of particular areas by any data manipulation in three axes.

This allows for easier evaluation of the damage shape and extent considering its distribution at various depth locations. The 3D array was reconstructed from planar projections of damage sites in a form of C-Scans, thus, the potential damage sites located beyond another ones are masked which is a disadvantage of this approach. Thus, as mentioned before, using B-Scans (if available) for the reconstruction purpose is more recommended. However, beyond this limitation, the proposed approach is computationally efficient and can be a useful (additional) tool for UT operators.

9. Summary conclusions

9.1 Conclusions

The presented thesis is the result of the performed studies connected with the application of image analysis methods aimed at supporting ultrasonic inspections of composite aircraft elements. This research was undertaken due to the practical problem occurring during the analysis of ultrasonic data, resulting mainly from large sizes of the obtained data and the necessity of manual handling of them (processing and annotating). Another problem is a lack of universal and comprehensive tools for aiding the UT data analysis as well as lack of knowledge about the accuracy of the existing solutions. This prompted the author to formulating the presented objectives and setting the hypothesis connected with the assumed possibility of increasing efficiency and reliability of diagnostics of composite aircraft elements based on ultrasonic testing. The research stages completed within the frames of this thesis include the elaboration of the literature survey on the existing solutions and studies of other researchers in this area and carrying out of several experimental studies with the use of the specimens as well as aircraft structures made of CFRP composites with common types of internal damage. Three main aspects of ultrasonic inspections and data analysis were investigated: damage detection, evaluation, and visualisation. Conclusions made after accomplishing particular experiments are summarised below.

Firstly, measurement uncertainty factors in damage detection and evaluation were analysed. In order to determine possible measurement errors that can be obtained during UT of the type and geometrical properties of the structures tested in this research, the experiments with the use of the specimens with FBHs of known dimensions were performed. This allowed for the determination of the influence of the selected UT technique and testing parameters on the damage detectability and the selection of the most suitable sets of UT parameters for further experiments. From the qualitative and quantitative analyses of the obtained results it was concluded that for the considered variables – the lowest measurement errors of the considered diameters and depth locations were obtained when tested with a frequency of 5 MHz and 10 MHz, both with the peak filtered RF display mode. Due to the specimen thinness (2.5 mm), the delay line was applied when tested with the Pulse-Echo testing, which improved the near-surface resolution and allowed for

the detection of all FBHs, i.e. located at the depths of 0.25–2.25 mm. In the case of the Phased Array testing, not all the FBHs were detected. It was also observed that most diameters were over-sized for the Pulse-Echo testing whereas for the Phased Array testing they were mostly under-sized.

Secondly, the methods of post-processing of ultrasonic data were analysed in the context of their accuracy for the damage detecting purposes. The analysis of the performed literature survey and own experience allowed concluding that the key aspect in damage detection from ToF C-Scans is proper image segmentation, i.e. data reduction, which allows for a quicker and easier separation of damage from background ultrasonic reflections. The comparative analysis of the damage detection accuracy using various image segmentation methods was accomplished based on C-Scans of the specimen with BVID and the aircraft panel with delamination, which provided different degrees of data complexity. Based on the initial qualitative analysis of the obtained results, several bi-modal threshold-based and edge-based segmentation methods were excluded from further consideration. The quantitative analysis of the rest (clustering-based and region-based) approaches indicated high impact of the selected input parameters on the results, which makes them not universal. The necessity of the selection of the input parameters and/or long computation duration are the major drawbacks of many from the tested methods. The best accuracy and versatility results were obtained for the proposed non-parametric segmentation approaches based on the detection of local minima of the image histogram and additional image processing operations. No necessity of the selection of parameters and very high computational performance are the other advantages of this approach. This allowed making the conclusion that this approach is suitable for the considered application and will be used in further research stages.

The next research stage concerned the analysis and experiments connected with the 3D reconstruction and visualisation of damage based on planar ultrasonic scans. Different image processing algorithms were proposed for the damage reconstruction based on a C-Scan and based on a series of B-Scans acquired during testing of the specimen with BVID. The results of the 3D reconstruction were evaluated qualitatively by comparing it with the reference data obtained by the BVID reconstruction from the data acquired with the X-ray CT method. A good convergence was observed between the the characteristics of damage areas reconstructed from the ultrasonic scans and X-ray CT data. Only some delaminated regions located directly below the top surface of the specimen, which were noticeable in the X-ray CT-based visualisation, could not be observed in the UT-based reconstructed view due to their position in the ultrasonic transducer dead zone during UT. Naturally, data extracted from the B-Scans resulted in a much more complete visual-

isation of particular delaminations shapes and locations than in the case of the extraction from the C-Scan. This is related to the way of C-Scans formation, which is done by extracting limited information from all B-Scans acquired during UT. Nevertheless, for both cases the obtained results allowed concluding that such a 3D visualisation is more informative than raw ultrasonic data and it may facilitate the diagnostic inference procedure and provide an additional support for UT operators.

Finally, the developed image analysis algorithms, or their extended versions, were tested based on three case studies. The first case study covered the investigation on damage in considered CFRP composites caused by low energy impacts. Various damage configurations were introduced to the specimens using different impact energies and shapes of impactors. The dependency between the impact parameters and visibility of the resulting damage on the outer surface of the specimens and the total area extent of the internal damage was analysed. The application of the proposed image analysis algorithm, extended by several additional operations, allowed for a very quick analysis of all the 49 obtained C-Scans, i.e. damage extraction and calculation of its surface area. The observations made indicated that flat-shaped impactors caused less damage than the sharp-ended impactors, which is due to different types of occurred stress distributions. The impacts of the energy in the range of 15–20 J caused BVID with little signs of damage visible on the outer sides of the specimens, whereas mostly no external signs could be noticed when impacted with the energy in the range of 5–12.5 J. This demonstrated the need of performing NDIs enabling the detection of internal damage since even large delaminations can be invisible when inspected just visually.

The second case study was dedicated to delamination size monitoring based on pairs of C-Scans of aircraft elements acquired during ultrasonic inspections performed with a two-year interval. The proposed image analysis algorithm allowed for quick extraction of damage and its contour, calculation of its size based on both C-Scans, and calculation of a change in the damage surface area as well as visual comparison of these contours. Additionally, both C-Scans and damage contours were merged and displayed in one figure, which may facilitate the detection of the precise location of damage propagation.

The last case study included 3D reconstruction of C-Scans of the composite aircraft panel. The described earlier image processing algorithm for this purpose was extended by the visualisation of damage together with the background with appropriate volume rendering so that damage was more emphasized. This modification allowed for more precise damage localisation with respect to internal architecture of the tested element, e.g. hatches or particular rivets. Moreover, arbitrary data manipulation in three axes is possible, which allows for easier evaluation of the damage shape and distribution at various

depth locations.

Quoting the formulated hypothesis it can be stated that the results of the accomplished research studies allowed confirming that *it is possible to increase efficiency and reliability of diagnostics of composite aircraft elements based on ultrasonic testing by the development of a methodology with the use of image processing and analysis methods.*

9.2 Further work

The analysis of the obtained results allowed for noticing several new areas of further development of the presented research studies. The most relevant of them are listed below.

- The results of the analysis of the measurement uncertainty could be improved by testing the specimens with more types, locations and orientations of flaws and damage. In particular, flaws/damage that are not perpendicular to the scanning direction could be analysed.
- The damage extraction procedures based on ToF C-Scans can be further improved by an application of new methods of image segmentation as well as other image or signal processing operations.
- The other noticed perspective of an improvement of the presented research results in this thesis resulted in the currently started grant no. 2017/25/N/ST8/01009 entitled: "Methodology of prediction of residual strength of composite structures based on ultrasonic testing supported by numerical modelling", financed by the National Science Centre (Poland). One of the grant research steps aims at further development of the presented 3D damage reconstruction approaches as well as the development of a method enabling 3D fusion of the UT-based reconstructed data and X-ray CT data for the purpose of enhanced visual and quantitative verification of the reconstruction. The obtained 3D shape of the damage will be used as an input to prepare a finite element model of the structure with existing damage. Such a model will be used as an input to numerical modelling for predicting the residual strength of the tested element.

Bibliography

- Aero Consultants AG (n.a.): Vacuum Bagging and Composite Tooling. Accessed: 2017-01-22.
URL: <http://www.aero-consultants.ch/en/Airtech-Hilfsmaterialien/Vacuum-Bagging-and-Composite-Tooling.htm>
- Ballard D. H. (1981): *Generalizing the Hough transform to detect arbitrary shapes*. Pattern recognition **13**(2): pp. 111–122.
- Barrett J. F. and Keat N. (2004): *Artifacts in CT: recognition and avoidance*. Radio-Graphics **24**(6): pp. 1679–1691.
- Berke M. (1996): *Nondestructive Material Testing with Ultrasonics: Introduction to the Basic Principles*. Krautkammer GmbH & Company.
- Bernsen J. (1986): *Dynamic thresholding of grey-level images*. Proc. of the 8th Int. Conf. on Pattern Recognition: pp. 1251–1255.
- Beucher S. and Lantuéjoul C. (1979): *Use of watersheds in contour detection*. Proc. International Workshop on Image Processing: Real-time Edge and Motion Detection/Estimation. Rennes, France.
- Bezdek J. C., Ehrlich R. and Full W. (1984): *FCM: The fuzzy c-means clustering algorithm*. Computers & Geosciences **10**(2): pp. 191–203.
- Bhanu B. and Lee S. (2012): *Genetic learning for adaptive image segmentation*. Vol. 287. Springer Science & Business Media.
- Bhardwaj S. and Mittal A. (2012): *A Survey on Various Edge Detector Techniques*. Procedia Technology **4**(Supplement C): pp. 220–226. 2nd International Conference on Computer, Communication, Control and Information Technology(C3IT-2012) on February 25 - 26, 2012.
- Birt E. A. and Smith R. A. (2004): *A review of NDE methods for porosity measurement in fibre-reinforced polymer composites*. Insight **46**(11): pp. 681–686.
- Boeing 787 Specs (n.a.): Accessed: 2017-01-30.
URL: <http://www.modernaairliners.com/boeing-787-dreamliner/boeing-787-dreamliner-specs/>

- Boller C. and Staszewski W. J. (2004): Aircraft Structural Health and Usage Monitoring. In: Health monitoring of aerospace structures: smart sensor technologies and signal processing, W. J. Staszewski, C. Boller and G. R. Tomlinson (Eds). John Wiley & Sons.
- Bouvet C. and Rivallant S. (2016): Damage tolerance of composite structures under low-velocity impact. Dynamic Deformation, Damage and Fracture in Composite Materials and Structures. Woodhead Publishing: pp. 7–33.
- Bowkett M. and Thanapalan K. (2017): *Comparative analysis of failure detection methods of composites materials' systems*. Systems Science & Control Engineering **5**(1): pp. 168–177.
- Bozzi E., Cavaccini G., Chimenti M., Di Bono M. and Salvetti O. (2007): *Defect detection in C-scan maps*. Pattern Recognition and Image Analysis **17**(4): pp. 545–553.
- Bradley D. and Roth G. (2007): *Adaptive thresholding using the integral image*. Journal of Graphics Tools **12**(2): pp. 13–21.
- Broughton W. R., Lodeiro M. J., Sims G. D., Zeqiri B., Hodnett M., Smith R. A. and Jones L. D. (1999): *Standardised procedures for ultrasonic inspection of polymer matrix composites*. ICCM 12th Conf. Composite Mater.. Paris.
- Brunelli R. (2009): *Template matching techniques in computer vision: theory and practice*. John Wiley & Sons.
- Cempel C., Tomaszewski F. and Leszek W. (1992): *Diagnostyka maszyn: zasady ogólne: przykłady zastosowań*. Międzynarodowe Centrum Naukowe Eksploatacji Majątku Trwałego. Radom.
- Chaki N., Shaikh S. H. and Saeed K. (2014): *Exploring image binarization techniques*. Studies in Computational Intelligence. Springer.
- Chen W.-T., Wen C.-H. and Yang C.-W. (1994): *A fast two-dimensional entropic thresholding algorithm*. Pattern Recognition **27**(7): pp. 885–893.
- Cholewa W. and Moczulski W. (1995): *Diagnostyka techniczna maszyn: pomiary i analiza sygnałów*. Wydawnictwo Politechniki Śląskiej. Gliwice.
- Civil Aviation Authority (2010): *Civil Aircraft Inspection Procedures: Part I – Basic*. Himalayan Books. New Delhi, India.
- Corneloup G., Moysan J. and Magnin I. E. (1996): *Bscan image segmentation by thresholding using cooccurrence matrix analysis*. Pattern Recognition **29**(2): pp. 281–296.
- Cornwell I. and McNab A. (1999): *Towards automated interpretation of ultrasonic NDT data*. NDT & E International **32**(2): pp. 101–107.

- Cot L. D., Bes C. and Gogu C. (2013): *Structural airframe maintenance strategy comparison: a new approach*. In: Structural Health Monitoring 2013: A Roadmap to Intelligent Structures: Proceedings of the Ninth International Workshop on Structural Health Monitoring, F.-K. Chang (Ed.). DEStech Publications, Inc: pp. 1460–1467.
- Crompton M. (2014): *Ultrasonic bond testing as a quality tool: with the growth in the use of adhesive bonding and composites, bond testing is seeing its second wind*. Quality **53**(7): pp. S4–S4.
- Davis J. R. (1989): *ASM Handbook: Nondestructive Evaluation and Quality Control*. Vol. 17. ASM International. Materials Park, OH.
- De S., Bhattacharyya S., Chakraborty S. and Dutta P. (2016): *Hybrid Soft Computing for Multilevel Image and Data Segmentation*. Computational Intelligence Methods and Applications. Springer. chapter 2 – Image Segmentation: A Review.
- Dempster A. P., Laird N. M. and Rubin D. B. (1977): *Maximum likelihood from incomplete data via the EM algorithm*. Journal of the royal statistical society. Series B (methodological) : pp1–38.
- Divya H. V., Naik L. and Yogesha B. (2016): *Processing Techniques of Polymer Matrix Composites – A Review*. International Journal of Engineering Research and General Science **4**(3): pp. 357–362.
- Donadon M. V., Iannucci L., Falzon B. G., Hodgkinson J. M. and de Almeida S. F. M. (2008): *A progressive failure model for composite laminates subjected to low velocity impact damage*. Computers & Structures **86**(11): pp. 1232–1252.
- Dragan K. (2011): *Image Processing approach for the Non Destructive Evaluation (NDE) of the composite materials as the input to structural durability assessment*. Technical News **1**: pp. 49–52.
- Dragan K. and Synaszko P. (2009): *In-service flaw detection and quantification in the composite structures of aircraft*. Fatigue of Aircraft Structures **1** (2009)(1): pp. 37–41.
- Dragan K., Bieniaś J., Leski A., Czulak A. and Hufenbach W. (2012a): *Inspection methods for quality control of fibre metal laminates (FML) in the aerospace components*. Composites Theory and Practice **12**(4): pp. 272–278.
- Dragan K., Dziendzikowski M., Kurnyta A., Sałacinski M., Kłysz S. and Leski A. (2015): *Composite Aerospace Structure Monitoring with use of Integrated Sensors*. Fatigue of Aircraft Structures **1** (2015)(7): pp. 12–17.

- Dragan K., Stefaniuk M. and Synaszko P. (2012b): *Numerical approach for ultrasonic imagining of defects in composites*. Composites Theory and Practice **12**(2): pp. 105–109.
- Dragan K., Stefaniuk M., Czulak A., Bieniaś J., Dziendzikowski M., Leski A., Gude M. and Hufenbach W. (2013): *Automated data analysis based on signal processing for two dimensional NDI data of the composite structures*. Przetwórstwo Tworzyw **19**(1 (151)): pp. 4–8.
- Duda R. O. and Hart P. E. (1972): *Use of the Hough transformation to detect lines and curves in pictures*. Communications of the ACM **15**(1): pp. 11–15.
- Dunn J. C. (1973): *A fuzzy relative of the ISODATA process and its use in detecting compact well-separated clusters*. Journal of Cybernetics **3**(3): pp. 32–57.
- DuPont (n.a.): Honeycomb Composite Made Lighter and Stronger. Accessed: 2018-03-10.
URL: <http://www.dupont.com/products-and-services/fabrics-fibers-nonwovens/fibers/uses-and-applications/honeycomb-composites.html>
- Ehrhart B., Valeske B. and Bockenheimer C. (2013): 9 - Non-destructive evaluation (NDE) of aerospace composites: methods for testing adhesively bonded composites. In: Non-Destructive Evaluation (NDE) of Polymer Matrix Composites, V. M. Karbhari (Ed.). Woodhead Publishing Series in Composites Science and Engineering. Woodhead Publishing: pp. 220–237.
- Farrar C. R. and Worden K. (2007): *An introduction to structural health monitoring*. Philosophical Transactions of the Royal Society of London A: Mathematical, Physical and Engineering Sciences **365**(1851): pp. 303–315.
- Federal Aviation Administration (2008): *Aviation Maintenance Technician Handbook: General*. U.S. Department of Transportation. Oklahoma City, Oklahoma, US.
- Federal Aviation Administration (2012a): Advanced Composite Materials. Aviation Maintenance Technician Handbook–Airframe. Vol. 1. U.S. Department of Transportation.
URL: https://www.faa.gov/regulations_policies/handbooks_manuals/aircraft/amt_airframe_handbook/media/ama_Ch07.pdf
- Federal Aviation Administration (2012b): Aircraft Structures. Aviation Maintenance Technician Handbook–Airframe. Vol. 1. U.S. Department of Transportation.
URL: https://www.faa.gov/regulations_policies/handbooks_manuals/aircraft/amt_airframe_handbook/media/ama_ch01.pdf
- Feng M.-L. and Tan Y.-P. (2004): *Contrast adaptive binarization of low quality document images*. IEICE Electronics Express **1**(16): pp. 501–506.

- Finch R., Fischer R., Grimes M., Stits R. and Watkins W. (n.a.): Advisory Circular 43.13-1B – Acceptable Methods, Techniques, and Practices – Aircraft Inspection and Repair.
URL: https://www.faa.gov/regulations_policies/advisory_circulars/index.cfm/go/document.information/documentID/99861
- Fowler T. J., Kinra V. K., Maslov K. and Moon T. J. (2001): *Research Report: Inspecting FRP Composite Structures with Nondestructive Testing. Technical Report FHWA/TX-03/1892-1*. Center for Transportation Research, The University of Texas at Austin.
- Francis D. (2013): 4 - Non-destructive evaluation (NDE) of composites: introduction to shearography. In: Non-Destructive Evaluation (NDE) of Polymer Matrix Composites, V. M. Karbhari (Ed.). Woodhead Publishing Series in Composites Science and Engineering. Woodhead Publishing: pp. 56–83.
- Fu K.-S. and Mui J. (1981): *A survey on image segmentation*. Pattern recognition **13**(1): pp. 3–16.
- Fu Z. and Wang L. (2012): Color image segmentation using gaussian mixture model and EM algorithm. Multimedia and Signal Processing. Springer: pp. 61–66.
- Fukunaga K. and Hostetler L. (1975): *The estimation of the gradient of a density function, with applications in pattern recognition*. IEEE Transactions on Information Theory **21**(1): pp. 32–40.
- Gamstedt E. K. and Sjögren B. A. (1999): *Micromechanisms in tension-compression fatigue of composite laminates containing transverse plies*. Composites Science and Technology **59**(2): pp. 167–178.
- Gaylord M. W. (1974): *Reinforced Plastics: Theory and Practice*. 2nd edn. Cahnerns Books.
- Gdoutos E. E. (2005): *Fracture Mechanics: An Introduction*. Vol. 123 of *Solid Mechanics and Its Applications*. 2nd edn. Springer Netherlands.
- Ghasemnejad H., Soroush V. R., Mason P. J. and Weager B. (2012): *To improve impact damage response of single and multi-delaminated FRP composites using natural Flax yarn*. Materials & Design (1980-2015) **36**: pp. 865–873. Sustainable Materials, Design and Applications.
- Giurgiutiu V. (2016): *Structural Health Monitoring of Aerospace Composites*. Academic Press.
- Glasbey C. A. (1993): *An analysis of histogram-based thresholding algorithms*. CVGIP: Graphical models and image processing **55**(6): pp. 532–537.

- Hale J. (2006): *Boeing 787 from the Ground Up*. AERO Magazine (4): pp. 17–23.
- Haralick R. M. and Shapiro L. G. (1985): *Image segmentation techniques*. Computer Vision, Graphics, and Image Processing **29**(1): pp. 100–132.
- Harrison R. P. and Bader M. G. (1983): *Damage development in CFRP laminates under monotonic and cyclic stressing*. Fibre Science and Technology **18**(3): pp. 163–180.
- Hartigan J. A. and Wong M. A. (1979): *Algorithm AS 136: A k-means clustering algorithm*. Journal of the Royal Statistical Society. Series C (Applied Statistics) **28**(1): pp. 100–108.
- Hasiotis T., Badogiannis E. and Tsouvalis N. G. (2011): *Application of ultrasonic C-scan techniques for tracing defects in laminated composite materials*. Strojniški vestnik-Journal of Mechanical Engineering **57**(3): pp. 192–203.
- Heida J. H. and Platenkamp D. J. (2011): *Evaluation of non-destructive inspection methods for composite aerospace structures*. Proc. of the International Workshop of NDT Experts. Prague: pp. 1–12.
- Heuer H., Schulze M. H. and Meyendorf N. (2013): 3 – Non-destructive evaluation (NDE) of composites: eddy current techniques. In: Non-Destructive Evaluation (NDE) of Polymer Matrix Composites, V. M. Karbhari (Ed.). Woodhead Publishing Series in Composites Science and Engineering. Woodhead Publishing: pp. 33–55.
- Hoa S. V. (2009): *Principles of the Manufacturing of Composite Materials*. Destech Publications, Inc.
- Holloway P. (2015): The shortcomings of the 6dB drop method for ultrasonic flaw length sizing.
URL: <https://www.linkedin.com/pulse/shortcomings-6db-drop-method-ultrasonic-flaw-length-sizing-holloway>
- Hough P. V. C. (1962): Method and means for recognizing complex patterns. US Patent 3069654.
- Hsu D. K. (2013): 15 – Non-destructive evaluation (NDE) of aerospace composites: ultrasonic techniques. In: Non-Destructive Evaluation (NDE) of Polymer Matrix Composites, V. M. Karbhari (Ed.). Woodhead Publishing Series in Composites Science and Engineering. Woodhead Publishing: pp. 397–422.
- Huang J. Q. (2013): 2 – Non-destructive evaluation (NDE) of composites: acoustic emission (AE). In: Non-Destructive Evaluation (NDE) of Polymer Matrix Composites, V. M. Karbhari (Ed.). Woodhead Publishing Series in Composites Science and Engineering. Woodhead Publishing: pp. 12–32.

- Hung Y. Y., Yang L. X. and Huang Y. H. (2013): 5 – Non-destructive evaluation (NDE) of composites: digital shearography. In: *Non-Destructive Evaluation (NDE) of Polymer Matrix Composites*, V. M. Karbhari (Ed.). Woodhead Publishing Series in Composites Science and Engineering. Woodhead Publishing: pp. 84–115.
- Jain A. K. and Dubuisson M.-P. (1992): *Segmentation of X-ray and C-scan images of fiber reinforced composite materials*. Pattern Recognition **25**(3): pp. 257–270.
- Kapur J., Sahoo P. and Wong A. (1985): *A new method for gray-level picture thresholding using the entropy of the histogram*. Computer Vision, Graphics, and Image Processing **29**(3): pp. 273–285.
- Karbhari V. M. (2013): 1 – Introduction: the future of non-destructive evaluation (NDE) and structural health monitoring (SHM). In: *Non-Destructive Evaluation (NDE) of Polymer Matrix Composites*, V. M. Karbhari (Ed.). Woodhead Publishing Series in Composites Science and Engineering. Woodhead Publishing: pp. 3–11.
- Kastner J., Plank B., Reh A., Salaberger D. and Heinzl C. (2013): *Advanced X-Ray Tomographic Methods for Quantitative Characterisation of Carbon Fibre Reinforced Polymers*. Proc. 4th International Symposium on NDT in Aerospace. Augsburg: pp. 1–9.
- Katunin A. (2015a): *Diagnostics of composite structures using wavelets*. Monographic series "Library of Maintenance Problems" no. 2540. The Publishing House of the Institute for Sustainable Technologies – National Research Institute. Radom.
- Katunin A. (2015b): *Impact damage assessment in composite structures based on multi-wavelet analysis of modal shapes*. Indian Journal of Engineering and Materials Sciences **22**: pp. 451–459.
- Katunin A. (2015c): *Stone impact damage identification in composite plates using modal data and quincunx wavelet analysis*. Archives of Civil and Mechanical Engineering **15**(1): pp. 251–261.
- Kefali A., Sari T. and Bahi H. (2014): *Text/Background separation in the degraded document images by combining several thresholding techniques*. WSEAS transactions on signal processing **10**: pp. 436–443.
- Kessler S. S., Spearing S. M., Atalla M. J., Cesnik C. E. S. and Soutis C. (2002): *Damage detection in composite materials using frequency response methods*. Composites Part B: Engineering **33**(1): pp. 87–95.
- Khurshid K., Siddiqi I., Faure C. and Vincent N. (2009): *Comparison of Niblack inspired binarization methods for ancient documents*. Document Recognition and Retrieval XVI **7247**: pp. 1–10.

- Kittler J. and Illingworth J. (1985): *On threshold selection using clustering criteria*. IEEE Transactions on Systems, Man, and Cybernetics (5): pp. 652–655.
- Kjelgaard C. (2012): *Challenges in composites*. Aircraft Technology (116): pp. 52–57.
- Konieczny J. (2013): *Materiały stosowane w konstrukcjach lotnictwa wojskowego*. Armia 4(56): pp. 68–75.
- Korbicz J., Kościelny J. M., Kowalczyk Z. and Cholewa W. (2002): *Diagnostyka procesów. Modele. Metody sztucznej inteligencji. Zastosowania*. Monografie – Komitet Automatyki i Robotyki Polskiej Akademii Nauk. Wydawnictwa Naukowo-Techniczne. Warszawa.
- Kotropoulos C., Magnisalis X., Pitas I. and Strintzis M. G. (1994): *Nonlinear ultrasonic image processing based on signal-adaptive filters and self-organizing neural networks*. IEEE Transactions on Image Processing 3(1): pp. 65–77.
- Kumar M. J., Kumar D. G. R. and Reddy R. V. K. (2014): *Review on image segmentation techniques*. International Journal of Scientific Research Engineering & Technology : pp2278–0882.
- Kurnyta A., Dziendzikowski M., Dragan K. and Kłysz S. (2016): Monitorowanie rozwoju uszkodzeń w elementach konstrukcji lotniczych. Problemy Badań i Eksploatacji Techniki Lotniczej. Instytut Techniczny Wojsk Lotniczych: pp. 49–62.
- Ley O. and Godinez V. (2013): 12 – Non-destructive evaluation (NDE) of aerospace composites: application of infrared (IR) thermography. In: Non-Destructive Evaluation (NDE) of Polymer Matrix Composites, V. M. Karbhari (Ed.). Woodhead Publishing Series in Composites Science and Engineering. Woodhead Publishing: pp. 309–336e.
- Li S. and Chu T. P. (2012): *Ultrasonic 3D reconstruction of CFRP panel delaminations*. Fall Conference & Quality Testing Show 2012. Orlando, FL: pp. 227–232.
- Li S., Poudel A. and Chu T. P. (2012): *An Image Enhancement Technique for Ultrasonic NDE of CFRP Panels*. Proc. of the 21st Annual Research Symposium & Spring Conference. Dallas, TX: pp. 21–26.
- Li S., Poudel A. and Chu T. P. (2013): *Fuzzy logic based delamination detection in CFRP panels*. Informatica 37(4): pp. 359–366.
- Liao P.-S., Chen T.-S., Chung P.-C. et al. (2001): *A fast algorithm for multilevel thresholding*. Journal of Information Science and Engineering 17(5): pp. 713–727.
- Mallick P. K. (2007): *Fiber-reinforced composites: materials, manufacturing, and design*. 3rd edn. CRC press.

- Margetan F. J., Leckey C. A. and Barnard D. (2013): *Modeling the effects of beam size and flaw morphology on ultrasonic pulse/echo sizing of delaminations in carbon composites*. AIP Conference Proceedings **1511**(1): pp. 955–962.
- Mašonkina M. and Kalniņš K. (2013): *Application of Ultrasonic Imaging Technique as Structural Health Monitoring Tool for Assessment of Defects in Glass Fiber Composite Structures*. Civil Engineering '13: 4th International Scientific Conference: Proceedings. Latvia University of Agriculture. Latvia, Jelgava: pp. 180–184.
- Masuelli M. A. (2013): Introduction of Fibre-Reinforced Polymers – Polymers and Composites: Concepts, Properties and Processes. In: Fiber Reinforced Polymers – The Technology Applied for Concrete Repair, M. A. Masuelli (Ed.). InTech.
- Meksen T. M., Boudraa M. and Boudraa B. (2013): *Neural Networks to Select Ultrasonic Data in Non Destructive Testing*. Contemporary Challenges and Solutions in Applied Artificial Intelligence. Springer International Publishing. Heidelberg: pp. 205–210.
- Meksen T. M., Draï R. and Sellidj F. (2003): *Pattern recognition in ultrasonic imagery using the Hough transform*. Proc. of the World Congress on Ultrasonics. Paris, France: pp. 753–756.
- Meola C. and Carlomagno G. M. (2013): 14 – Non-destructive evaluation (NDE) of aerospace composites: detecting impact damage. In: Non-Destructive Evaluation (NDE) of Polymer Matrix Composites, V. M. Karbhari (Ed.). Woodhead Publishing Series in Composites Science and Engineering. Woodhead Publishing: pp. 367–396.
- Meola C., Boccardi S., Carlomagno G., Boffa N., Monaco E. and Ricci F. (2015): *Nondestructive evaluation of carbon fibre reinforced composites with infrared thermography and ultrasonics*. Composite Structures **134**: pp. 845–853.
- Merazi-Meksen T., Boudraa B. and Boudraa M. (2012a): *A method to improve and automate flat defect detection during ultrasonic inspection*. International Journal of Adaptive Control and Signal Processing **26**(5): pp. 375–383.
URL: <http://dx.doi.org/10.1002/acs.1289>
- Merazi-Meksen T., Boudraa M. and Boudraa B. (2012b): *Automatic detection of circular defects during ultrasonic inspection*. Control (CONTROL), 2012 UKACC International Conference on. IEEE. Cardiff, UK: pp. 1003–1006.
- Migeon B. and Marché P. (1997): *In vitro 3D reconstruction of long bones using B-scan image processing*. Medical and Biological Engineering and Computing **35**(4): pp. 369–372.
- Minachi A., Margetan F. J. and Hsu D. K. (1993): *Delamination sizing in composite materials using a Gauss–Hermite beam model*. Ultrasonics **31**(4): pp. 237–243.

- Mix P. E. (2005): *Introduction to Nondestructive Testing: a Training Guide*. 2nd edn. John Wiley & Sons.
- Momtaz A. and Sadr A. (2009): *Clustering of Ultrasonic C-Scan Images using Rosette Pattern*. International Journal of Simulation, Systems, Science and Technology **10**(6): pp. 34–39.
- Mulcair J. and Villiers D. (2006): *Heavyweight Goes Light*. Flight Safety Australia **10**(5): pp. 49–51.
- Murphy R. V. (1987): *Ultrasonic Defect-sizing Using Decibel Drop Methods, Volume I: Text. Technical report*. Atomic Energy Control Board.
- Natke H. G. and Cempel C. (1997): *Model-aided diagnosis of mechanical systems: fundamentals, detection, localization, assessment*. Springer, Berlin, Heidelberg.
- Niblack W. (1985): *An introduction to digital image processing*. Strandberg Publishing Company.
- Niepokólczycki A., Leski A. and Dragan K. (2016): *Review of Aeronautical Fatigue Investigations in Poland (2013-2014)*. Fatigue of Aircraft Structures **1** (2016)(8): pp. 5–48.
- Noble J. A. and Boukerroui D. (2006): *Ultrasound image segmentation: a survey*. IEEE Transactions on Medical Imaging **25**(8): pp. 987–1010.
- Nock R. and Nielsen F. (2004): *Statistical region merging*. IEEE Transactions on Pattern Analysis and Machine Intelligence **26**(11): pp. 1452–1458.
- Nowosielska K. and Kowalczyk P. (2008): *Wykrywanie, lokalizacja i identyfikacja uszkodzeń w wysokowytrzymałych konstrukcjach kompozytowych*. Prace Instytutu Lotnictwa **3–4**(194–195): pp. 83–111.
- Ohlander R., Price K. and Reddy D. R. (1978): *Picture segmentation using a recursive region splitting method*. Computer graphics and image processing **8**(3): pp. 313–333.
- Olympus Corporation (2006): *Ultrasonic Transducer Technical Notes*. Panametrics-NDT.
URL: <https://mbi-ctac.sites.medinfo.ufl.edu/files/2017/02/ultrasound-basics.pdf>
- Olympus Corporation (n.a.): *Ultrasonic Flaw Detection Tutorial. 3.4 Pulser and Receiver Operation*. Accessed: 2017-01-22.
URL: <http://www.olympus-ims.com/en/ndt-tutorials/flaw-detection/>
- Osman A., Hassler U., Kaftandjian V. and Hornegger J. (2012): *An automated data processing method dedicated to 3D ultrasonic non destructive testing of composite pieces*. IOP Conference Series: Materials Science and Engineering. Vol. 42. IOP Publishing.

- Otsu N. (1979): *A threshold selection method from gray-level histograms*. IEEE Transactions on Systems, Man, and Cybernetics **9**(1): pp. 62–66.
- Pal N. R. and Pal S. K. (1989): *Entropic thresholding*. Signal Processing **16**(2): pp. 97–108.
- Papamarkos N. and Atsalakis A. (2000): *Gray-Level Reduction Using Local Spatial Features*. Computer Vision and Image Understanding **78**(3): pp. 336–350.
- Prewitt J. and Mendelsohn M. L. (1966): *The analysis of cell images*. Annals of the New York Academy of Sciences **128**(1): pp. 1035–1053.
- Pun T. (1980): *A new method for grey-level picture thresholding using the entropy of the histogram*. Signal processing **2**(3): pp. 223–237.
- Qiu T., Wen T. and Gu J. (2011): *Freehand 3D Ultrasound Reconstruction on Image-Guided Surgery*. Buletin of advanced technology research **5**: pp. 52–56.
- Rajic N. (2013): 13 – Non-destructive evaluation (NDE) of aerospace composites: flaw characterisation. In: Non-Destructive Evaluation (NDE) of Polymer Matrix Composites, V. M. Karbhari (Ed.). Woodhead Publishing Series in Composites Science and Engineering. Woodhead Publishing: pp. 335–366.
- Rashli R., Bakar E. A. and Othman A. R. (2012): *Feature analysis of ultrasonic C-Scan image for nondestructive evaluation*. Proc. of the IEEEJ Image Electronics and Visual Computing Workshop. Kuching, Malaysia: pp. 21–24.
- Reddi S. S., Rudin S. F. and Keshavan H. R. (1984): *An optimal multiple threshold scheme for image segmentation*. IEEE Transactions on Systems, Man, and Cybernetics (4): pp. 661–665.
- Reddick H. K. (1983): *Safe-life and damage-tolerant design approaches for helicopter structures*. US Army Research and Technology Laboratories. Virginia.
- Ridler T. W. and Calvard S. (1978): *Picture thresholding using an iterative selection method*. IEEE Transactions on Systems, Man, and Cybernetics **8**(8): pp. 630–632.
- Roerdink J. B. and Meijster A. (2000): *The watershed transform: Definitions, algorithms and parallelization strategies*. Fundamenta informaticae **41**(1, 2): pp. 187–228.
- Rose J. L. (1999): *Ultrasonic Waves in Solid Media*. Cambridge University Press. Cambridge.
- Safri S. N. A., Sultan M. T. H., Yidris N. and Mustapha F. (2014): *Low Velocity and High Velocity Impact Test on Composite Materials – A review*. The International Journal of Engineering and Science **3**(9): pp. 50–60.
- Sahoo P. K., Soltani S. and Wong A. K. C. (1988): *A survey of thresholding techniques*. Computer Vision, Graphics, and Image Processing **41**(2): pp. 233–260.

- Saini K., Dewal M. and Rohit M. (2010): *Ultrasound imaging and image segmentation in the area of ultrasound: a review*. International Journal of advanced science and technology **24**.
- Samanta S. and Datta D. (2012): *Imaging of impacted composite armours using data clustering*. Proc. of the 18th World Conference on Nondestructive Testing. Durban, South Africa.
- Sauvola J. and Pietikäinen M. (2000): *Adaptive document image binarization*. Pattern recognition **33**(2): pp. 225–236.
- Schijve J. (2009): *Fatigue damage in aircraft structures, not wanted, but tolerated?*. International Journal of Fatigue **31**(6): pp. 998–1011. Damage Tolerance of Aircraft Structures.
- Sezan M. I. (1990): *A peak detection algorithm and its application to histogram-based image data reduction*. Computer Vision, Graphics, and Image Processing **49**(1): pp. 36–51.
- Sezgin M. and Sankur B. (2004): *Survey over image thresholding techniques and quantitative performance evaluation*. Journal of Electronic imaging **13**(1): pp. 146–168.
- Shaw K. B. and Lohrenz M. C. (1995): *A survey of digital image segmentation algorithms. Technical report*. Naval Oceanographic and Atmospheric Research Lab. Stennis Space Center, MS.
- Shi J. and Malik J. (2000): *Normalized cuts and image segmentation*. IEEE Transactions on Pattern Analysis and Machine Intelligence **22**(8): pp. 888–905.
- Shyr T.-W. and Pan Y.-H. (2003): *Impact resistance and damage characteristics of composite laminates*. Composite Structures **62**(2): pp. 193–203.
- Skarbek W. and Koschan A. (1994): *Colour image segmentation a survey*. IEEE Transactions on Circuits and Systems for Video Technology **14**.
- Smith R. A. (2009): Composite defects and their detection. In: Encyclopaedia of Life Support Systems, R. Rawlings (Ed.). Vol. 3 of *Materials science and engineering*. UNESCO: pp. 103–143.
- Smith R. A., Marriott A. B. and Jones L. D. (1997): *Delamination sizing in fibre-reinforced plastics using pulse-echo amplitude*. Insight **39**(5): pp. 330–336.
- Sonka M., Hlavac V. and Boyle R. (2014): *Image processing, analysis, and machine vision*. 4th edn. Cengage Learning.

- Sridevi S. and Sundaresan M. (2013): *Survey of image segmentation algorithms on ultrasound medical images*. Pattern Recognition, Informatics and Mobile Engineering (PRIME), 2013 International Conference on. IEEE: pp. 215–220.
- Standard (2012): PN-EN ISO 9712:2012, Non-destructive testing – Qualification and certification of NDT personnel.
- Standard (2014a): PN-EN ISO 16810:2014, Non-destructive testing – Ultrasonic testing – General principles.
- Standard (2014b): PN-EN ISO 16811:2014, Non-destructive testing – Ultrasonic testing – Sensitivity and range setting.
- Standard (2014c): PN-EN ISO 16827:2014, Non-destructive testing – Ultrasonic testing – Characterization and sizing of discontinuities.
- Stathis P., Kavallieratou E. and Papamarkos N. (2008): *An Evaluation Technique for Binarization Algorithms*. Journal of Universal Computer Science **14**(18): pp. 3011–3030.
- Stefaniuk M. and Dragan K. (2014): *Preliminary approach for an NDT to FEM mapping software used for assessment of delamination-type damage*. Proc. of the 6th World Conference on Structural Control and Monitoring. Barcelona, Spain: pp. 2541–2551.
- Stefaniuk M. and Dragan K. (2016): *Improvements to image processing algorithms used for delamination damage extraction and modeling*. Proc. of the 19th World Conference on Non-Destructive Testing. Munich: pp. 1–8.
- Stępiński T., Uhl T. and Staszewski W. (Eds) (2013): *Advanced Structural Damage Detection: From Theory to Engineering Applications*. 1st edn. John Wiley & Sons, Ltd.
- Talreja R. and Singh C. V. (2012): *Damage and Failure of Composite Materials*. Cambridge University Press. New York.
- Taylor R. P. (2008): *Fibre composite aircraft – capability and safety. Technical Report No. AR-2007-021*. Australian Transport Safety Bureau.
- Tinga T. and Loendersloot R. (2014): *Aligning PHM, SHM and CBM by understanding the physical system failure behaviour*. European Conference of the Prognostics and Health Management Society. PHM society: pp. 1–10.
- Unnþórsson R. (2008): *Acoustic Emission Monitoring of CFRP Laminated Composites Subjected to Multi-axial Cyclic Loading*. PhD thesis. University of Iceland.
- Upadhyaya A. R., Dayananda G. N., Kamalakannan G. M., Ramaswamy Setty J. and Christopher Daniel J. (2011): *Autoclaves for Aerospace Applications: Issues and Challenges*. International Journal of Aerospace Engineering **2011**: pp. 1–11.

- Wanhill R. (2003): *Milestone Case Histories in Aircraft Structural Integrity*. Vol. 1 of *Comprehensive Structural Integrity*. Elsevier: pp. 61–72.
- Weszka J. S. (1978): *A survey of threshold selection techniques*. Computer Graphics and Image Processing **7**(2): pp. 259–265.
- Wolf C. and Jolion J.-M. (2004): *Extraction and recognition of artificial text in multimedia documents*. Pattern Analysis & Applications **6**(4): pp. 309–326.
- Wood C. A. and Bradley W. L. (1997): *Determination of the effect of seawater on the interfacial strength of an interlayer E-glass/graphite/epoxy composite by in situ observation of transverse cracking in an environmental SEM*. Composites Science and Technology **57**(8): pp. 1033–1043.
- Wood H. A. and Engle R. M. (1979): *USAF Damage Tolerant Design Handbook: Guidelines for the analysis and Design of Damage Tolerant Aircraft Structures*. Technical Report AFFDL-TR-79-3021. Air Force Flight Dynamics Laboratory at WPAFB.
- Wronkiewicz A. and Dragan K. (2016): *Damage size monitoring of composite aircraft structures based on ultrasonic testing and image processing*. Composites Theory and Practice **16**(3): pp. 154–160.
- Wronkiewicz A., Dragan K. and Lis K. (2018a): *Assessment of uncertainty in damage evaluation by ultrasonic testing of composite structures*. Composite Structures (submitted) .
- Wronkiewicz A., Dragan K., Dziendzikowski M., Chalimoniuk M. and Sbarufatti C. (2016): *3D Reconstruction of Ultrasonic B-Scans for Nondestructive Testing of Composites*. In: Proc. of the International Conference on Computer Vision and Graphics, L. J. Chmielewski, A. Datta, R. Kozera and K. Wojciechowski (Eds). Springer: pp. 266–277.
- Wronkiewicz A., Katunin A. and Dragan K. (2015): *Ultrasonic C-Scan image processing using multilevel thresholding for damage evaluation in aircraft vertical stabilizer*. International Journal of Image, Graphics and Signal Processing **7**(11): pp. 1–8.
- Wronkiewicz A., Mihaylov G., Dragan K. and Timofiejczuk A. (2018b): *Accuracy of damage detection in ultrasonic C-Scans: comparative analysis of image segmentation methods*. Ultrasonics (submitted) .
- Yeh P.-L. and Liu P.-L. (2009): *Imaging of internal cracks in concrete structures using the surface rendering technique*. NDT & E International **42**(3): pp. 181–187.
- Zack G. W., Rogers W. E. and Latt S. A. (1977): *Automatic measurement of sister chromatid exchange frequency*. Journal of Histochemistry & Cytochemistry **25**(7): pp. 741–753.

- Zaitoun N. M. and Aqel M. J. (2015): *Survey on image segmentation techniques*. Procedia Computer Science **65**: pp. 797–806.
- Zhu H., Meng F., Cai J. and Lu S. (2016): *Beyond pixels: A comprehensive survey from bottom-up to semantic image segmentation and cosegmentation*. Journal of Visual Communication and Image Representation **34**: pp. 12–27.
- Żółtowski B. (1996): *Podstawy diagnostyki maszyn*. Wydawnictwo Uczelniane Akademii Techniczno-Rolniczej. Bydgoszcz.

List of Figures

2.1	A scheme of basic prepreg products (Federal Aviation Administration, 2012a)	6
2.2	An example of quasi-isotropic material lay-up $(0/90/\pm 45)_s$ (Federal Aviation Administration, 2012a)	7
2.3	Typical autoclave moulding bagging scheme (Aero Consultants AG, n.a.)	7
2.4	Materials used in the Boeing 787 Dreamliner body (<i>Boeing 787 Specs</i> , n.a.)	9
2.5	Typical manufacturing flaws and fractures in FRP composites (Unnpórrsson, 2008)	12
2.6	Matrix crack initiated from: fibre debonds (a), void (b) (Wood and Bradley, 1997)	15
2.7	Fibre/matrix debonds (a) and coalescence into transverse cracks (b) (Gamstedt and Sjögren, 1999)	15
2.8	A scheme of fibre bridging and fibre pull-out	16
2.9	A typical impact damage mode in an FRP composite structure (adapted from (Shyr and Pan, 2003))	18
2.10	Schemes of basic modes of UT results visualisation	30
2.11	Ultrasonic inspection of a vertical stabilizer of MiG-29 carried out by the AFIT and the exemplary results (adapted from (Dragan and Synaszko, 2009))	33
2.12	Exemplary defects and damage types located in vertical stabilizers of MiG-29 (adapted from (Niepokólczycki <i>et al.</i> , 2016))	34
2.13	Exemplary tools for a C-Scan analysis available in ImagIn [®] software (the presented C-Scans concern a CFRP specimen with BVID)	36
4.1	Examples of basic wave interaction scenarios	41
4.2	Other factors affecting crack detectability	42
4.3	Influence of a flaw size and location on the echo amplitude	46
4.4	Illustrative examples of the echo display modes	48
5.1	Exemplary specimen and its nominal dimensions (depths configurations are described in the text)	65
5.2	Measurements using the coordinate measuring machine Zeiss C400 [®]	65
5.3	UT with the use of the MAUS [®] automated system	66

5.4	Exemplary pair of ultrasonic C-Scans	67
5.5	UT with the use of the FlawInspecta [®] scanner	68
5.6	Selected steps of the image analysis algorithm	69
5.7	ToF C-Scans obtained using the Pulse-Echo UT method for the specimen with FBHs at a depth of 0.5 mm	69
5.8	ToF C-Scans obtained using the Pulse-Echo UT method for the specimen with FBHs at mixed depths	70
5.9	ToF C-Scans obtained using the Pulse-Echo UT method for the specimen with FBHs at a depth of 2 mm	70
5.10	Measurement diameter error statistics for ToF C-Scans obtained using the Pulse-Echo UT method	73
5.11	Measurement depth error statistics for ToF C-Scans obtained using the Pulse-Echo UT method	75
5.12	ToF C-Scans obtained using the Phased Array UT method	76
5.13	Measurement diameter error statistics for ToF C-Scans obtained using the Phased Array UT method	76
6.1	Tested elements made of CFRP composites	79
6.2	C-Scans of the tested elements (a,c) and corresponding binary images (b,d)	80
6.3	Exemplary results of image thresholding (C-Scan of the impacted specimen)	81
6.4	Exemplary results of image thresholding (C-Scan of the aircraft panel)	81
6.5	Exemplary results of edge detection obtained for: the C-Scan of the im- pacted specimen (a,b); C-Scan of the aircraft panel (c,d)	82
6.6	Exemplary results of image segmentation (C-Scan of the impacted speci- men) with different numbers of classes (given in brackets)	83
6.7	Exemplary results of image segmentation (C-Scan of the aircraft panel) with different numbers of classes (given in brackets)	84
6.8	Segmentation accuracy obtained with the use of methods: k -means, c - means, multilevel Otsu thresholding and GMM-EM clustering	85
6.9	Exemplary results obtained using the Mean Shift clustering algorithm for: the C-Scan of the impacted specimen (a,b); C-Scan of the aircraft panel (c,d)	86
6.10	Segmentation accuracy obtained using the Mean Shift clustering algorithm	86
6.11	Exemplary results obtained using the SRM algorithm for: the C-Scan of the impacted specimen (a–d) and the aircraft panel (e–h)	87
6.12	Segmentation accuracy obtained using the SRM method	88

6.13 Exemplary results obtained using the MBP approaches (for the impacted specimen)	89
6.14 Exemplary results obtained using the MBP approaches (for the aircraft panel)	90
6.15 Exemplary results of the Gaussian-MBP algorithm (for the aircraft panel)	91
6.16 Segmentation accuracy obtained using the MBP and the Gaussian-MBP algorithms	91
7.1 Views of the CFRP specimen with BVID	94
7.2 The results of ultrasonic inspection of the specimen (C-Scans)	95
7.3 Selected slices of the tomogram (no. of slices between 80–820)	96
7.4 3D damage visualisation based on the reconstructed ToF C-Scan	97
7.5 Selected sequence of ultrasonic B-Scans (sections no. 18–45)	98
7.6 Raw 3D matrix of a series of B-Scans without (a) and with set transparency (b) and three versions of their initial processing (c–e)	99
7.7 3D damage visualisation based on the reconstructed series of B-Scans (emphasized BVID (a–d), only BVID with changed colour map (e–h))	99
7.8 3D damage visualisation based on the reconstructed CT slices	101
8.1 Impact test rig (a,b) and used impactors (c) – hemispherical (radii R given in mm): A – R17, B – R14, C – R11, D – R8, E – R5, stone impactors: K – with flat surface, N – with rough surface	104
8.2 Exemplary photographs of the specimens' surfaces after impact (limited to the central areas of 35×35 mm)	105
8.3 Ultrasonic C-Scans of the impacted specimens (reduced to dimensions of 35×35 mm)	106
8.4 Selected algorithm steps: image after segmentation (a), image after segments removal (b), ROI selection (c), input C-Scan with the BVID contour (d)	107
8.5 Calculated BVID areas for the specimens impacted with variable energy values and impactor shapes (given in the legend of colours)	107
8.6 Exemplary pair of C-Scans of a composite aircraft panel acquired during UT performed in an interval of two years	110
8.7 Selected algorithm steps: image after segmentation (a), image after segments removal (b), ROI selection (c), extracted damage region (d)	111
8.8 Contours of the selected damage region: in the first C-Scan (a), in the second C-Scan (b), superimposed C-Scans and contours (c)	111

8.9	Exemplary pairs of C-Scans and the damage extraction and comparison results	112
8.10	Parts of the C-Scan of the aircraft panel with detected delaminations . . .	114
8.11	Selected steps of the algorithm: image after segmentation (a), ROI selection (b), extracted damage region (c)	115
8.12	3D visualisation of damage sites with backgrounds of the tested aircraft panel	116

Non-destructive evaluation of composite aircraft elements based on ultrasonic testing and image analysis

Doctoral dissertation – summary

Silesian University of Technology, Faculty of Mechanical Engineering

Author: Angelika Wronkiewicz, M.Sc, Eng.

Dissertation advisor: Assoc. Prof. Anna Timofiejczuk, Ph.D., D.Sc. Eng.

Auxiliary advisor: Lt. Col. Krzysztof Dragan, Ph.D., D.Sc. Eng.

The doctoral dissertation covers the development of a methodology aimed at facilitating currently implemented procedures of diagnostics of composite aircraft elements based on ultrasonic testing. According to reports found in the literature and provided by experts performing non-destructive testing of aircrafts it is noted that there is a necessity to aid the procedures of the analysis of the ultrasonic data obtained during inspections in order to properly detect and quantify damage. This need arises from difficulties such as high time-consumption due to excessive amounts of the analysed data and large sizes of the ultrasonic scans. These inconveniences as well as data processing with manually set parameters' values lead to the occurrence of human errors and unrepeatable results.

The main goal of the research was to increase efficiency and reliability of damage detection and evaluation including its localisation, characterisation, quantification, as well as enhanced (three dimensional) visualisation. This objective was planned to be achieved with the use of developed algorithms based on image processing and analysis methods. This allowed formulating a research hypothesis that it is possible to increase efficiency and reliability of diagnostics of composite aircraft elements based on ultrasonic testing by the development of a methodology with the use of image processing and analysis methods.

In order to achieve the determined objectives and verify the set hypothesis, numerous experiments were carried out. For this purpose, artificially damaged specimens as well as aircraft components with damage induced during in-service were used. Firstly, measurement uncertainty factors influencing on the damage detection and evaluation were analysed, which allowed for the selection of the most suitable sets of ultrasonic testing parameters for further experiments. Afterwards, various image segmentation methods (including the proposed approaches) were investigated in the context of their accuracy for the damage detecting purposes. This allowed for the selection of the most suitable methods for the considered application. The next research stage concerned the analysis connected with the three dimensional reconstruction and visualisation of damage based on planar ultrasonic scans. The results were verified based on reference data acquired with the X-ray computed tomography method, which confirmed the accuracy and usefulness of such visualisation. Finally, the developed methodology was tested based on three case studies, which allowed confirming the validity of the formulated hypothesis.

Keywords: non-destructive evaluation; ultrasonic testing; diagnostics; aircrafts; image analysis.

Ocena nieniszcząca kompozytowych elementów statków powietrznych w oparciu o badania ultradźwiękowe oraz analizę obrazu

Praca doktorska – streszczenie

Politechnika Śląska, Wydział Mechaniczny Technologiczny

Autor: mgr inż. Angelika Wronkiewicz

Promotor: dr hab. inż. Anna Timofiejczuk, Prof. Pol. Śl.

Promotor pomocniczy: ppłk dr hab. inż. Krzysztof Dragan

Rozprawa doktorska dotyczy opracowanej metodyki mającej na celu ułatwienie obecnie wdrożonych procedur diagnostyki kompozytowych elementów statków powietrznych za pomocą badań ultradźwiękowych. Zgodnie z doniesieniami z literatury oraz od ekspertów przeprowadzających badania nieniszczące statków powietrznych zauważa się potrzebę wspomagania procedur analizy danych ultradźwiękowych uzyskanych podczas inspekcji w celu prawidłowego wykrywania i określania ilościowego uszkodzeń. Potrzeba ta wynika z trudności, takich jak czasochłonność analiz powodowana nadmiernymi ilościami danych oraz dużymi rozmiarami skanów ultradźwiękowych. Te niedogodności, a także przetwarzanie danych za pomocą ręcznie dobieranych wartości parametrów prowadzą do powstawania błędów ludzkich i braku powtarzalności uzyskiwanych wyników.

Głównym celem badań było zwiększenie efektywności i wiarygodności wykrywania i dokonywanej oceny uszkodzeń, w tym ich lokalizacji, identyfikacji, określania ilościowego, a także ulepszonej (trójwymiarowej) wizualizacji. Cel ten zaplanowano osiągnąć przy użyciu opracowanych algorytmów opartych na metodach przetwarzania i analizy obrazu. Pozwoliło to na sformułowanie hipotezy badawczej, iż możliwe jest zwiększenie wydajności i wiarygodności diagnostyki kompozytowych elementów statków powietrznych za pomocą badań ultradźwiękowych poprzez opracowanie metodyki z wykorzystaniem metod przetwarzania i analizy obrazu.

W celu osiągnięcia wyznaczonych celów i weryfikacji postawionej hipotezy przeprowadzono liczne eksperymenty. Na ich potrzebę wykorzystano próbki ze sztucznie wprowadzonymi uszkodzeniami oraz elementy statków powietrznych z uszkodzeniami powstałymi w trakcie ich eksploatacji. W pierwszej kolejności przeanalizowano czynniki niepewności pomiaru wpływające na wykrywanie i ocenę uszkodzeń, co pozwoliło na dobór najbardziej odpowiednich parametrów do testów ultradźwiękowych, zastosowanych w kolejnych eksperymentach. Następnie zbadano liczne metody segmentacji obrazu (w tym zaproponowane podejścia) w kontekście ich dokładności na potrzebę wykrywania uszkodzeń. Pozwoliło to na wybór najbardziej odpowiednich metod dla rozważanego zastosowania. Kolejny etap badań dotyczył analizy związanej z trójwymiarową rekonstrukcją i wizualizacją uszkodzeń na podstawie dwuwymiarowych skanów ultradźwiękowych. Wyniki zostały zweryfikowane w oparciu o dane referencyjne uzyskane metodą rentgenowskiej tomografii komputerowej, które potwierdziły poprawność i przydatność takiej wizualizacji. Opracowana metodyka została przetestowana w oparciu o trzy studia przypadków, co w wyniku pozwoliło na potwierdzenie trafności sformułowanej hipotezy.

Słowa kluczowe: ocena nieniszcząca; badania ultradźwiękowe; diagnostyka; statki powietrzne; analiza obrazu.